Study of Cosmic-ray Muons and Muons Induced Neutrons

宇宙射線渺子及其引致中子的研究

TAM, Yiu Ho

譚耀豪

A Thesis Submitted in Partial Fulfilment

of the Requirements for the Degree of

Doctor of Philosophy

in

Physics

The Chinese University of Hong Kong

September 2013

Thesis/Assessment Committee

Professor WONG, King Young (Chair)
Professor CHU, Ming Chung (Thesis Supervisor)
Professor ONG, Hock Chun Daniel (Committee Member)
Professor WONG, Tsz King Henry (External Examiner)

Abstract

In many underground particle physics experiments, cosmic-ray muons act as one of the main sources of background. It is therefore important to understand their properties. Measurements of muon flux, angular distribution, and muon induced neutrons have been carried out in the Aberdeen Tunnel Underground Laboratory. These were compared with simulations, and good agreement between the two was found. Similar study of muon induced neutrons on data from the Daya Bay Reactor Neutrino Experiment has also been carried out. We have also studied the angular distribution and time dependence of surface cosmic muon flux using scintillation hodoscopes in CUHK. The data is useful both as input for underground muon simulation and for correlation study with atmospheric conditions.

摘要

宇宙射線的渺子作為大部份地下粒子物理實驗的背景，因此我們須要了解它們的特性。我們在香港仔隧道的地下實驗室，量度了其通量分佈和它引致中子的數量。這些實驗數據和電腦模擬計算吻合。相似的渺子引致中子研究也在大亞灣核電廠中微子實驗進行。除此之外，我們也利用渺子探測器在香港中文大學量度渺子在地面的通量分佈和它的時序變化。這些數據可供給電腦來計算渺子在地下實驗室的通量分佈和了解它和大氣變化的相關性。

Acknowledgement

I sincerely thank my supervisor, Prof. CHU Ming Chung, for providing me an opportunity of joining various projects of particle physics experiment, having a lot of precious experience and making my childhood dream came true.

I would also thank Prof. K.B. Luk (UC Berkely), Dr. J.K.C Leung (HKU) and Dr. J.C.S. Pun (HKU) for their valuable discussion and suggestion.

It is impossible of conducting the experiments alone. I must thank my groupmates, Jimmy Ngai, K.K. Kwan, Y.L. Chan, Y.C. Lin, Talent Kwok, Antony Luk, Cui Kexi, X.C. Chan, Raymond Kwok, J. Xu, Steven Wong, Henoch Wong, Phoebe Lau and those scientists who contributed to the Aberdeen Tunnel Experiment and Daya Bay Neutrino Experiment.

Last but not least, I must thank Christy Lee for the unlimited support specially during my most difficult days. Also I thank my family, in memory of my beloved grandmothers, Mrs. Tam and Mrs. Lam.

Contents

Chapter 1

Introduction

1.1 Neutrino

1914, a beta decay experiment conducted by James Chadwick showed that the emitted electrons take up a continuous energy spectrum, unlike alpha or gamma decays, which give monoenergetic spectra. The continuous energy spectrum contradicts with the law of conservation of energy and momentum if only two bodies – the daughter nucleus and beta particle are involved. In 1930, Wolfgang Pauli suggested that there existed a third product in beta decays which carried away some of the energy or momentum [1]. The particle is weakly interacting and hence not easily detected. In 1956, the idea was confirmed by Clyde Cowan and Frederick Reines. They constructed an experiment near a nuclear reactor to detect electron antineutrino through the inverse beta decay (IBD) process:

$$\bar{\nu_e} + p \longrightarrow e^+ + n. \tag{1.1}$$

Two gammas were emitted when a positron annihilates with an electron. After few micro seconds, the neutrons were thermalized and captured by the Cadmium nuclei, which were then excited. The relaxation of Cadmium nuclei emitted gam-

mas. All the gammas were converted to visible light by the liquid scintillator there and then detected by photomultiplier tubes (PMT). The signature of the IBD decay was positron annihilation, known as the prompt signal, followed by neutron capture signal, known as the delayed signal. Due to the noise caused by background cosmic radiation, the experiment failed to detect neutrinos. The neutrino was discovered after the experiment was moved to underground so as to suppress the background cosmic radiation.

In 1960's, several experiments were conducted to measure the neutrino flux emitted from the nuclear fusion of Sun. Ray Davis measured the flux and found only 1/3 of the expected from the Standard Solar Model (SSM) [2]. This was the famous "solar neutrino problem". In 1969, Gribov and Pontecorvo [3] proposed theoretically the existence of neutrino oscillations. It described the change of neutrino lepton flavors (electron-type, muon-type and tau-type) as the cause of the deficit of the solar neutrino flux. In 2001, the Sudbury Neutrino Observatory (SNO) collaboration experimentally confirmed the solar neutrino oscillation. They found that not all of the neutrinos from the sun were electron-type, but some were muon-type and tau-type as well [4], even though they were all produced as electron-type in the sun This clearly showed the existence of the neutrino oscillations.

1.2 Neutrino oscillations

A neutrino has 3 mass eigenstates, ν_1, ν_2 and ν_3. The transformation of the neutrino mass eigenstates to flavor eigenstates ν_e, ν_τ and ν_μ were given by the formula [5]:

$$|\nu_i >= \sum_\alpha U^*_{\alpha i} |\nu_\alpha >, \tag{1.2}$$

where $\alpha = e$, τ, μ and $i = 1, 2, 3$ and $U^*_{\alpha i}$ is the unitary inverse transformation matrix from flavor to mass eigenstates. The mass to flavour eigenstates transform

is:

$$|\nu_\alpha >= \sum_i U_{\alpha i}|\nu_i > . \tag{1.3}$$

Eq. 1.3 can be written as:

$$\begin{pmatrix} \nu_e \\ \nu_\mu \\ \nu_\tau \end{pmatrix} = \begin{pmatrix} U_{e,1} & U_{e,2} & U_{e,3} \\ U_{\mu,1} & U_{\mu,2} & U_{\mu,3} \\ U_{\tau,1} & U_{\tau,2} & U_{\tau,3} \end{pmatrix} \begin{pmatrix} \nu_1 \\ \nu_2 \\ \nu_3 \end{pmatrix} = U_{PMNS} \begin{pmatrix} \nu_1 \\ \nu_2 \\ \nu_3 \end{pmatrix}, \tag{1.4}$$

where U_{PMNS} is called the Pontecorvo-Maki-Nakagawa-Sakata matrix [3, 6]. The matrix is parameterized by three mixing angles θ_{12}, θ_{23} and θ_{13} and a CP-violating phase δ:

$$U_{PMNS} = \begin{pmatrix} C_{12}C_{13} & S_{12}C_{13} & S_{13}e^{-i\delta} \\ -S_{12}C_{23} - C_{12}S_{23}S_{13}e^{i\delta} & -C_{12}C_{23} - S_{12}S_{23}S_{13}e^{i\delta} & S_{23}C_{13} \\ -S_{12}S_{23} - C_{12}C_{23}S_{13}e^{i\delta} & -C_{12}S_{23} - S_{12}C_{23}S_{13}e^{i\delta} & C_{23}C_{13} \end{pmatrix}, \tag{1.5}$$

where $C_{ij} = \cos\theta_{ij}$, $S_{ij} = \sin\theta_{ij}$. Table 1.1 showed the best-fitted values and 3σ confidence intervals of the mixing angles [7] before they were updated by the Daya Bay Reactor Neutrino Experiment. Both of the mixing angles θ_{12} and θ_{23} had upper and lower limits, but there was only an upper bound for θ_{13}.

Table 1.1: Best-fitted values and intervals of 3σ confidence of the mixing angles before they were updated by the Daya Bay Reactor Neutrino Experiment [7].

Parameters	Best-fit value	Interval of 3σ confidence
$\sin^2(\theta_{12})$	$0.312^{+0.017}_{-0.015}$	0.28-0.35
$\sin^2(\theta_{13})$	$0.010^{+0.009}_{-0.006}$	< 0.035
$\sin^2(\theta_{23})$	$0.51^{+0.06}_{-0.06}$	0.39-0.64

For the calculation of the disappearance probability, suppose a neutrino in a

mass eigenstate $|\nu_i>$ propagated as a plane wave, its phase change after propagation of distance L is,

$$e^{-im_i^2 \frac{L}{2E\hbar}}, \tag{1.6}$$

where m_i is the mass of the mass eigenstate and E is the total energy of the particle. For an anti-neutrino with the initial state of:

$$|\psi(0)>=|\nu_\alpha>=\sum_i U_{\alpha i}^* |\nu_i>, \tag{1.7}$$

its final state, after propagation of distance L is:

$$|\psi(L)>=|\nu_\alpha>=\sum_i U_{\alpha i}^* e^{-im_i^2 \frac{L}{2E\hbar}} |\nu_i> . \tag{1.8}$$

Therefore, Eq. 1.8 becomes:

$$|\psi(L)>=|\nu_\alpha>=\sum_i \sum_\beta U_{\alpha i}^* e^{-im_i^2 \frac{L}{2E\hbar}} U_{\beta i} |\nu_\beta> . \tag{1.9}$$

The disappearance probability is:

$$P_\alpha^{dis} = 1 - |<\nu_\alpha|\psi(L)>|^2 = 4\sum_{i>j} |U_{\alpha i} U_{\alpha j}|^2 \sin^2\left(\frac{\Delta m_{ij}^2 L}{4E\hbar}\right), \tag{1.10}$$

where $\Delta m_{ij}^2 = \Delta m_i^2$ - Δm_j^2, the mass squared difference. For $\Delta m_{13} \approx \Delta m_{23}$, the disappearance probability for ν_e is:

$$P_{\nu_e}^{dis} = C_{13}^4 \sin^2(2\theta_{12}) \sin^2\left(1.27\Delta m_{21}^2 \frac{L}{E}\right) + \sin^2(2\theta_{13}) \sin^2\left(1.27\Delta m_{31}^2 \frac{L}{E}\right), \tag{1.11}$$

where $\Delta m_{21}^2 = 0.76^{+0.20}_{-0.18}(10^{-5}\text{eV}^2)$ [8] and $\Delta m_{31}^2 = 2.32(10^{-3}\text{eV}^2)$ [8, 9].

1.3 Daya Bay Reactor Neutrino Experiment

1.3.1 Measurement of θ_{13}

In Eq. 1.11, the term $\sin^2\left(1.27\Delta m^2_{31}\frac{L}{E}\right)$ acted as the oscillation amplitude corresponding to the θ_{13} transformation. Therefore, to have a large oscillation amplitude for θ_{13}, $1.27\Delta m^2_{31}\frac{L}{E}$ have to be close to $\pi/2$. With 3-4 MeV peak energy of reactor anti-neutrinos, the baseline L, which is the detector to reactor distance, is about 2 km, which is a short baseline measurement. For $\Delta m^2_{31} >> \Delta m^2_{21}$, Eq. 1.11 can be written as:

$$P^{dis}_{\alpha} = \sin^2(2\theta_{13})\sin^2\left(1.27\Delta m^2_{31}\frac{L}{E}\right). \tag{1.12}$$

Therefore, the short baseline measurement of the oscillation is dominated by θ_{13} [10].

Fig. 1.1 showed the layout of the Daya Bay Reactor Neutrino Experiment. There are three nuclear power plants, namely Daya Bay, Ling Ao and Ling Ao II, with two reactor cores each. Each of the core generates 2.9 GW thermal power. Three experimental halls (EH), namely Daya Bay Near Hall (EH1), Ling Ao Near Hall (EH2) and Far Hall (EH3), are located underground with various overburdens to shield the cosmic muons. Table 1.2 showed the detail configuration of the EHs. Having both the near and far halls makes it possible to carry out a relative measurement, and the systematic uncertainties related to the detectors and reactors are reduced greatly. The layout of the detectors in the EH is shown in Fig 1.2. In each of the EHs, a water pool filled with ultra pure water is installed with a Cherenkov system. The water can attenuate the fast neutrons spallated from rock by cosmic muons. It also acted as a muon veto system by detecting the Cherenkov light generated by incoming muons. Besides, resistive plate chambers (RPCs) are placed on the top of the water pool. This system also acted as a muon veto system. The total efficiency of the muon veto systems is 99.5%. The detail structure of the

AD will be discussed in Chapter 4.

Table 1.2: Detail configuration of the EHs [11].

	Vertical overburden (water equivalence depth, m)	Distance from Daya Bay cores (m)	Distance from Ling Ao cores (m)	Distance from Ling Ao II cores (m)
EH1	250	360	860	1310
EH2	265	1350	480	530
EH3	860	1910	1540	1550

With data taken during the period of 24^{th} December of 2011 to 11^{th} May of 2012, about 130 days of data live time, the latest result of $\sin^2(2\theta_{13})$ announced by the Daya Bay Collaboration is [10]:

$$\sin^2(2\theta_{13}) = 0.089 \pm 0.010(\text{stat.}) \pm 0.005(\text{sys.}). \tag{1.13}$$

The results excluded no oscillation hypothesis with 7.7σ.

1.3.2 Backgrounds of the experiment

Cosmic rays and their induced products are the main backgrounds of the Daya Bay experiment. Moving the experiment underground helps to suppress the cosmic ray flux dramatically. However, the cosmic ray backgrounds still cannot be ignored for many underground experiments. Neutrons and cosmogenic isotopes such as ^{8}He and ^{9}Li, which decay and emit betas and neutrons, are induced by the cosmic muons. Some of the neutrons drifted into or were generated inside the ADs. They recoil the protons there to give a prompt-like signal. After a few micro seconds of thermalization, the neutrons are captured to give a delayed signal. They also

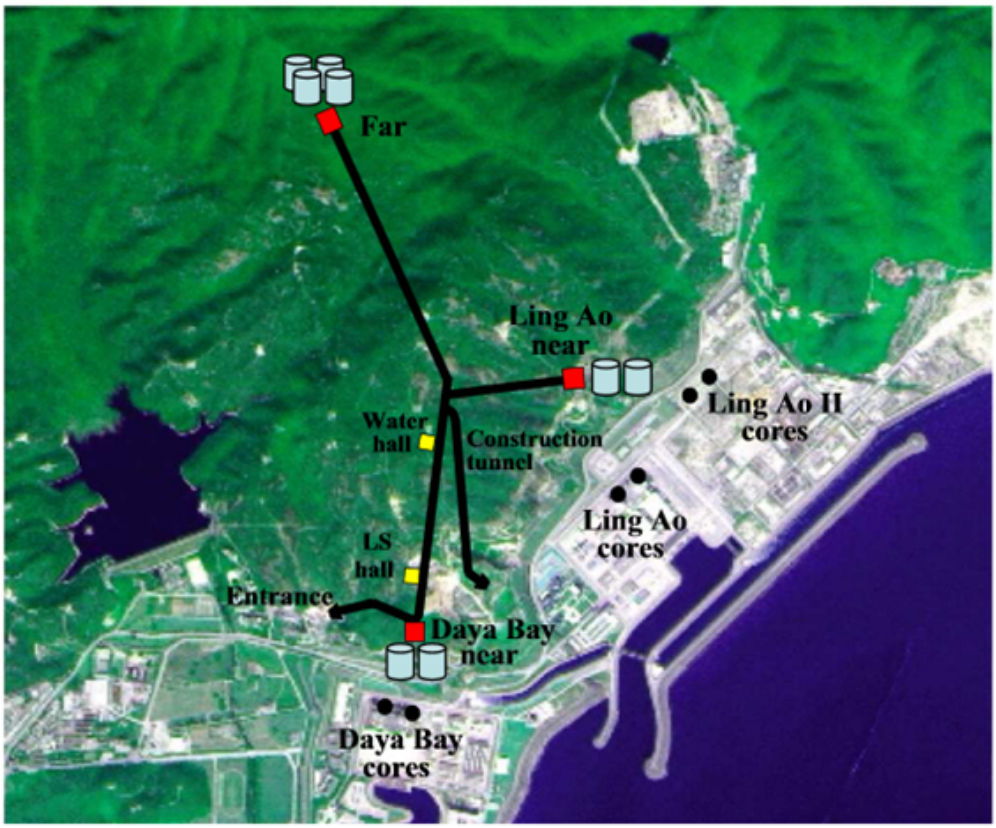

Figure 1.1: Layout of the Daya Bay Reactor Neutrino Experiment [12].

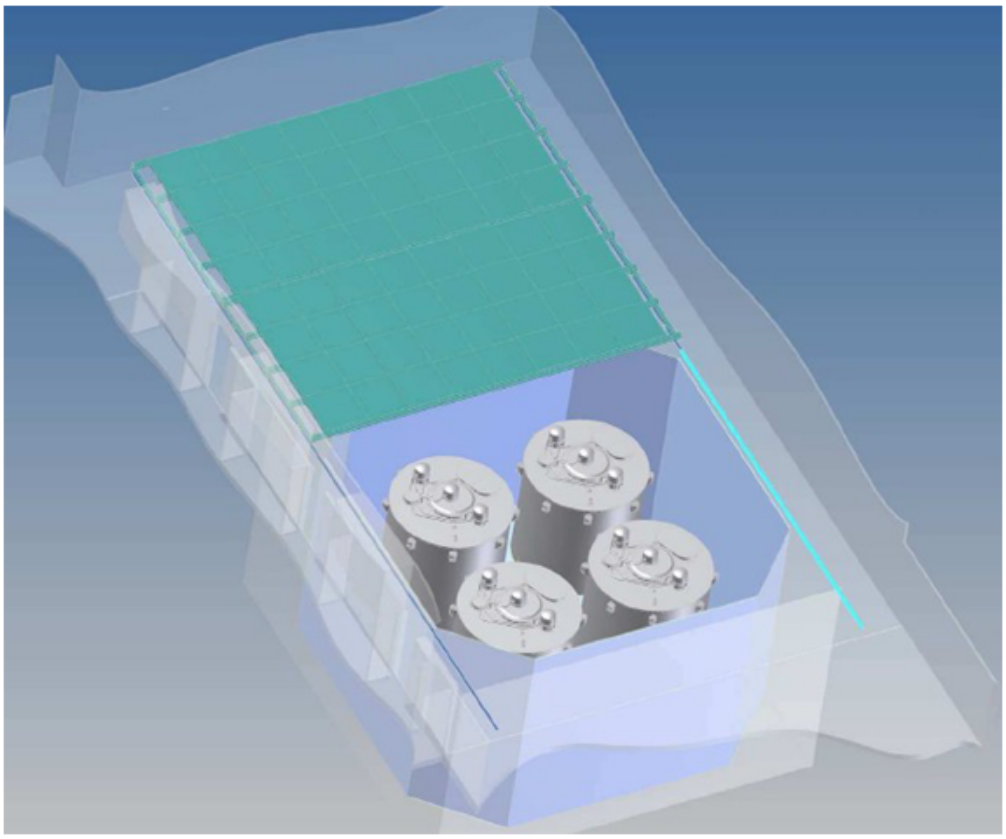

Figure 1.2: Layout of the detectors in the far hall EH3 [12]. The ADs are sitting inside the water pool. The green part is the RPC detectors placed on the top of the water pool. In this figure, the PMTs and optical decouplers for inner and outer water pool are not drawn.

contribute to accidental coincident signals. These cause unwanted backgrounds. Muon veto has to be applied for the IBD data analysis. However, the long lifetime cosmogenic isotopes (119 ms for ^{8}He and 178 ms for ^{9}Li) cannot be vetoed. Estimation of the background contributions has to be carried out carefully [13, 14]. Other non-cosmic backgrounds are gamma radiations from natural radioisotopes, neutrons emitted from natural rocks and alpha, beta radiations from Radons.

Although most of the muon induced backgrounds are vetoed by the high efficiency muon system in the Daya Bay experiment, study of cosmic muons and muon induced neutrons underground is valuable for the background estimation in many other underground particle physics experiments.

1.4 Cosmic Ray (CR) Muons

Study of cosmic rays is valuable in many aspects. First, they acted as a main source of backgrounds in underground particle physics experiments. A lot of efforts are needed for CR shielding. Second, researches recently showed that the amount of low cloud cover is correlated with the intensity of the CRs [15, 16], as shown in Fig. 1.3.The CLOUD experiment at CERN is established to study the relation between CRs and formation of clouds. If CRs and clouds are indeed related, climate condition is affected by the intensity of CRs. Third, the earth's magnetic field affects CR intensity on the ground. While the earth's magnetic fields are affected by solar activities. Fig. 1.4 showed the correlation between measured CR intensity and the observed sun spot numbers. Measurement of CR is therefore an indirect solar activity monitoring.

CRs are classified as primary or secondary. Primary CRs are mainly energetic protons coming from outside Earth's atmosphere. Fig. 1.5 showed the energy spectrum of the primary CRs. The spectrum has an energy dependence of $E^{-2.7}$ above 2 GeV. The energy extends to as large as 10^{20} eV. The mechanism for pro-

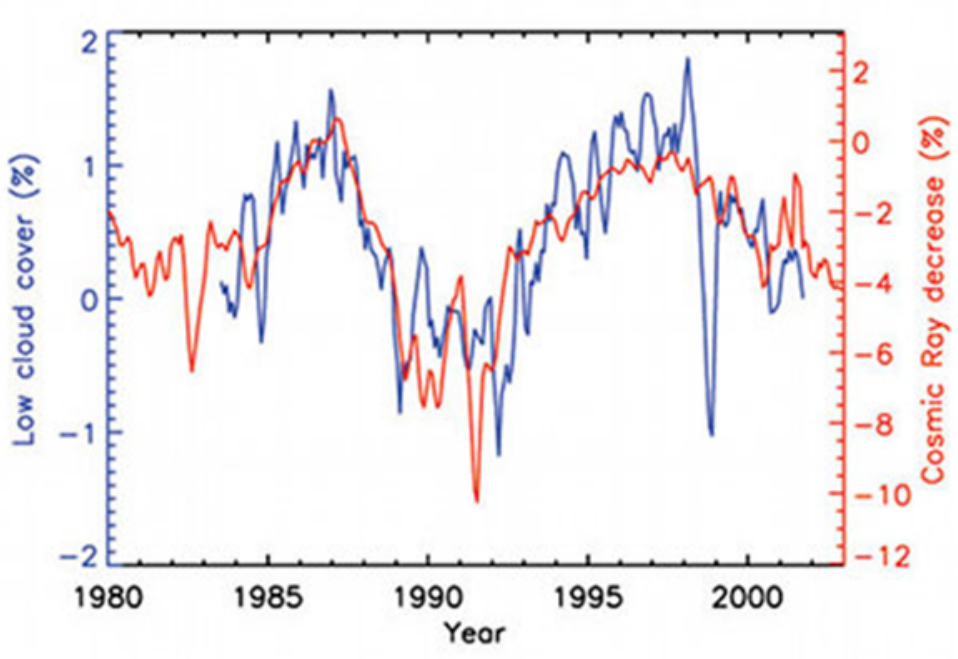

Figure 1.3: Measured CR intensity and low cloud coverage over 20 years. The figure is adapted from [16].

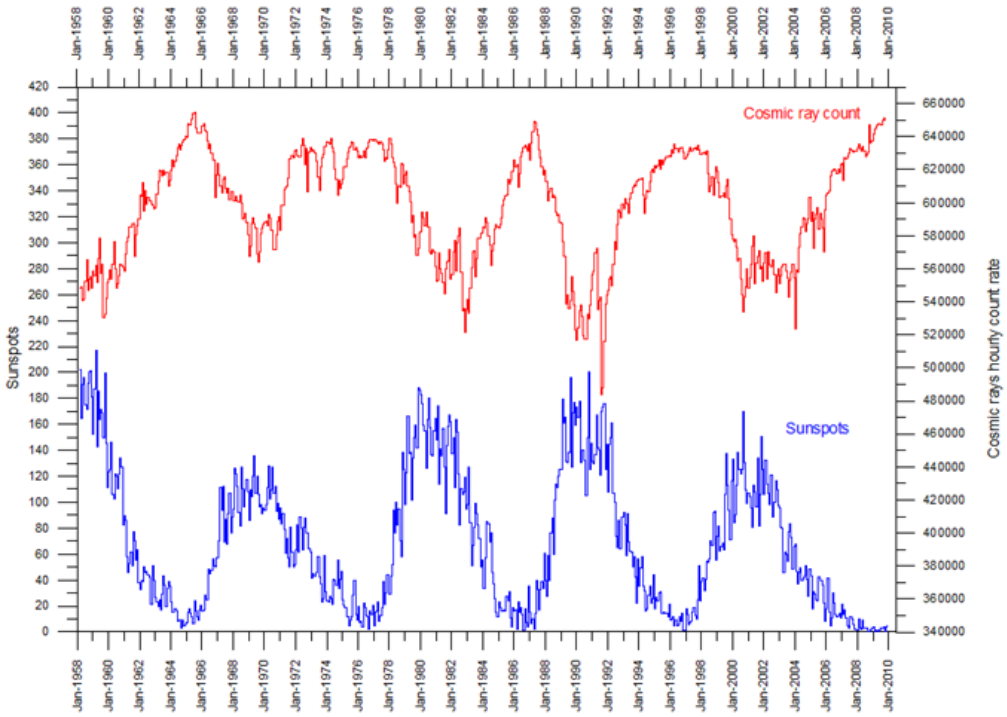

Figure 1.4: Measured CR intensity and Sun spot numbers over 50 years [17].

ducing particles with such large energy is still not confirmed. One of the accepted models of CR production is the Fermi acceleration of astrophysical shock fronts [18], such as in supernovae.

The primary CRs collide inelastically with air nuclei in the atmosphere to give secondary CRs. Pions, kaons and nucleons are produced in the collisions. Since the life-times of pions and kaons are short, they decay to give muons with life-time of 2.2 μs, which can reach the ground with the help of the relativistic time dilation effect. Muons, nucleons and other hadrons are known as the hard components of the secondary CRs. The soft components of the secondary CRs includes electrons and gammas, which are generated from decays of neutral pions or traveling charged particles. If the hard components of the secondary CRs have sufficient energy, they can initiate hadronic cascades to form more secondary particles. This is known as extensive air showers.

1.4.1 CR measured on surface

CR variation with time

There are different sources of variations of CR intensity with time, of different time scales, which are caused both extra-terrestrial and atmospheric effects.

Solar activities are one of the dominating extra-terrestrial origins of CR variations. The CR intensity is known to be anti-correlated with the 11-year solar cycle, as shown in Fig. 1.4. Besides, there are Forbush events of the CRs, which are significant decreases in the CR intensity for a few days, caused by energetic solar activities, such as coronal mass ejection (CME) [20]. These solar activities cause disturbances of the Earth's magnetic fields, which in turn suppress the primary CRs' incidences. In addition, the distribution of primary CRs is not isotopic in the solar system. The radial magnetic field of the rotating Sun has a spiral shape, known as the Parker Spiral [21]. The primary CRs are distributed along the spiral

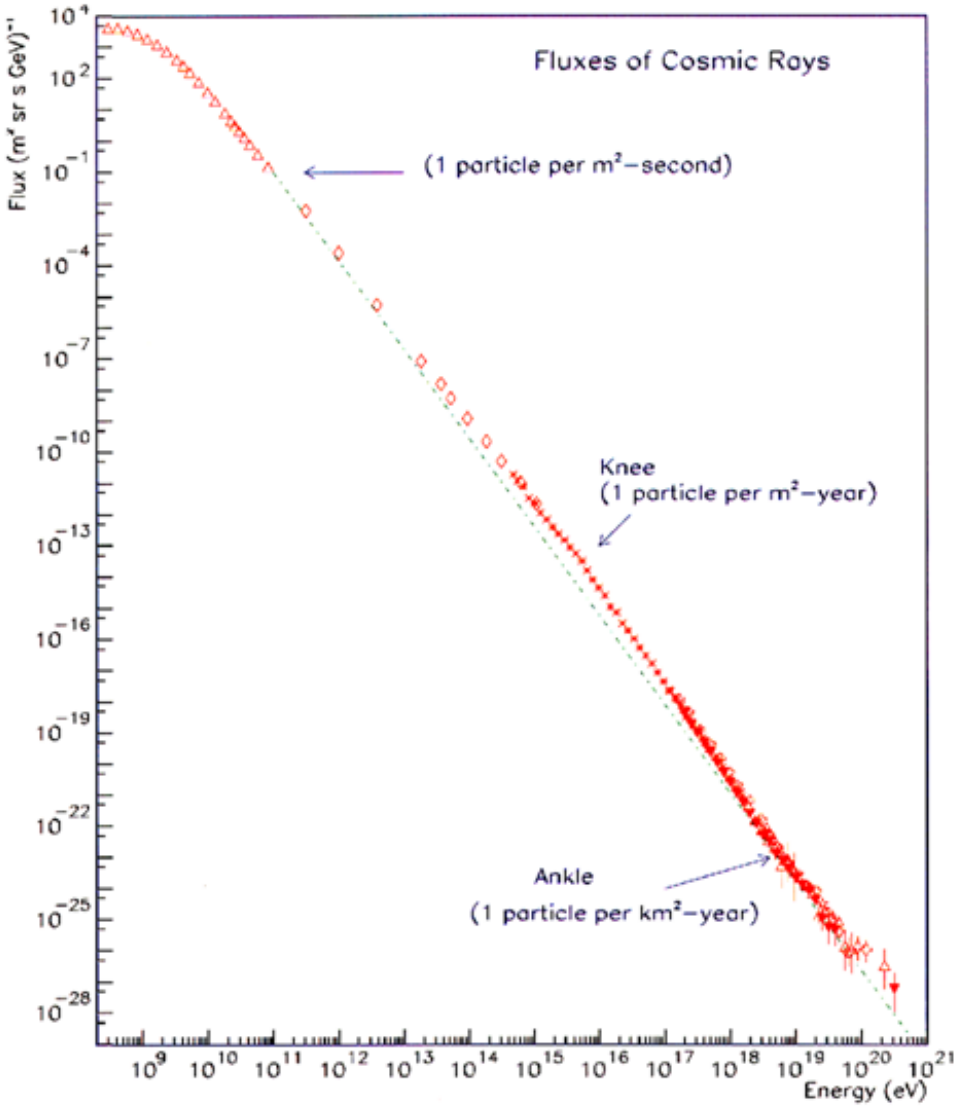

Figure 1.5: Energy spectrum of primary CR. The figure is adapted from Ref. [19].

arms. This causes a daily variation of the observed CRs on the self-rotating Earth, typically resulting in a peak observed at the local time near sun set.

The CRs are also affected by conditions of the atmosphere, known as barometric effect and temperature effect. The CRs have to travel through the atmosphere to reach the ground, during which the amount of energy loss increases with the total air mass. Some of the CRs would be stopped and decay before reaching the ground. Hence, an increase in surface air pressure would suppress the CR intensity on the ground. The barometric effect is negative [22, 23, 24] and its strength depends on the CR energy range that the detector is sensitive to. For surface muon detectors, the barometric effect is typically about -0.1% in the CR muon count change per hpa. On the other hand, there are both positive and negative temperature effects. If the temperature of the atmosphere rises, the air expands. This would shift up the production height of CR muons. As a result, some of the low energy CR muons are stopped and decay before reaching the ground. Fig. 1.6 shows an experimental result of the effect [22]. This is known as the negative temperature effect [22, 25, 24, 26]. At the same time, the expansion of the air in the production site can cause more mesons, pions and kaons, to decay without colliding with other nuclei. This would increase the CR muon production, and result in the positive temperature effect [25, 27]. High energy CR muons are not sensitive to the uplifting of the production site, and hence they only have the negative temperature effect. Hence, the temperature effect depends on the range of energy a detector is sensitive to, with typical effect of about -0.2%/°C. These effects cause different time scales of the CR variations (daily, monthly and seasonally)[24, 28].

CR variation with direction

The CR muon flux is anisotropic on the surface. There are zenith angle dependence and east-west asymmetry [29]. A schematic diagram is shown in Fig. 1.7 for the

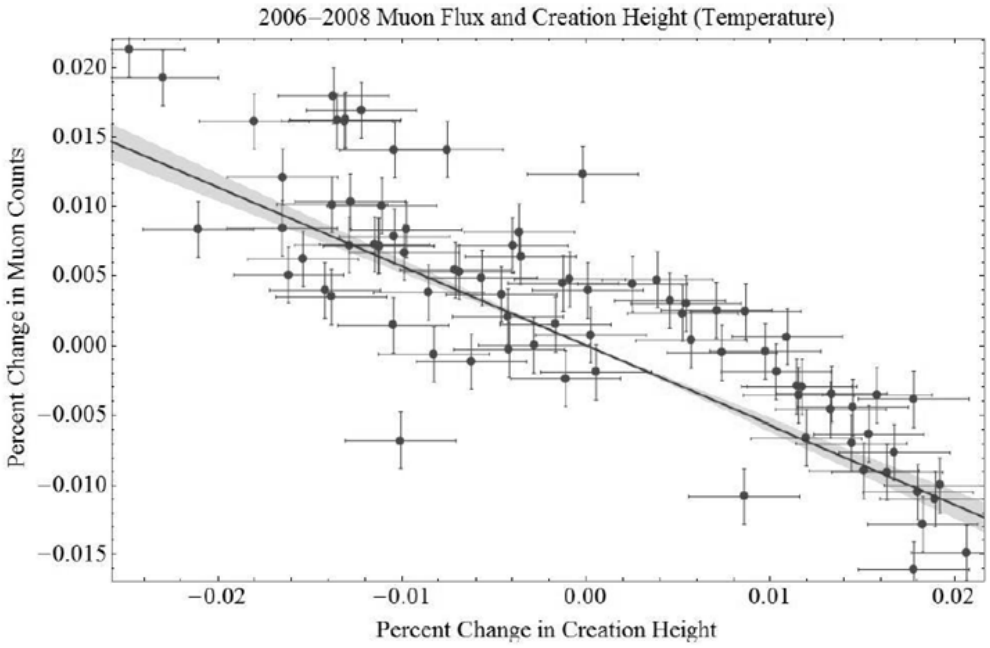

Figure 1.6: Measured negative correlation of the production (creation) height and CR muon counts in the GRAND experiment [22].

description of the zenith angle dependence. The detector is measuring muon flux coming from different paths, Path_A and Path_B. At the larger zenith angle of Path_B, CR muons have to travel a longer distance. Due to muon stopping and decay, the muon flux would be lower than that along Path_A 's, if the production intensity and height are the same. The modified Gaisser formula describes the energy E_μ and zenith angle θ dependence of the CR muon flux [30, 31]:

$$\frac{dI_\mu}{dE_\mu d\Omega} = \frac{0.14}{\text{cm}^2 \text{ s sr GeV}} \left[\frac{E_\mu}{\text{GeV}}\left(1 + \frac{3.64\text{GeV}}{E_\mu(\cos\theta^*)^{1.29}}\right)\right]^{-2.7} \left(\frac{1}{1+\frac{1.1E_\mu\cos\theta^*}{115\text{GeV}}} + \frac{0.054}{1+\frac{1.1E_\mu\cos\theta^*}{850\text{GeV}}}\right), \tag{1.14}$$

where I_μ is the muon flux, Ω is the solid angle measuring the flux, and

$$\cos\theta^* = \sqrt{\frac{(\cos\theta)^2 + P_1^2 + P_2(\cos\theta)^{P_3} + P_4(\cos\theta)^{P_5}}{1 + P_1^2 + P_2 + P_4}}, \tag{1.15}$$

where P_1 = 0.102573, P_2 = -0.068287, P_3 = 0.958633, P_4 = 0.0407253 and P_5 = 0.817285. The Earth's curvature effect at large zenith angles is considered in the formula, and the energy terms are modified from the simple $E^{-2.7}$, such that the formula works for muons with low energy or large zenith angles. The parameters are obtained by fitting with experimental results [31].

The East-West asymmetry effect is caused by Earth's magnetic field. Fig 1.8 shows a schematic diagram describing the effect. The Lorentz force acting on the positively charged protons of primary CRs suppresses those coming from East. This enhances the West counts by about 5% compared to those from East. Since high energy primary CRs are not easily deflected, they are not sensitive to the effect.

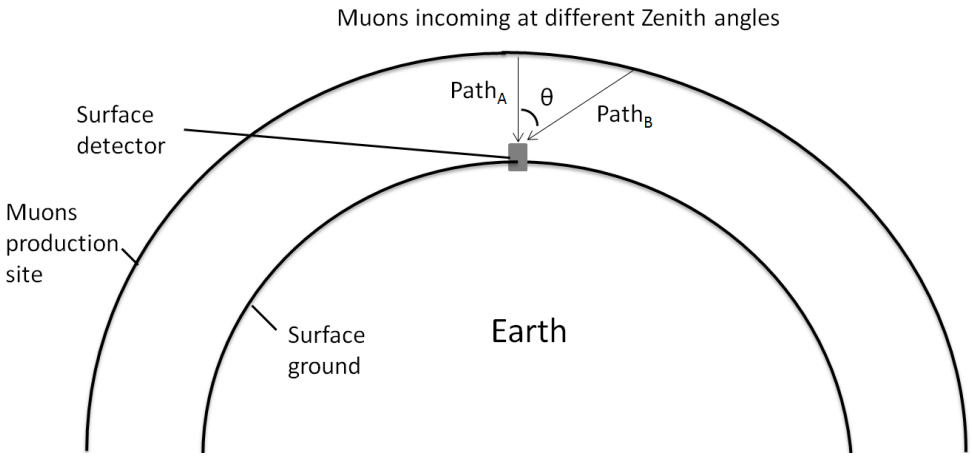

Figure 1.7: A schematic diagram for the description of the zenith angle dependence.

1.4.2 CR measured in underground

Fig. 1.9 showed the vertical muon flux against the vertical overburden in water equivalence (w.e.) depth. The flux decreases dramatically with the overburden. Only muons with high enough energy can penetrate the rocks and reach certain depth. Most of the aforementioned effects are pronounced for low energy CR muons, and so they are not noticable in underground labs. The underground CR muon flux is highly anisotropic, depending on the distribution of the overburden. Therefore, the overburden profile is important for understanding the CR flux in underground. With the profile, a program called Muon Simulation Code, MUSIC, can be used to simulate the processes of energy loss and decay of muons [32, 33]. It gives the energy and number of muons passing through the overburdens, given an input muon energy distribution.

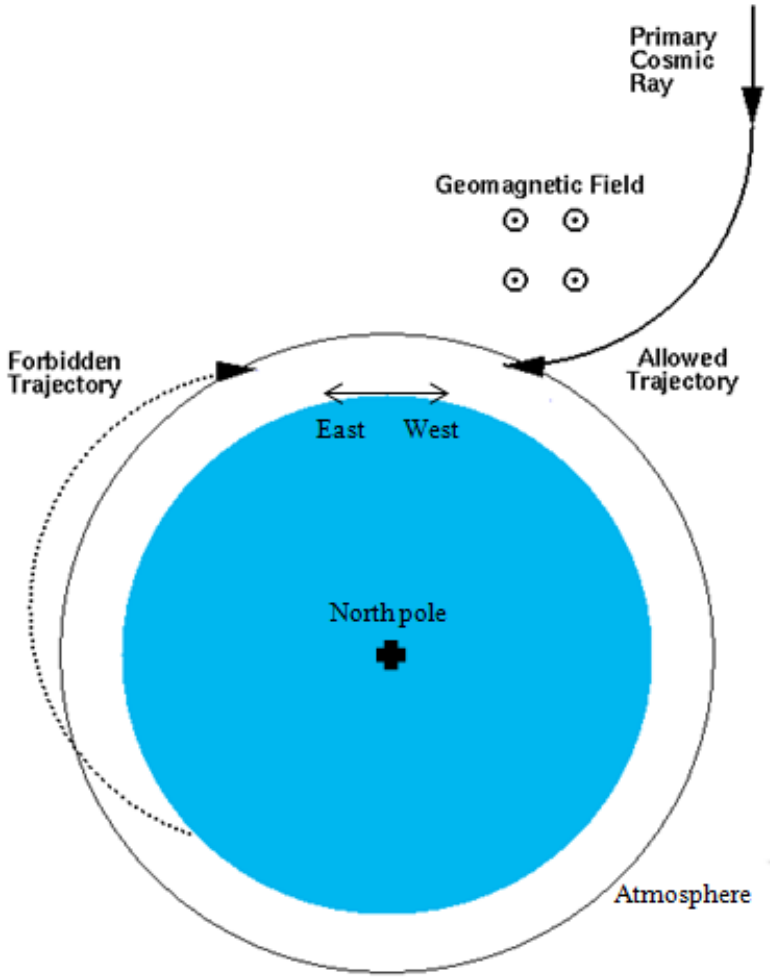

Figure 1.8: A schematic diagram describing the East-West asymmetry effect.

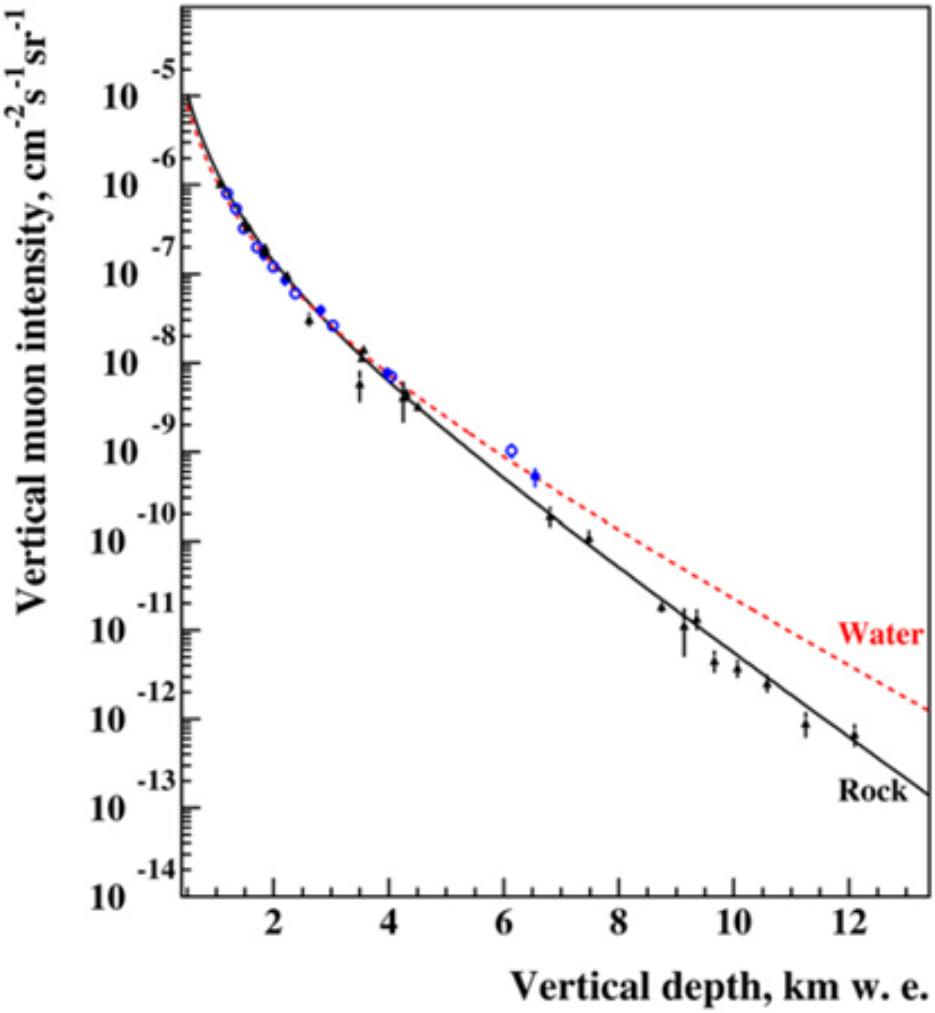

Figure 1.9: Vertical muon flux against the vertical overburden for standard rock and water from Ref. [33]. The data points for rock and water are measured by experiments [34, 35, 36].

1.5 Muon induced neutrons

Neutrons can be produced when a muon exchanges a virtual photon with a nucleus. The process is called neutron spallation. The neutrons produced can be a source of backgrounds for particle physics experiments.

Wang et al. [37] simulated the process using FLUKA-1999 to give parameterizations of the neutron yield, neutron energy spectrum and multiplicity of produced neutrons. The neutron yield, or number of neutrons N_n produced in a material density (gcm^{-3}) with total muon track length μ cm is given as:

$$N_n = 4.14 \times 10^{-6} E_\mu^{0.74} (n/(\mu g cm^{-2})), \tag{1.16}$$

where E_μ is the single muon energy in GeV. The neutron energy spectrum is:

$$\frac{dN_n}{dE} = K \left[\frac{e^{-7E_n}}{E_n} + A(E_\mu) e^{-2E_\mu} \right], \tag{1.17}$$

where K is a normalization constant, E_n is neutron energy and

$$A(E_\mu) = 0.52 - 0.58 e^{-0.0099 E_\mu}. \tag{1.18}$$

The multiplicity M of neutron generation is:

$$\frac{dN_n}{dM} = K \left[e^{-B(E_\mu)M} + C(E_\mu) e^{-D(E_\mu)M} \right], \tag{1.19}$$

where

$$B(E_\mu) = 0.085 + 0.54 e^{-0.075 E_\mu}, \tag{1.20}$$

$$C(E_\mu) = \frac{27.2}{1 + 7.2 e^{-0.076 E_\mu}}, \tag{1.21}$$

$$D(E_\mu) = 0.67 + 1.4 e^{-0.12 E_\mu}. \tag{1.22}$$

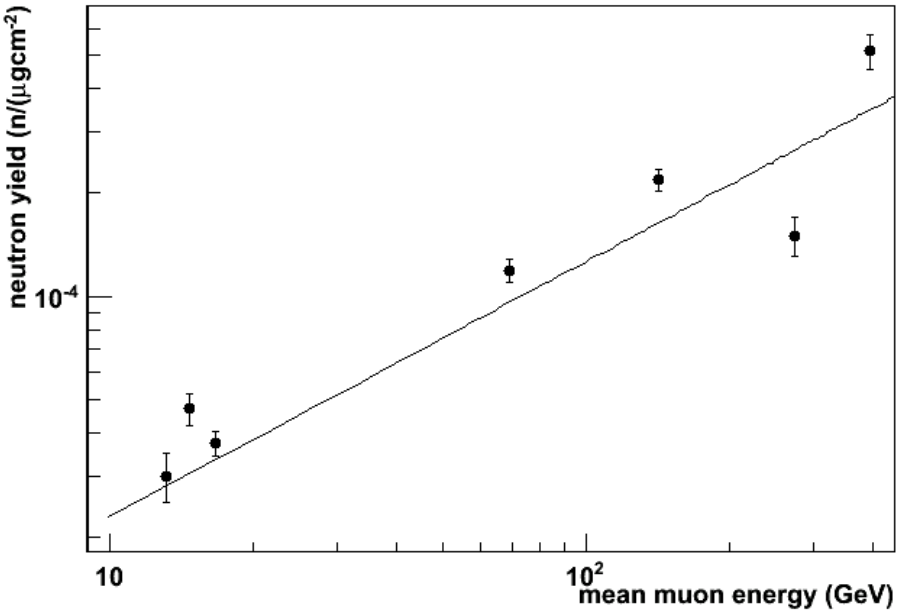

Figure 1.10: Comparison of Wang 's parameterization of spallation neutron yield with experimental results [37]. The data points are from experiments with depths (from left to right): 1) 20 m.w.e. [38], 2) 25 m.w.e. [39], 3) 32 m.w.e. [40], 4) 316 m.w.e. [38], 5) 750 m.w.e. [41], 6) 3650 m.w.e. [42], 7) 5200 m.w.e. [43].

However, Wang et al. discussed that the multiplicity was the least known property of the neutron production. Fig. 1.10 shows a comparison of the parameterization of neutron yield to other experimental results.

Chapter 2

CUHK Muon Telescope

The surface CR muon study was mainly carried out using a detector called the CUHK Muon Telescope (CMT) in Science Center North Block of CUHK, except for the measurement of Zenith angle dependence, which was carried out on the roof of the New Asia Library, CUHK, to minimize the shielding effects of the surrounding mountains and buildings. The location of Science Center North Block is at 22.42°N, 114.21°E and 110 m above sea level. Properties of surface CR muons variations, including zenith angle dependence, East-west effect and atmospheric effect, were measured and studied. The goal of the study is to have a better understanding of the origin of the CR variations.

2.1 Detector Configuration

The CMT consists of four detection layers. Each layer has 3 hodoscopes oriented in the same direction. Each hodoscope consists of a 2 cm thick 20 cm $\times$ 60 cm plastic scintillator, a photon multiplier tube (PMT) Hamamatsu H7826, and a light guide. The components are coupled together by epoxy glue and wrapped by 3M dark duct tape to shield them from external light. The hodoscope configuration

is shown in Fig. 2.1(a) (left). Totally there are 12 hodoscopes for the 4 detection layers.

The hodoscopes are arranged orthogonally between the adjacent detection layers to form 3 by 3 grids of 20 cm $\times$ 20cm each. The arrangement is shown in Fig. 2.1(a) (right). As a result, there are two layers of grids. In between the two grid layers, two 2 cm thick 60 cm $\times$ 60 cm iron plates are placed in order to block low energy background radiations, such as gamma radiations. The hodoscopes and the iron plates are mounted on an aluminum frame which sits on a motorized rotatable mount so that the telescope can be freely pointing at any direction. Besides, the separation between the grid layers can be freely adjusted to change the angular acceptance for the incident muons. The configuration of the whole set up is shown in Fig. 2.1(b).

2.2 Detection Mechanism

When a CR muon passes through a plastic scintillator, it excites the molecules there and their relaxation emits scintillation UV photons, which are absorbed by the fluorescence materials and converted into visible blue photons. The energy deposited in the 2 cm thick scintillator by a muon is of MeV order [44], and hence muons with mean energy of GeV order mostly pass through the plastic scintillator. The scintillated visible photons are total-internally reflected inside the plastic scintillator and reach the PMT through a light guide. Photoelectrons are produced by photoelectric effect in the cathode of the PMT, and the number of photoelectrons is multiplied by about 10^7 by the high voltage cathode of the PMT. An analog pulse is then produced and input to the front end electronics (FEE).

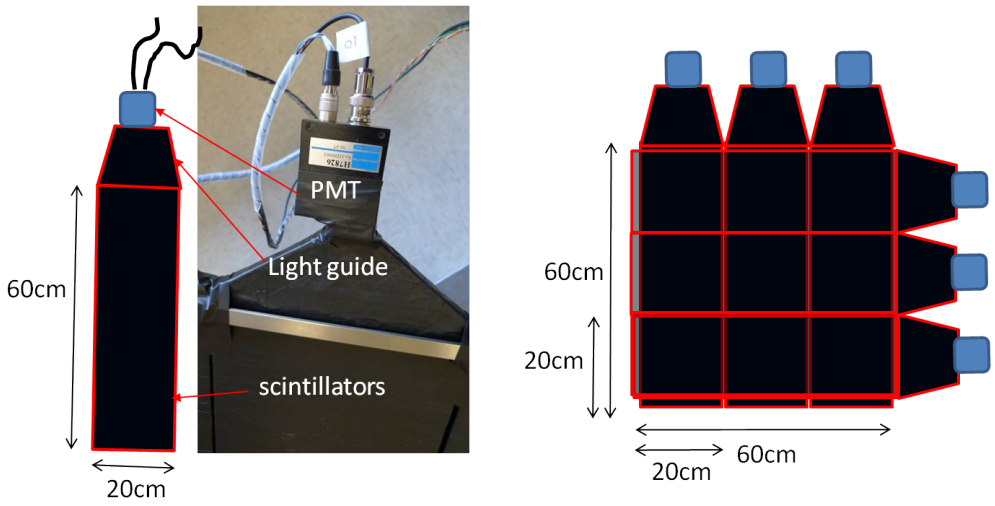

(a)

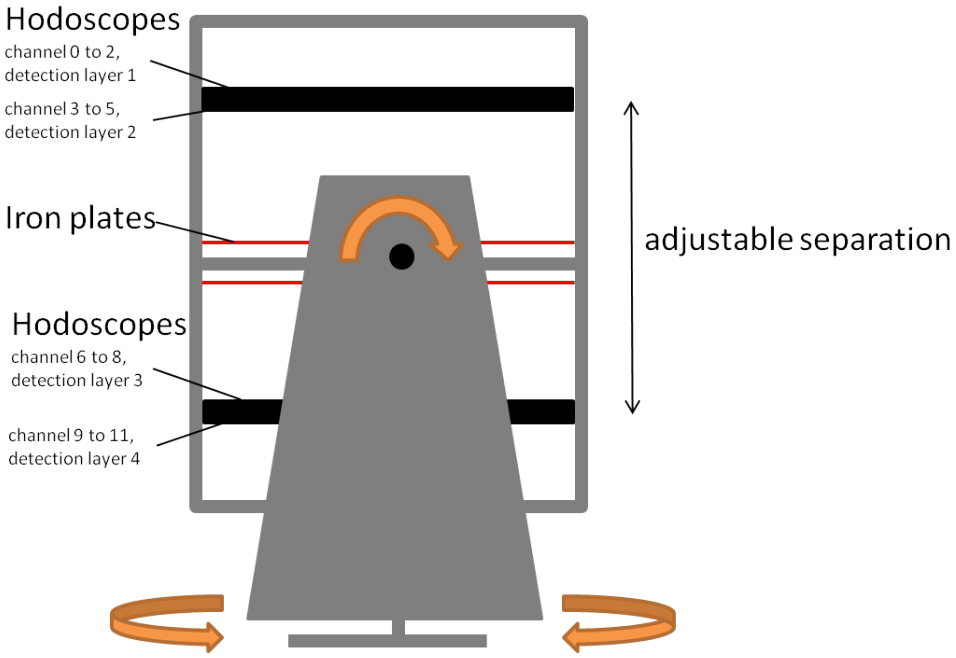

(b)

Figure 2.1: (a) Hodoscope configuration (left) and grid arrangement of hodoscopes (right) in the CUHK CMT; (b) Configuration of the whole set up with a rotatable mount.

2.3 Data Acquisition (DAQ)

The analog signal is inverted and amplified in the inverted amplifier in the FEE. Probed signals and a schematic circuit of the amplifier and the comparator are shown in Fig. 2.2 and Fig. 2.3 respectively. The amplitude of amplified signal is compared with a threshold reference value of 60 mV in a comparator (or so-called discriminator). A "True" logic signal, which is digitalized, is produced if the amplitude of the amplified signal passes the comparison. The digitized signal is then input to a programmed FPGA (Field Programmable Gate Array) electronic board, model Spartan 3E with clock rate of 100 MHz, for further processing including coincidence and event word building.

For the coincidence unit, a 100 ns time window is set when the unit receives a rising edge of true logic. After that, the unit counts an event if it detects at least one rising edge of the true logic from each of detection layer during the time window. An example of the probed event signals in coincidence is shown in Fig. 2.4. Assuming Poisson distribution for the event counts, the probability P per second of chance coincidence of 4, with 1000 Hz singles rate of the PMT, within a 100 ns time window is calculated by:

$$P = \frac{\lambda^k e^- \lambda}{k!} / 100\text{ns}, \tag{2.1}$$

where $\lambda = 1000$ Hz $\times$ 100 ns and $k = 4$, for 4-fold trigger. This gives $P = 4\times10^{-11}$ s^{-1}, which means 2.5×10^{10}s on average. Once the physics event count is generated, the event builder is triggered. A 64-bit hexadecimal event word is built. The word included a 42 bits timestamp, generated from a clock counter, and a 16-bit hit pattern of the true logic channels. Fig. 2.5 shows an example of the event word.

The event words are stored in a 256-unit sized buffer of the FPGA and then sent to a computer through a RS232 serial port. All of the event words are then

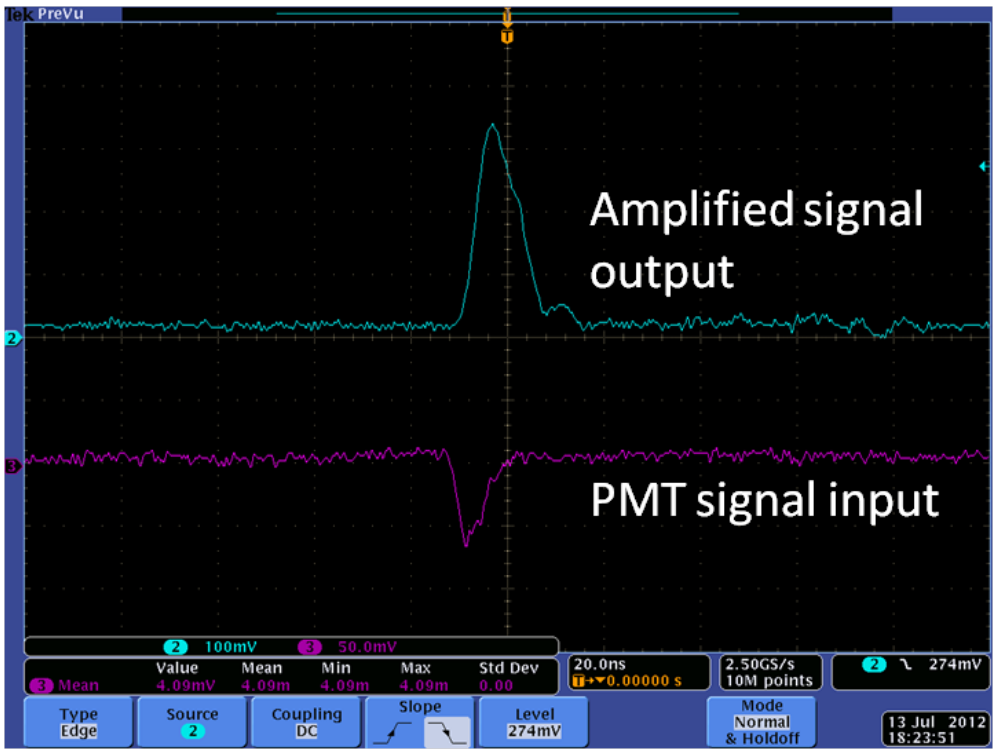

(a)

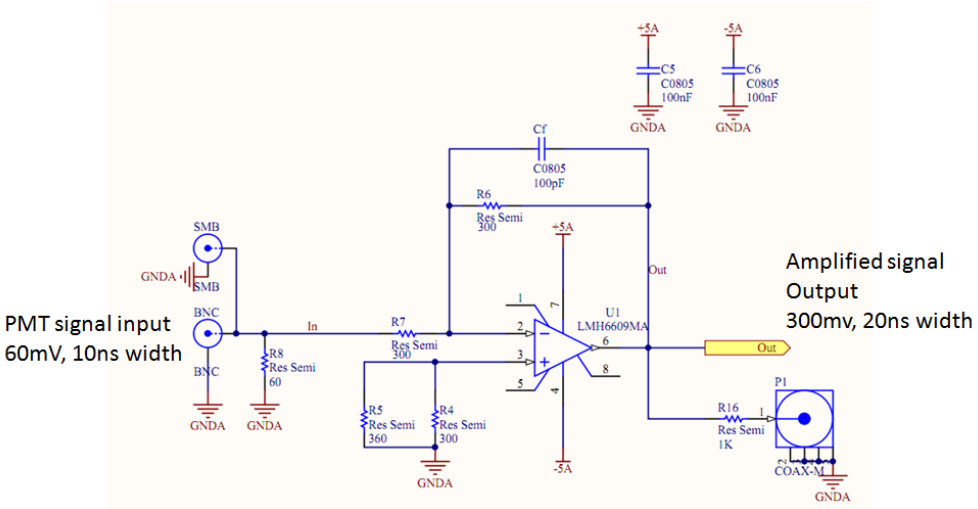

(b)

Figure 2.2: (a) Probed signals before and after the inverted amplifier. (b) Schematics of the inverted amplifier (designed by K. K. Kwan).

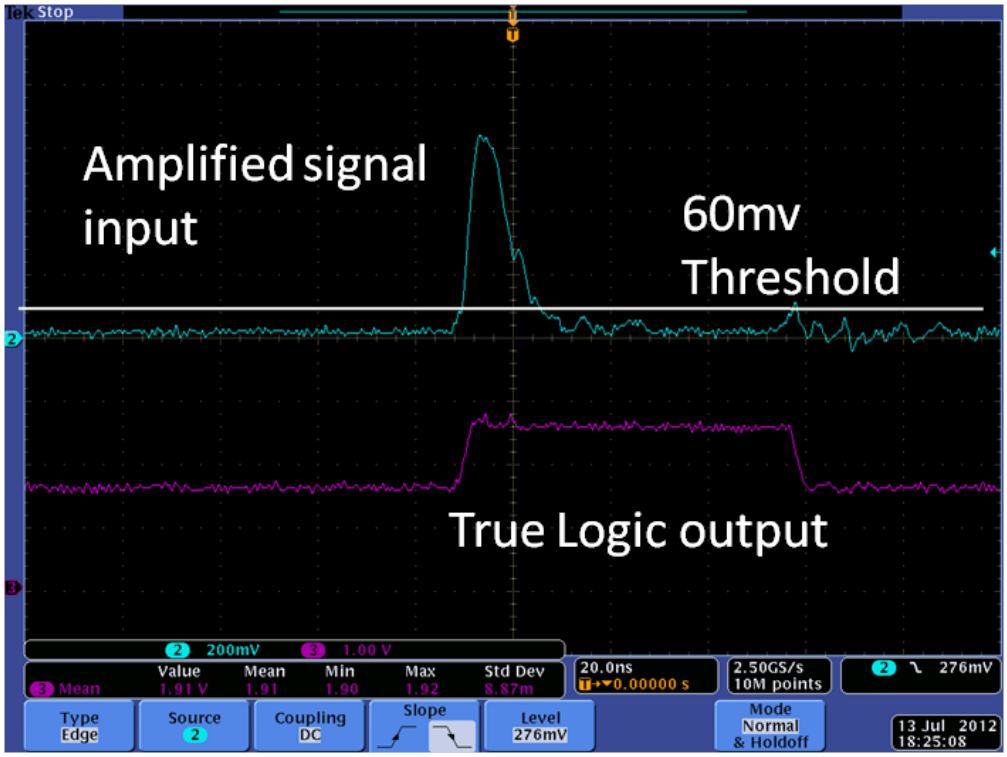

(a)

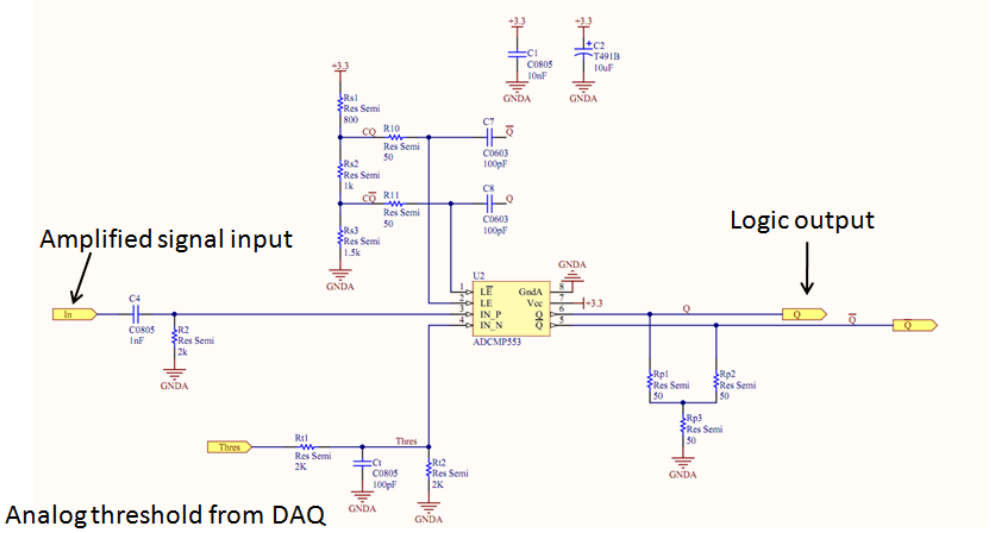

(b)

Figure 2.3: (a) Probed signals before and after the comparator (discriminator). (b) Schematics of the comparator designed by K. K. Kwan.

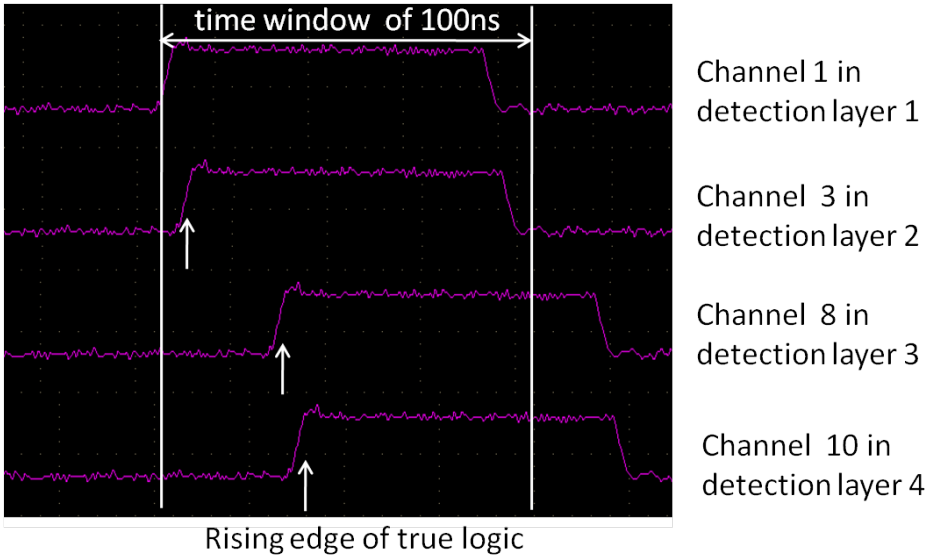

Figure 2.4: An example of the probed event signals in coincidence.

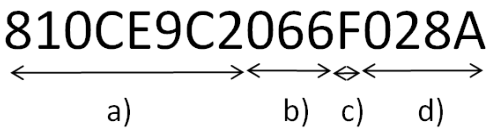

Figure 2.5: An example of the hexadecimal event word. a) The 12^{nd} to 42^{nd} bits of the timestamp with a check bit of "1" on the leftmost bit and b) The 1^{st} to $11st$ bits with a check bit of "0" on the leftmost bit; c) hit pattern of the layers with the rightmost bit for the detection layer 1.; d) hit pattern of the channels of hodoscopes with the rightmost bit for the channel 0. In this example, all four layers with Channel 1, 3, 7 and 9 got a hit signal. The timestamp is 360.92907622 s.

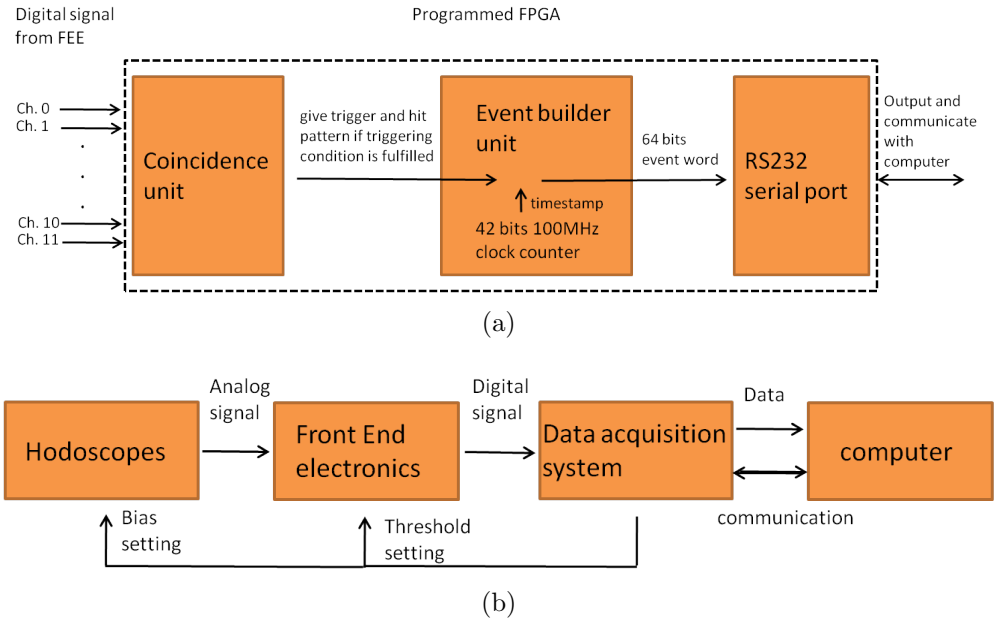

Figure 2.6: (a) Schematic of the data acquisition in FPGA. (b) Schematic of the whole Data Acquisition system.

stored in a text file with a hard drive. Besides the data storage, the computer is set to send commands, through a RS232 serial port, to a 12-bit digital-to-analog converter (DAC) unit of the FPGA for setting the threshold and bias values, used for PMT gains, of 12 channels. Fig. 2.6(a) and Fig. 2.6(b) show schematic diagrams of the data acquisition in the FPGA and the whole data acquisition system respectively.

2.4 Track reconstruction

If there are single hits of a hodoscope in each detection layer, the track incidence angle can be traced from the hit pattern. The 2 grid layers, with a structure of 3×3 pixels in each of the layer, form 81 combinations (combos) of pixel hits for a single track. The corresponding effective area of each combo as a function θ

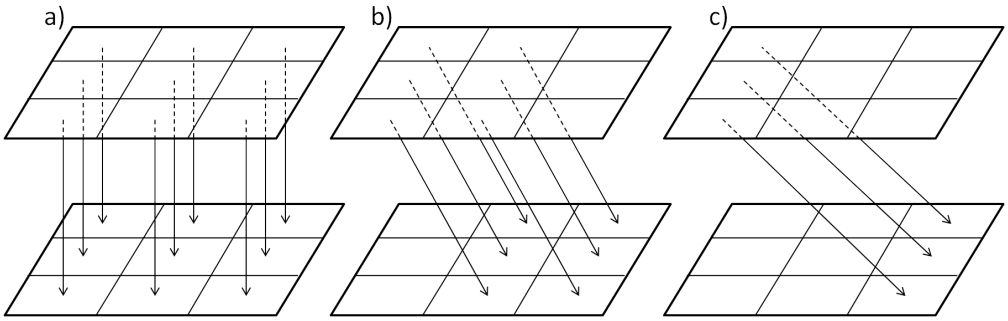

Figure 2.7: Frequently used combos. a) 9 combos for vertical tracks, b) 6 1-offset combos for tilted tracks and c) 3 two-offset combos for larger tilted tracks. Here, for 1- or 2-offset combos, only tracks tilting to right handed side are shown.

and ϕ is given by the overlapped area for pixel to pixel projection. Frequently used combos are vertically overlapped pixels and one-offset or two-offset pixels as shown in Fig. 2.7. Fig. 2.8 and Fig. 2.9 shows the effective area for some common combos at layer separations of 150 cm and 40 cm.

2.5 Muon flux measurement and results

There are time averaged and dependent effects on the CR count variations. Different types of measurement methods had been used. Results were analyzed and compared with some theoretical models.

2.5.1 Time averaged CR variations

The zenith angle dependence and East-West count asymmetry effects were studied. These effects are constant in time within the measurement period.

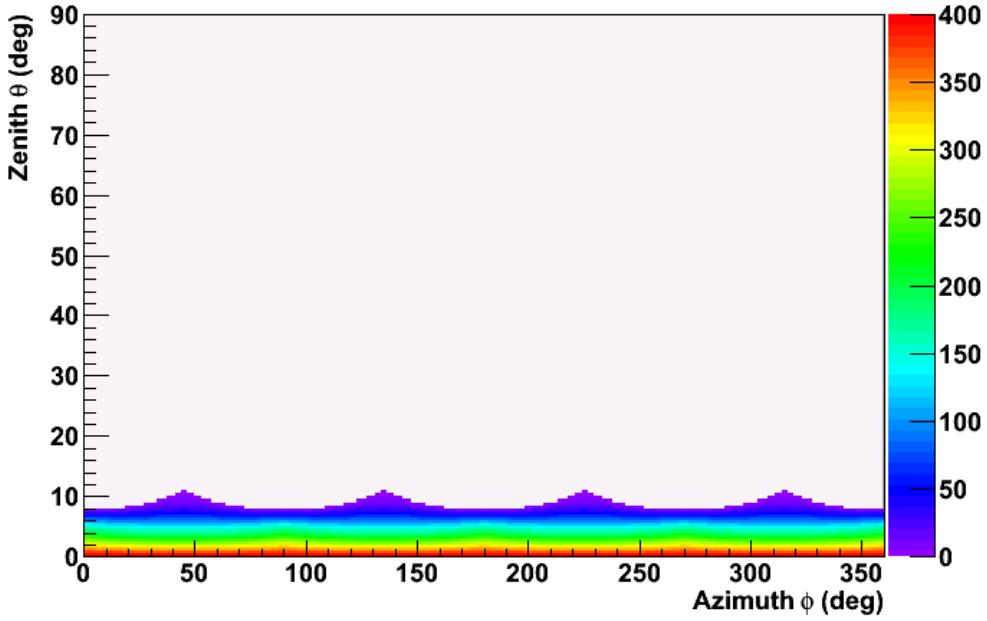

(a)

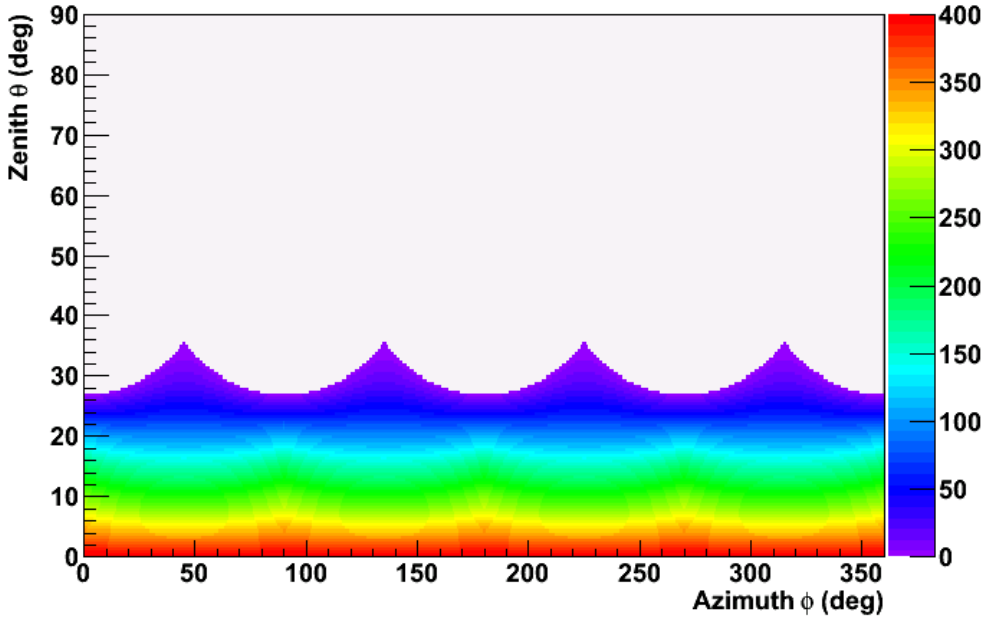

(b)

Figure 2.8: Effective areas as a function θ and ϕ for some of common combos: (a) vertical combos at separation = 150 cm; (b) vertical combos at separation = 40 cm. The color codes represent the effective areas in unit of cm^2.

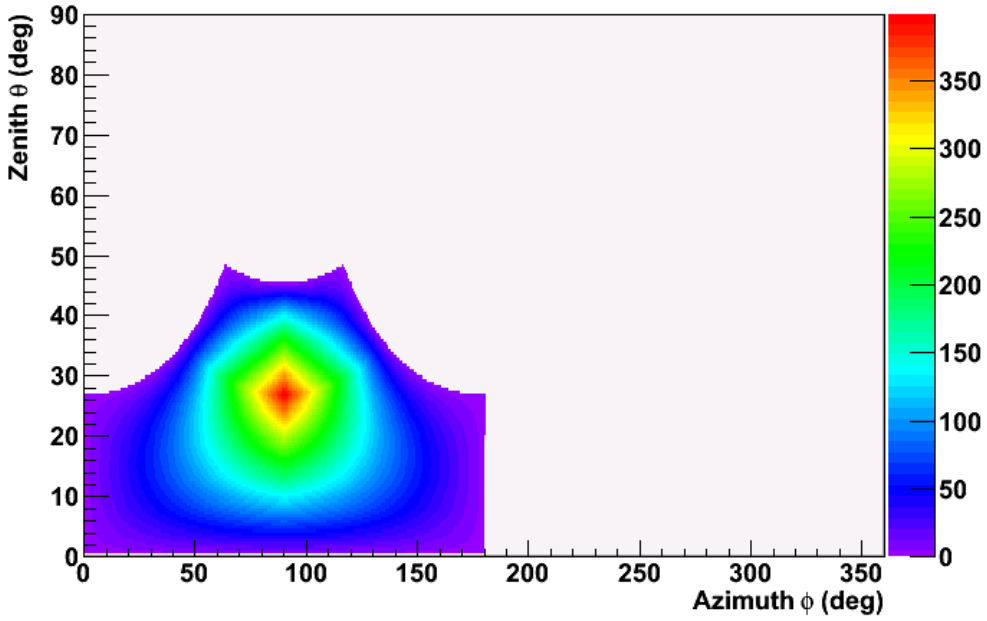

(a)

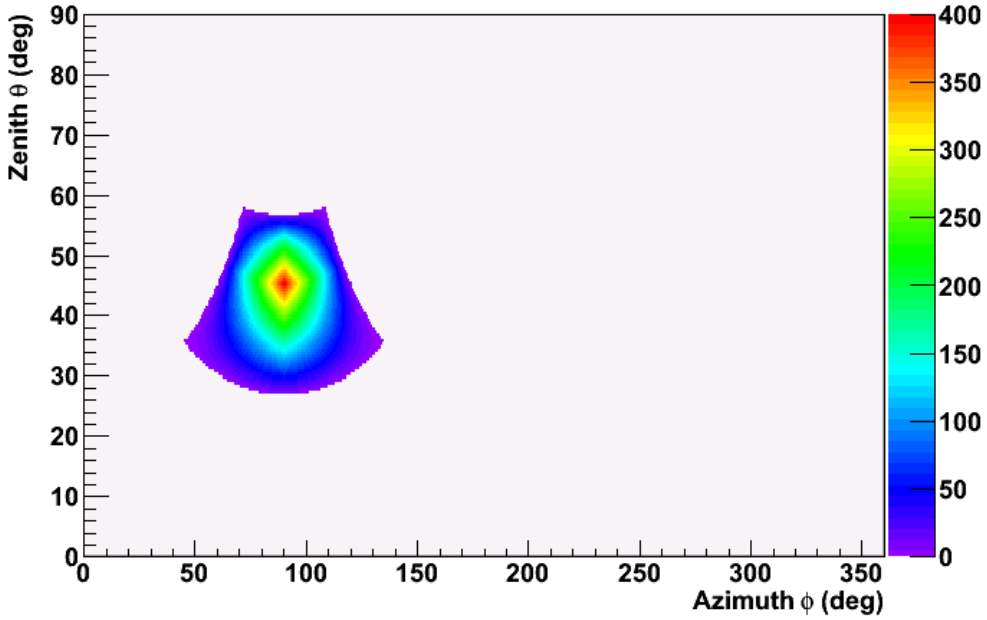

(b)

Figure 2.9: Effective areas as a function θ and ϕ for some of common combos: (a) 1-offset-combos at separation = 40 cm; (b) 2-offset combos at separation = 40 cm. North is at $\phi = 0°$. The color codes represent the effective areas in unit of cm^2.

Zenith angle dependence

The measurement was carried out in the New Asia Astronomy Observatory Dome of the CUHK. Its location is on the roof of the New Asia Library (about 150 m above sea level), CUHK, and there is no concrete or hill blockage of CRs for a large range of zenith angles. The vertical axis of the telescope was tilted to point at different zenith angles for count rate measurement.

The separation between the grid layers was set to maximum (1.5 m) to minimize the angular acceptance, or to maximize the angle resolution. The counts of the 9 vertical combos were considered. In this configuration, the angular acceptance of zenith angle, θ, for each of the vertical combo is about plus or minus 10° centered at the angle of the vertical axis of the telescope. In order to have good enough statistics, the data taking duration is much longer at the large zenith angles where the count rates are low. Table 2.1 shows the duration of data taking at different angles. The telescope was set to point at 0° to 70° of zenith angle with 10° intervals. The result was plotted on Fig. 2.10. 5% estimated uncertainty is added for the daily and atmospheric effects in counts, which are discussed in a later section.

The zenith angle dependence of cosmic ray rates was compared with a modified Gaisser formula [31]. For a rough comparison of the absolute flux, at zenith angle of 0°, the expected count rate for the detector with about 30% averaged 4-fold triggering efficiency, 60 cm^2 detection area and 10° in θ angular acceptance over 360° in ϕ is about 3200 counts per hour, which agrees quite well with the measurement result of 2900 counts per hour. However, instead of the absolute flux, the ratio of count rates at different zenith angles is considered. Many systematic errors are cancelled out by considering the relative measurement.

The integrated modified Gaisser formula with 10° angular acceptance was normalized by a fitting parameter and compared with normalized measurement result. The Chi-squared fitting method was applied and the result is shown in Fig. 2.11.

Table 2.1: The duration of data taking at different angles.

Zenith angle θ (degrees)	Data taking duration (hours)
0	23
10	30
20	22
30	19
40	41
50	42
60	54
70	72

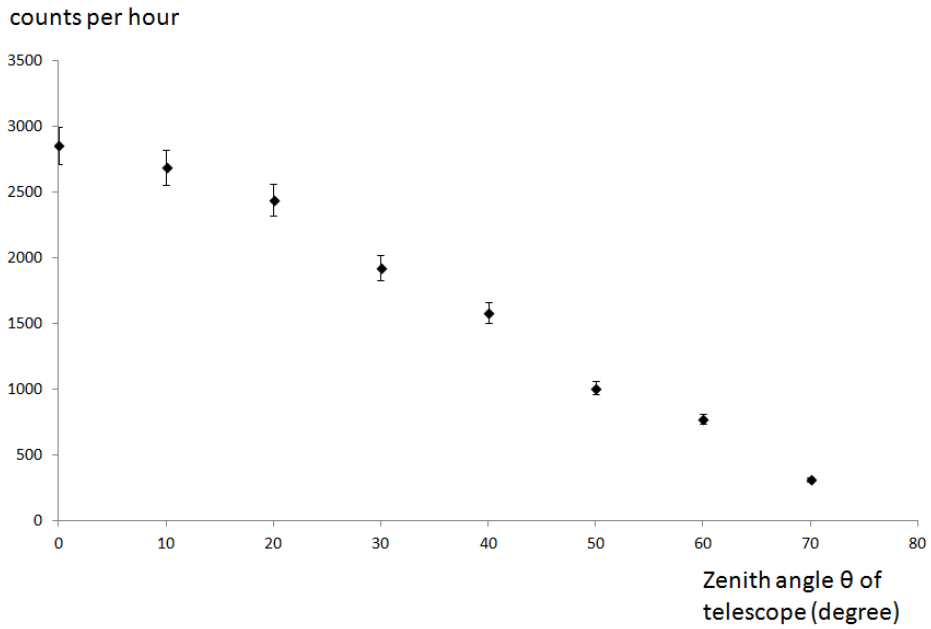

Figure 2.10: Measured zenith angle dependence of surface cosmic ray rates.

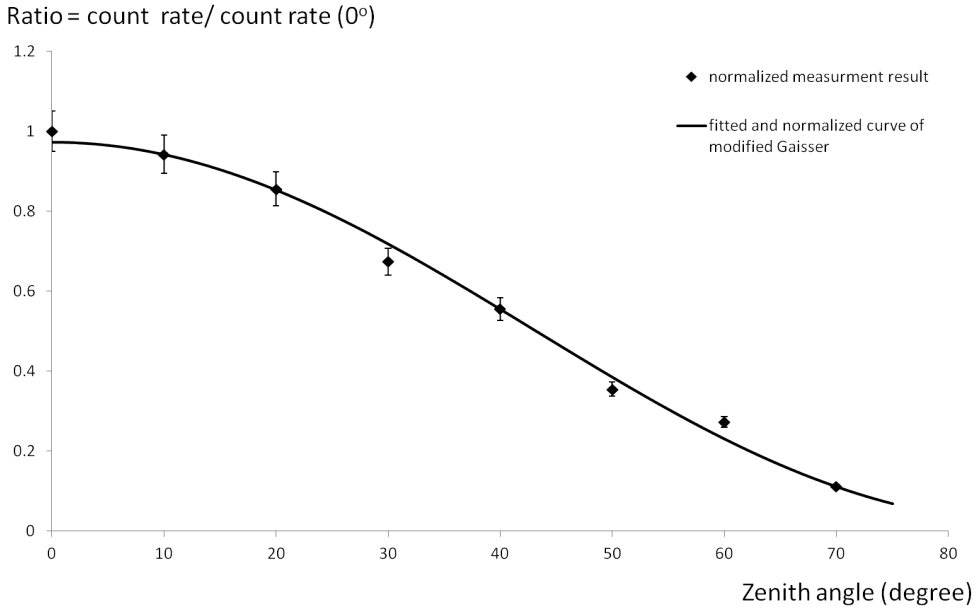

Figure 2.11: Fitted normalized modified Gaisser distribution compared with the normalized measurement data of zenith angle dependence of cosmic ray rates.

The fitted chi-squared per degree of freedom is 14.5/7. Beside the 10° of angular acceptance, the formula is also integrated with other values of angular acceptance. Fig. 2.12 shows a plot of the fitted chi-squared values against the range of integration of angular acceptance. In the plot, the minimum chi-squared value is for angular acceptance of around 10°-15°, which is quite consistent with the calculated angular acceptance.

East-West effect

The measurement of the East-West count asymmetry was carried out in a room on the roof of the Science Center North Block, to reduce the asymmetry of concrete blockage of CR. The separation of the grid layers is 40 cm. The CR tracks coming from East, West, South and North were traced by the combo selection method, as mentioned on Fig. 2.7, while the telescope's vertical axis remained pointing verti-

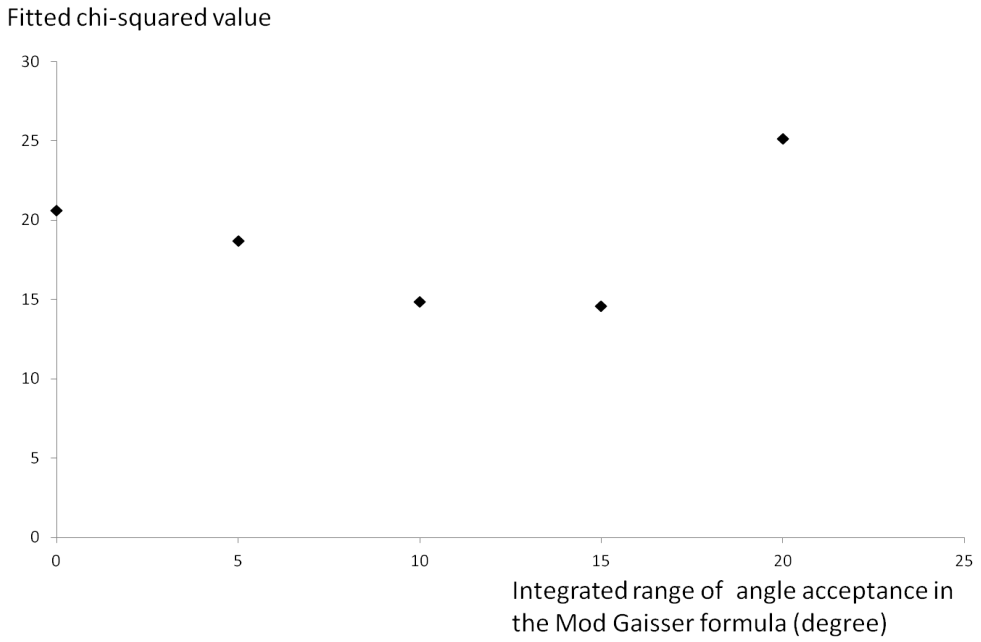

Figure 2.12: A plot of the fitted chi-squared value against the range of integration of angular acceptance. The number of degrees of freedom here is 7.

cally upward. The six 1-offset combos and the three 2-offset combos were selected for the measurement. Since the uncertainties of the combo efficiency correction method, which is obtained by propagating the uncertainties of the hodoscope efficiencies, are larger than the interested effect, the measurement of EWSN count asymmetry had been done by the 'measurement-rotation' method. First, we align the telescope in a position such that the combos trace the tracks coming exactly from the EWSN direction. Second, we take a count measurement for about a day. After that, the telescope is rotated by 90° about the vertical axis. The above procedure is repeated for 3 more times to finish a complete measurement. We then sum the total counts contributed from different combos for a certain direction of the tracks. The results are independent of the combo efficiencies. To cancel out the daily and atmospheric effects of CR count variations, the counts of the various combos were normalized by the counts of the 9 vertical combos during the same period of measurement. Each period of measurement was 94 hours. The results were shown in Fig. 2.13. The statistical uncertainty is about 0.2%. In the plot, an obvious asymmetry of the counts can be seen. Fig. 2.14 shows the ratios of the counts for East to West and South to North. The East-West count asymmetries for the 1-offset and 2-offset combos are about 8% and 14% respectively. The East-West asymmetry is much larger than that of South-North.

The result was compared with a simulation done using GEANT4 for the distribution of incoming muons according to the geomagnetic fields of Hong Kong [45]. The simulated result showing the East-West asymmetry is shown in Fig. 2.15. In the figure, more muons are coming from the West. The simulated result is folded with the effective area of the combos, as shown in Fig. 2.16, for a quantitative comparison. An uncertainty of 1.5% due to up to 30 cm difference in concrete thickness in different sides of the room is estimated. This is based on the threshold of 250 MeV muon energy required to pass through the concrete,

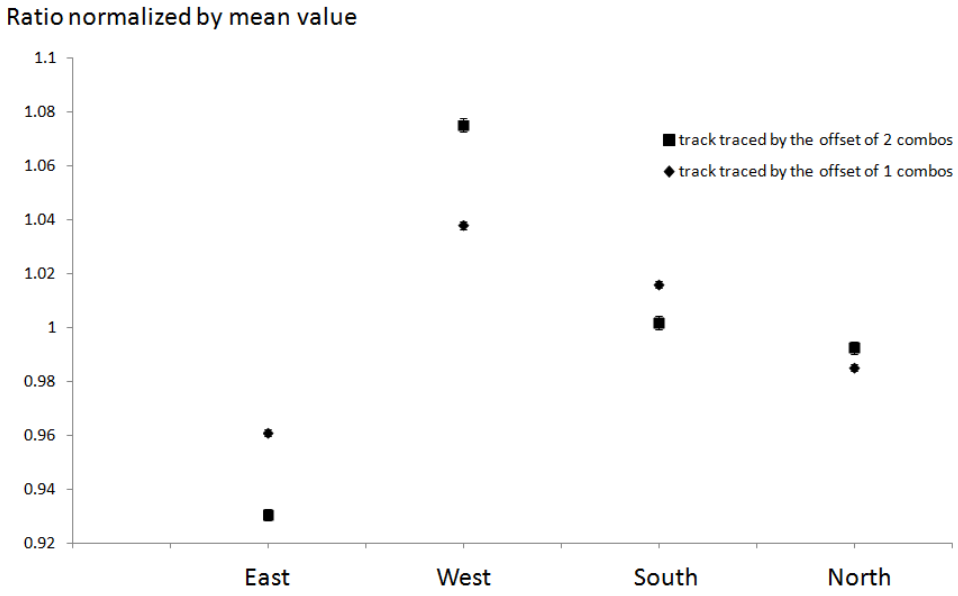

Figure 2.13: Averaged ratios of counts to the vertical counts normalized by the mean value of the ratios for the four different directions.

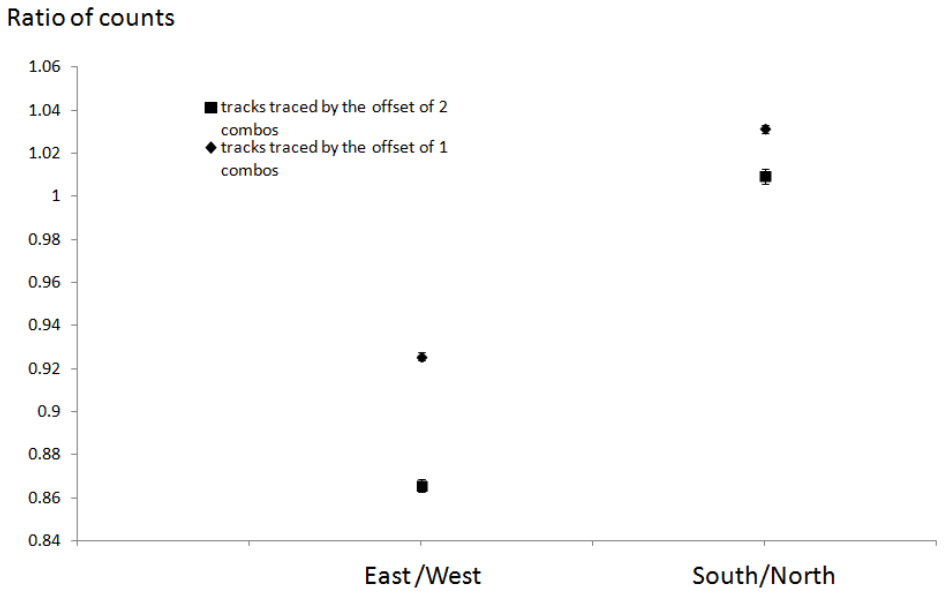

Figure 2.14: Ratios of counts for East to West and South to North.

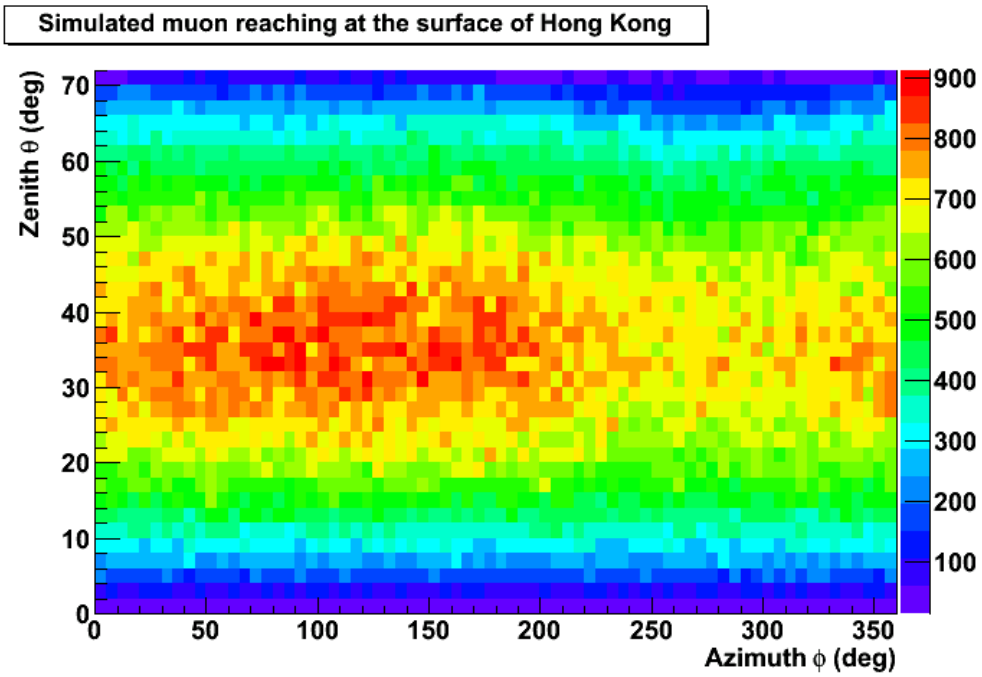

Figure 2.15: Angular distribution of muons reaching the surface of Hong Kong, simulated using GEANT4 by Chan [45]. $\phi = 0°$ corresponds to North. The color codes represent the number of incoming muons.

obtained in the simulation. Fig. 2.17 compares the ratios of counts for East-West and South-North in measurement and simulation. The plots show a good agreement between simulation and experiment, except for the 2-offset combos for the Southern direction which shows a two sigma of deviation.

2.5.2 Time dependent CR variations

For the measurement of CR count rate time series, the telescope was set to point at vertically upward direction ($\theta = 0$). The grid layer separation was 40 cm and all 81 triggering combos were measured, in order to have a good statistics of counts. The data taking was during the period of 20^{th} Jan to 4^{th} June of 2012. The hourly counts during the period are shown in Fig. 2.18 The discontinuity of the series

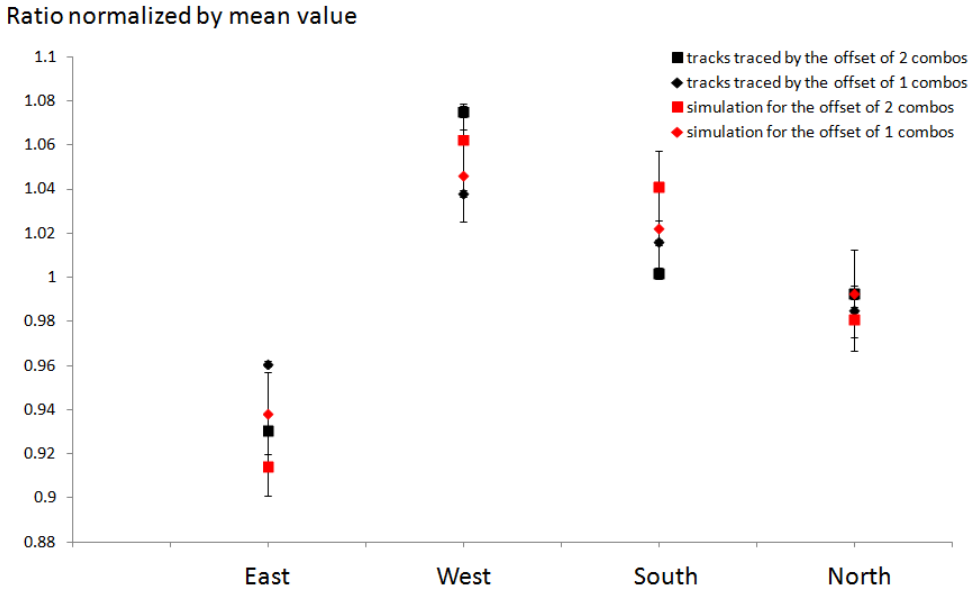

Figure 2.16: Normalized ratios of counts of the four directions compared with the simulation.

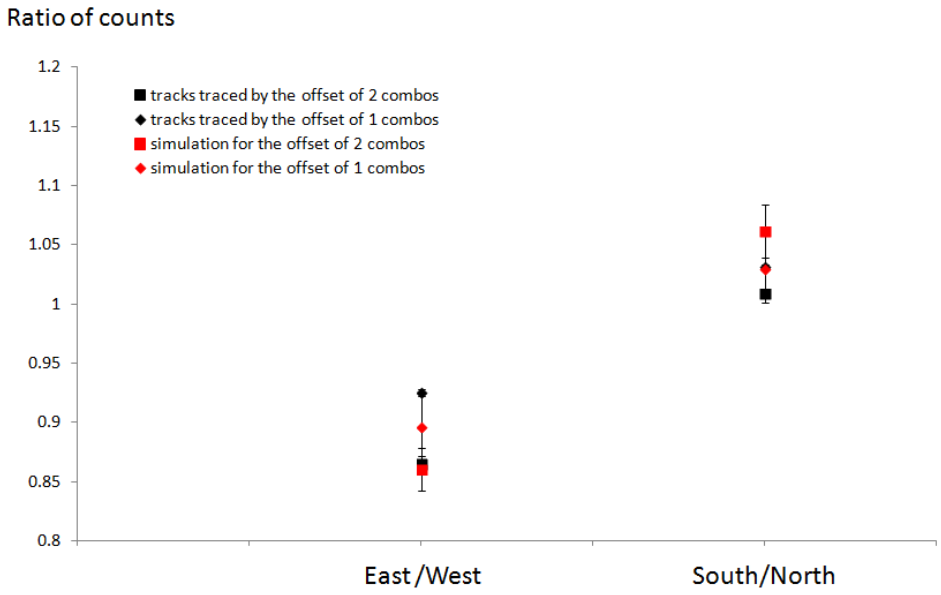

Figure 2.17: Ratios of counts of East to West and South to North in measurement and simulation.

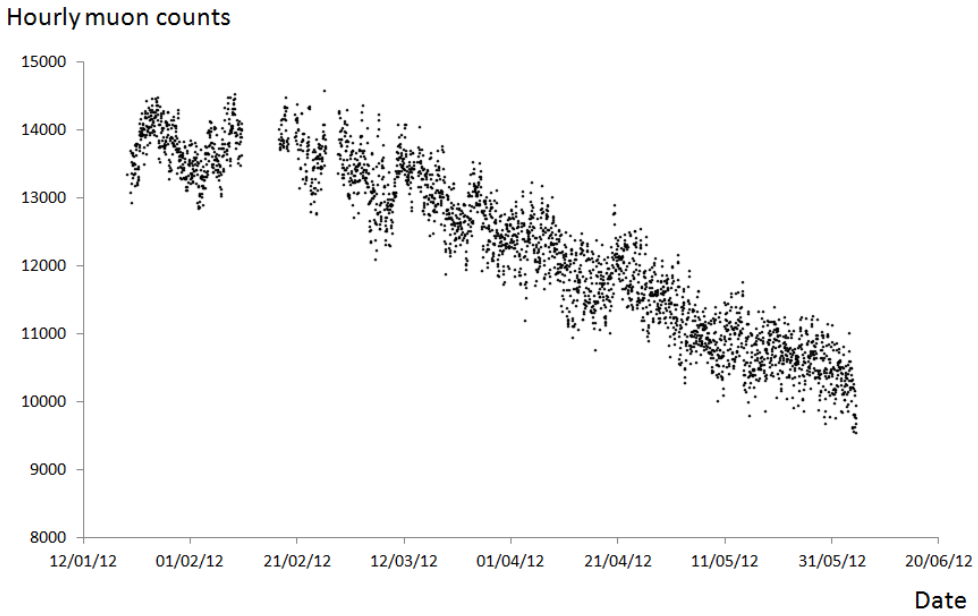

Figure 2.18: Time series of hourly counts of all triggering combos from 20^{th} Jan to 4^{th} June of 2012.

is due to a system crash. There are clear time variations of the CR count rates. The variation was correlated with meteorological conditions in different time scales (atmospheric effect).

Day-night variation

The periodic behavior of the series was analyzed by Fast Fourier transform in ROOT. The spectrum in the time domain of the series is shown in Fig. 2.19, where a peak at 24 hour period can be observed.

To analyze such 24-hour periodic behavior, hourly counts were averaged according to the daily local time over the entire time series. The result, called a 24-hour series, was shown in Fig. 2.20, where the errors were based on the statistical uncertainties given by square-root N. In the plot, an obvious day and night hourly count asymmetry was found, with more night counts than day counts. The

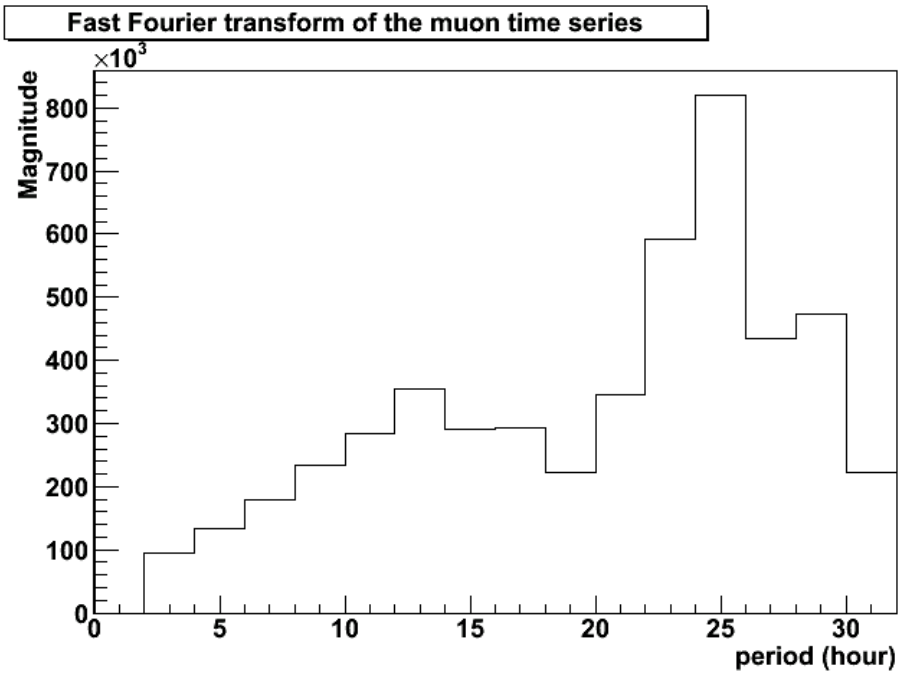

Figure 2.19: Fast Fourier Transform of the time series of muon count rates.

variation is about 2% from the mean. This behavior is believed to be caused by the daily variation of the atmosphere [28], details of which will be discussed soon.

Measurement and results

The trends shown in Fig. 2.18 and 2.20 were compared with the atmospheric surface pressure, surface temperature and ratio of surface pressure/ temperature, called the surface air density according to the ideal gas law. The data were taken by the weather station at the New Asia Astronomy Observatory Dome of CUHK. The comparisons were shown in Fig. 2.21, Fig. 2.22 and Fig. 2.23. In Fig. 2.21 and Fig. 2.22, the lines are the 24-hour moving averages of the data.

In Fig. 2.21 and Fig. 2.22, the data series were separated into two more groups, series of one-month moving average, called seasonal trends, and 24-hour moving average of the difference of the original data from the seasonal trends , called the

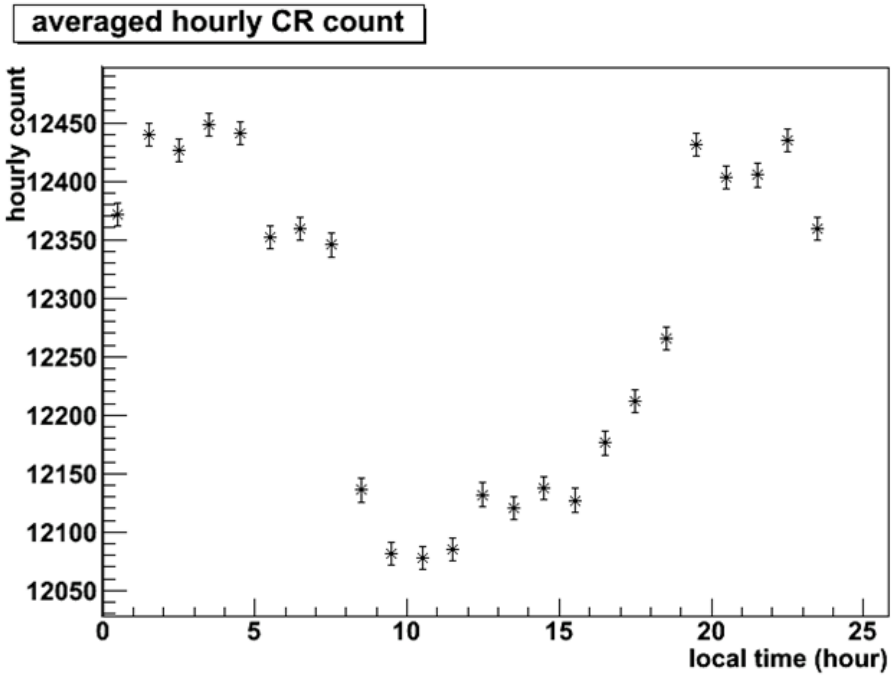

Figure 2.20: 24-hour series of the cosmic ray hourly counts, taken using the CUHK muon telescope in CUHK, averaged from the entire time series shown in Fig. 2.18

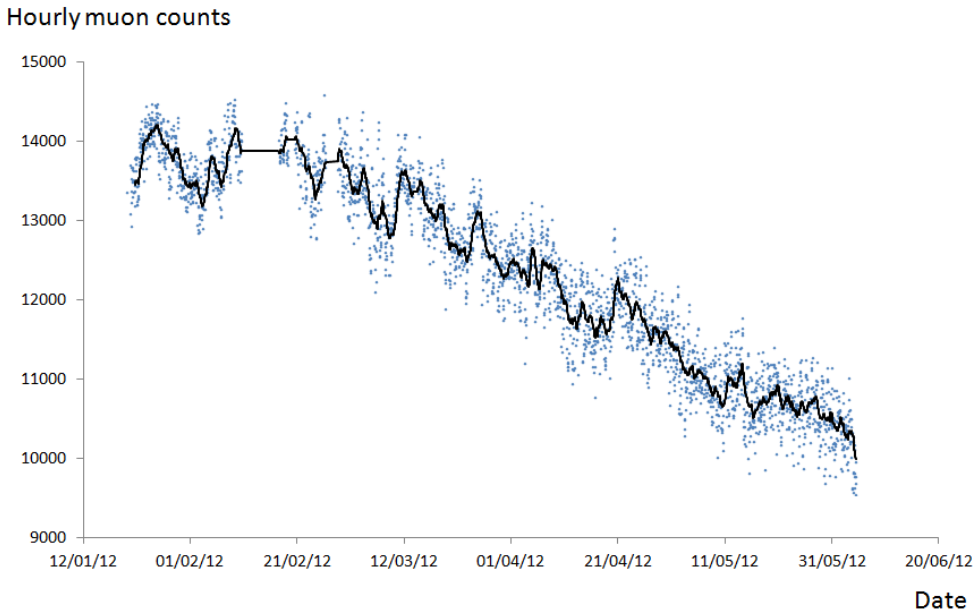

Figure 2.21: Time series of muon hourly counts. A line showing the 24-hour moving average of data was added.

monthly series. The series were shown in Fig. 2.24, Fig. 2.25, Fig. 2.26 and Fig. 2.27. For the seasonal trends, the muon counts kept decreasing during the summer time. The trend is consistent with other experiments [24, 46]. This is believed to be caused by the upward shifting of the production height during the summer [25].

The correlations between the muon counts and the atmospheric parameters were calculated,

$$\text{Correlation}(x, y) = \sum_{n=1}^{N} \frac{(x - \bar{x})(y - \bar{y})}{\sigma_x \sigma_y}, \tag{2.2}$$

where σ_x and σ_y are the standard deviations of x and y respectively. The results are shown in Table 2.2. A negative correlation between the muon counts and temperature were obtained. This is the negative temperature effect.

In order to examine the origin of such strong muon counts-temperature correlation, a temperature sensor was installed to monitor the room temperature

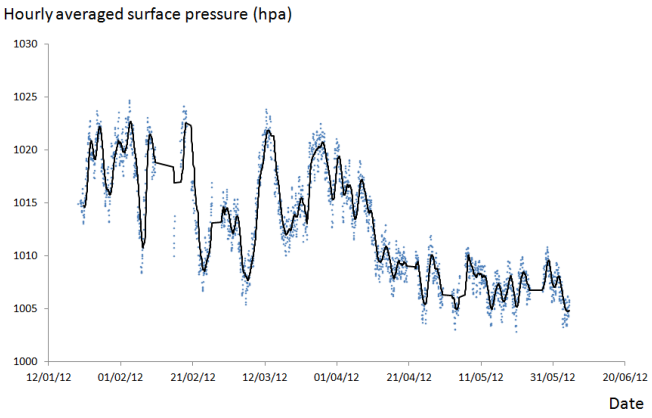

(a)

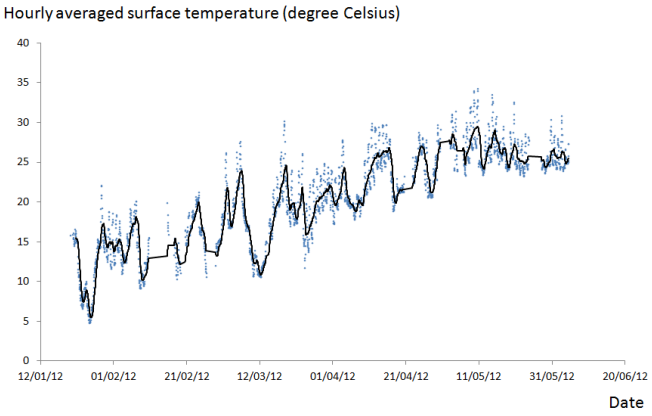

(b)

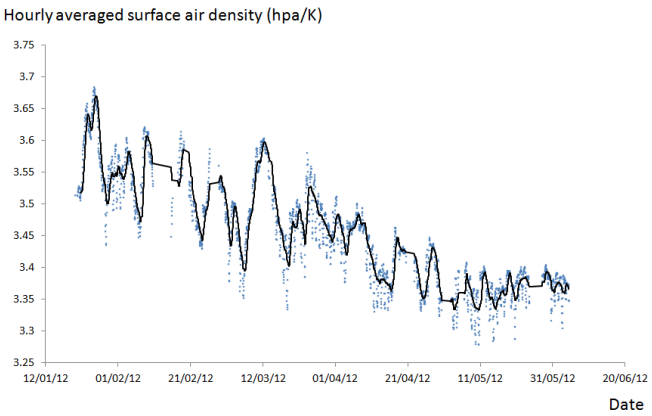

(c)

Figure 2.22: Time series of (a) hourly averaged surface pressure, (b) hourly averaged surface temperature and (c) hourly averaged surface air density, taken at the NA Observatory, CUHK. Lines showing the 24-hour moving averages of data were added.

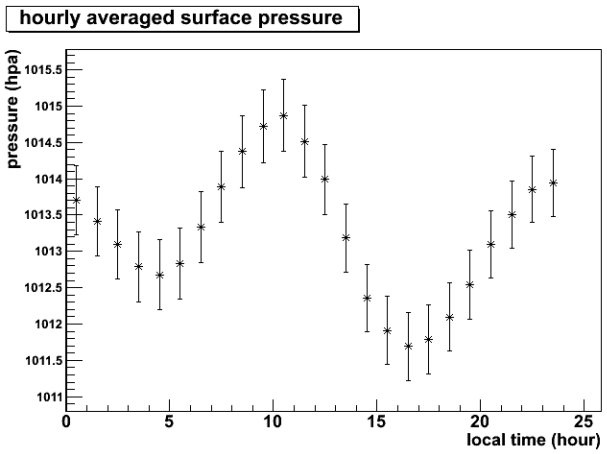

(a)

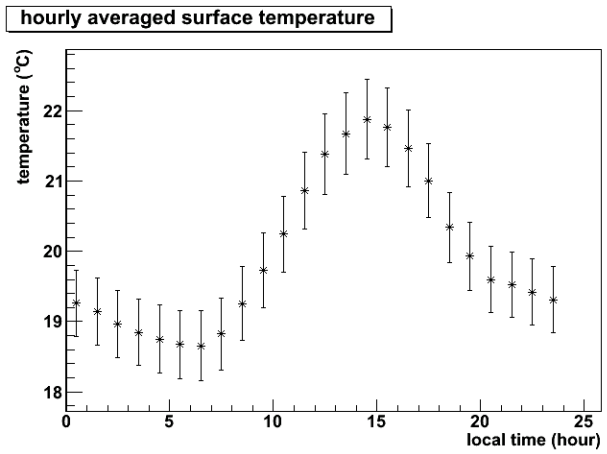

(b)

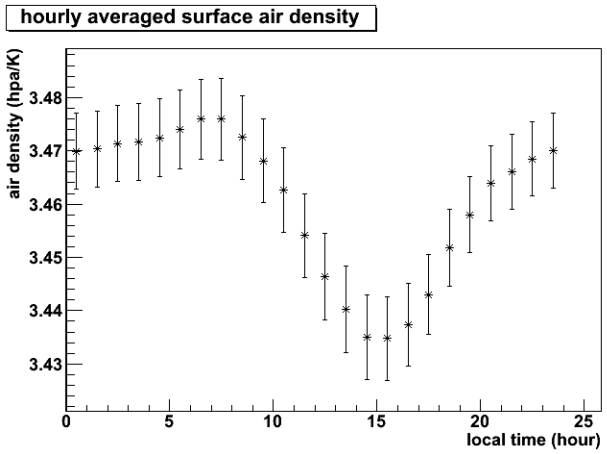

(c)

Figure 2.23: 24-hours series of (a) hourly averaged surface pressure, (b) hourly averaged surface temperature and (c) hourly averaged surface air density, taken at the NA Observatory, CUHK.

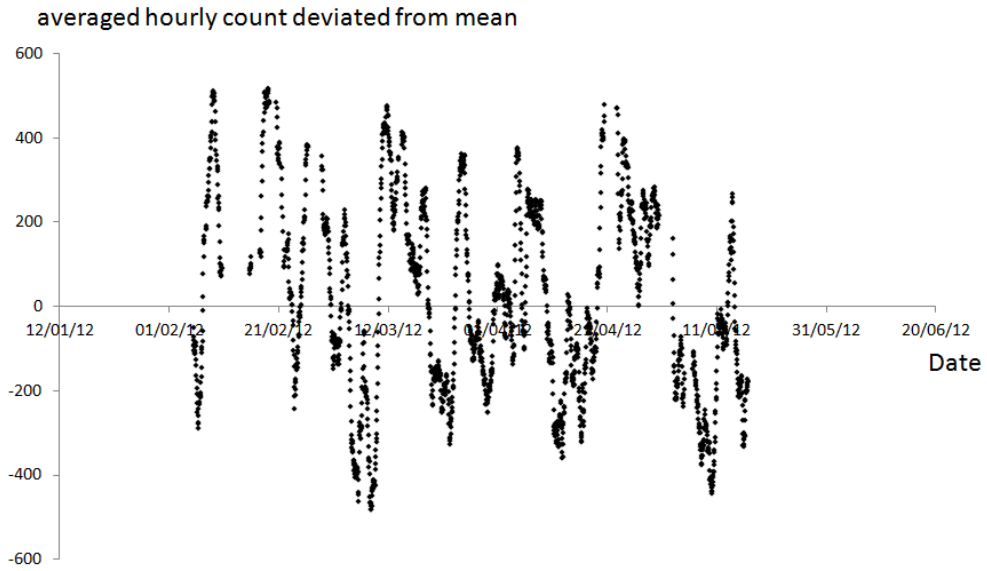

Figure 2.24: Monthly series of muon hourly counts

Table 2.2: Correlations between the muon counts and atmospheric parameters for different ranges of time moving average.

Time range of series	Correlation of muon counts and P	Correlation of muon counts and T	Correlation of muon counts and air density
24-hour series	-0.13	-0.78	0.68
Monthly series	0.35	-0.53	0.51
Seasonal trend	0.95	-0.98	0.99

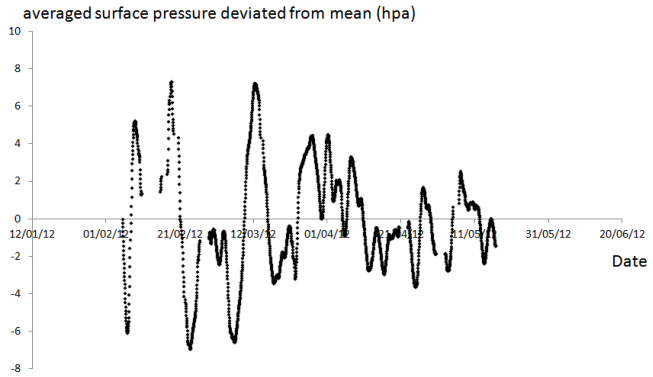

(a)

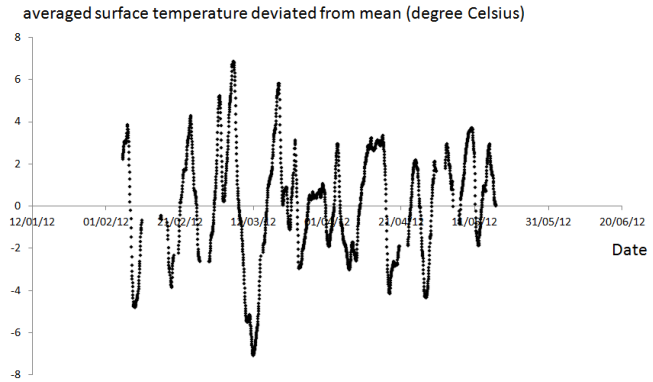

(b)

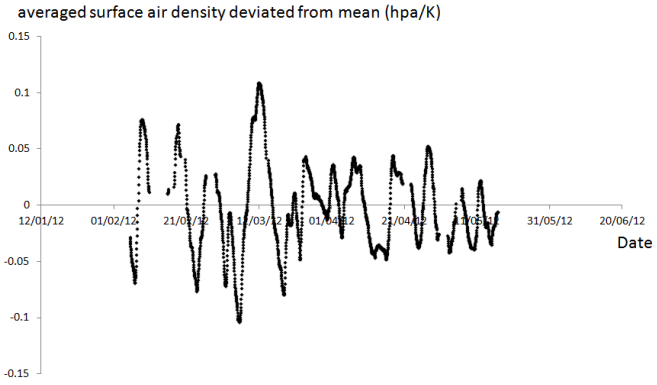

(c)

Figure 2.25: Monthly series of (a) surface pressure, (b) surface temperature and (c) surface air density, taken at the NA Observatory, CUHK.

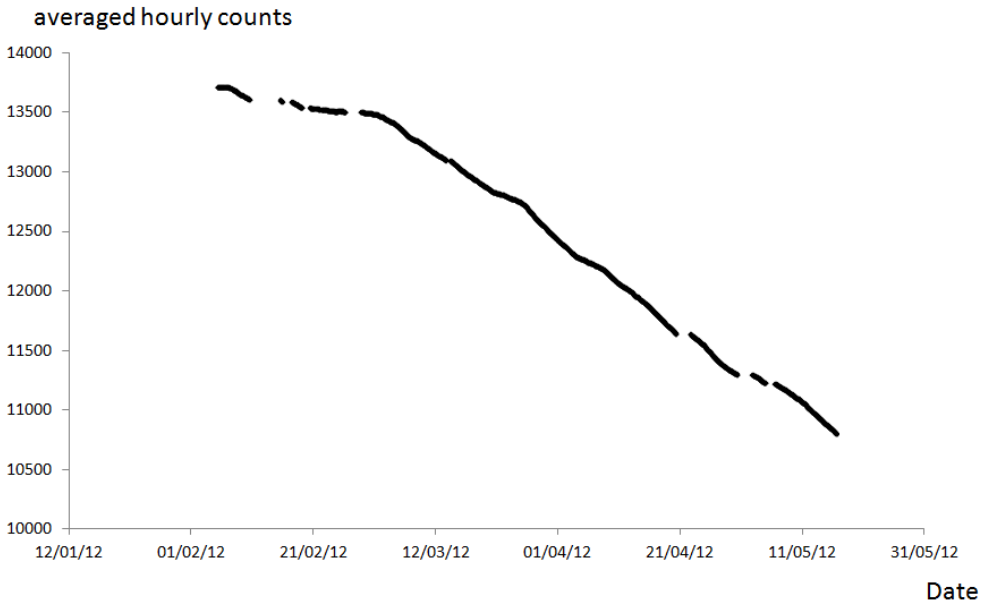

Figure 2.26: Seasonal trends of muon hourly counts.

together with the detector. The result is shown in Fig. 2.28. The room temperature is quite stable within $\pm$ 1°C for a day while the outdoor temperature changes by 5° to 10°C. These variations of the room temperature should have negligible influence on the detectors.

Modeling

A model for such correlations is developed. First, the primary cosmic ray particles, mostly protons, coming from outside the atmosphere would collide with air molecule nuclei to give pions, which decay to muons. The differential change of the number N_p of the protons with height h is written as :

$$\frac{dN_p}{dh} = \sigma \rho N_p, \tag{2.3}$$

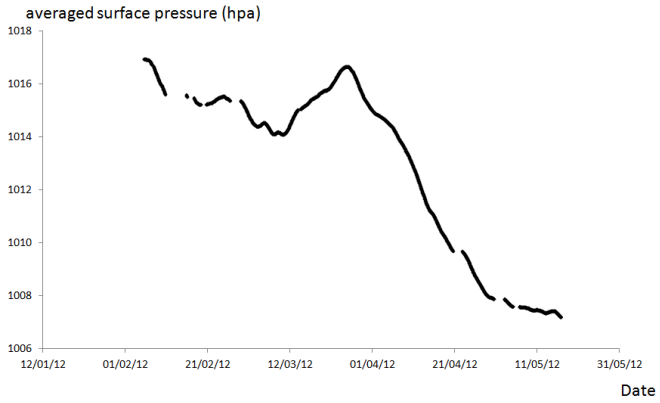

(a)

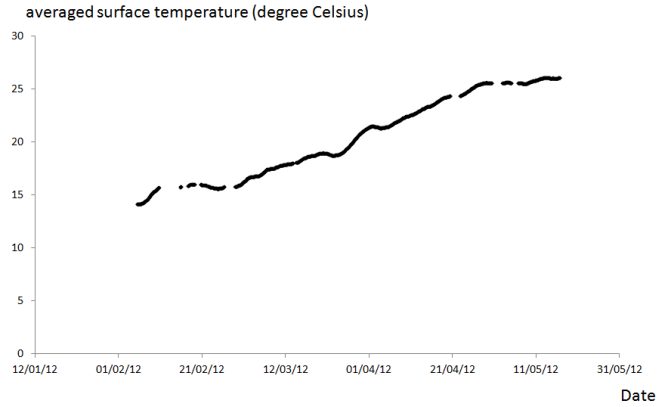

(b)

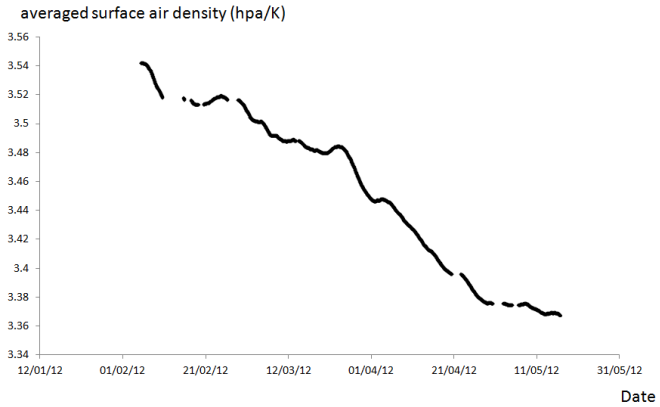

(c)

Figure 2.27: Seasonal trends of (a) surface pressure, (b) surface temperature and (c) surface air density, taken at the NA Observatory, CUHK.

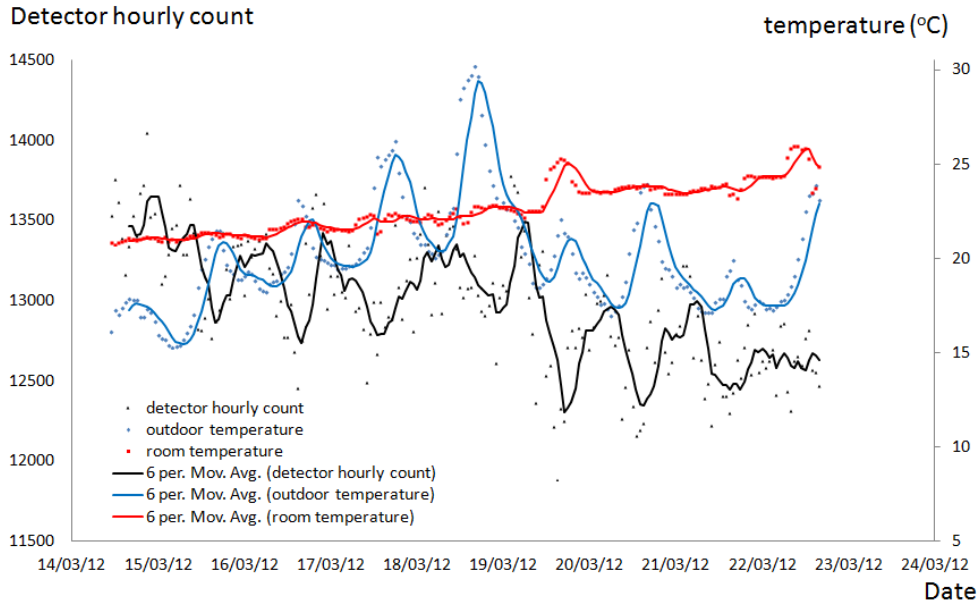

Figure 2.28: Comparison of muon counts, outdoor temperature (measured by the weather station) and room temperature (measured by a temperature sensor near the DAQ) in the NA Observatory, CUHK. Lines of moving averages of 6 hours were added.

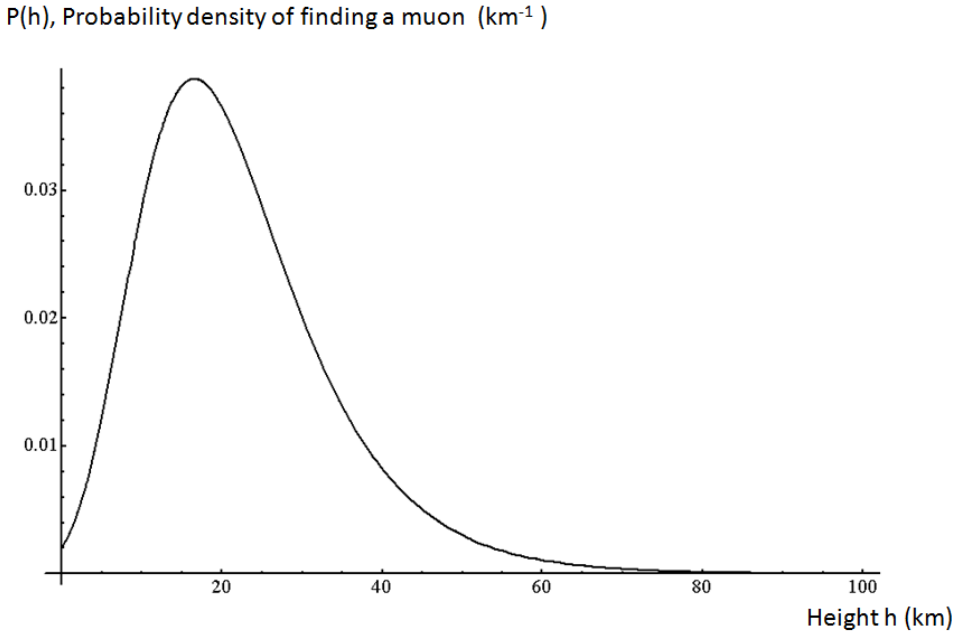

Figure 2.29: Probability density distribution of muon production at different heights of the atmosphere.

where $\sigma \approx 250$ mb is the proton-air molecule cross section [47], and ρ is the air density. The density profile of the atmosphere is assumed to be given by hydrostatic equilibrium:

$$\rho = \rho_\circ e^{-\frac{h}{h_\circ}}, \tag{2.4}$$

where $\rho_\circ = 1.2$ kgm^{-3} is the surface air density, $h_\circ = 9.5$ km is the scaled height. The differentiation of the solution of Eq. 2.3 gives the probability density P_{pcol} of collisions of the protons, also for the generation of muons, as a function of h:

$$P_{\text{pcol}} = \sigma\rho_\circ e^{-(\sigma\rho_\circ h_\circ e^{-\frac{h}{h_\circ}} + \frac{h}{h_\circ})}. \tag{2.5}$$

The plot of Eq. 2.5 is shown in Fig. 2.29, which shows a peak around $h = 16$ km.

The averaged energy spectrum $N_{p.h.}(E)$ of the generated muons for the production height around 10-20 km is simulated by Chan using GEANT4 [45]. The

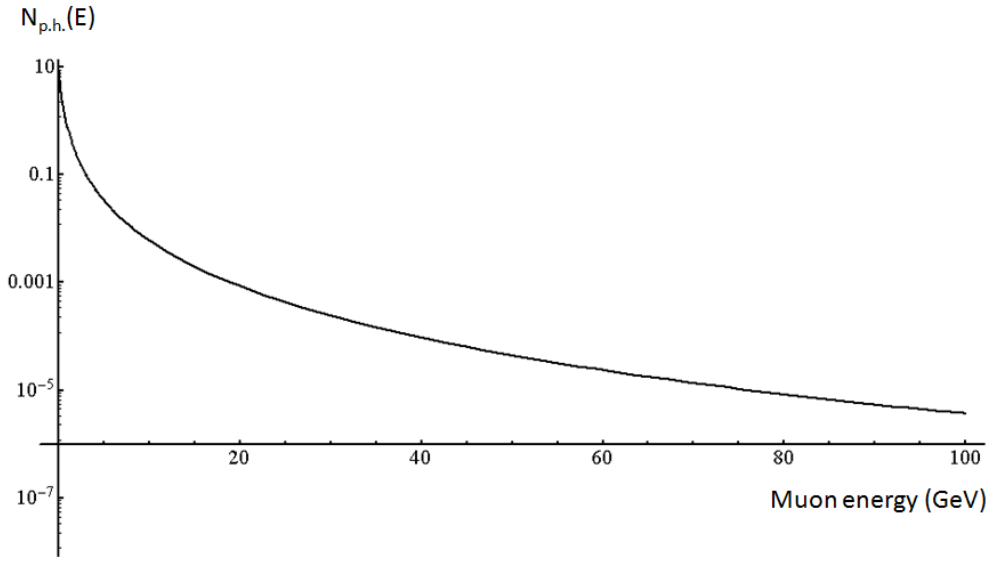

Figure 2.30: GENAT4 simulation by Chan of the averaged energy spectrum of the generated muons produced around 10-20 km. The best-fit values for the parameters are μ_f = -1.102 and σ_f = 1.436 in Eq. 2.6.

result is plotted in Fig. 2.30. A function,

$$A\frac{1}{E}e^{-\frac{(\ln E-\mu_f)^2}{2\sigma_f^2}}, \tag{2.6}$$

was applied to fit the curve for numerical calculation in later steps.

The change in the number of muons N_μ as they pass through the atmosphere is governed by muon decay Eq. 2.7 and muon stopping Eq. 2.8:

$$\frac{dN_\mu}{dt} = -\frac{N_\mu}{\tau\gamma}, \tag{2.7}$$

$$\frac{dE}{dx} = -a_{stop}\rho, \tag{2.8}$$

where τ = 2.2 μs is the muon life time, $\gamma = E/m_\circ$ is the Lorentz factor, with $m_\circ$ = 106 MeV is the rest mass of a muon, a_{stop} = 2.5 MeVcm^{2}g^{-1} is the muon

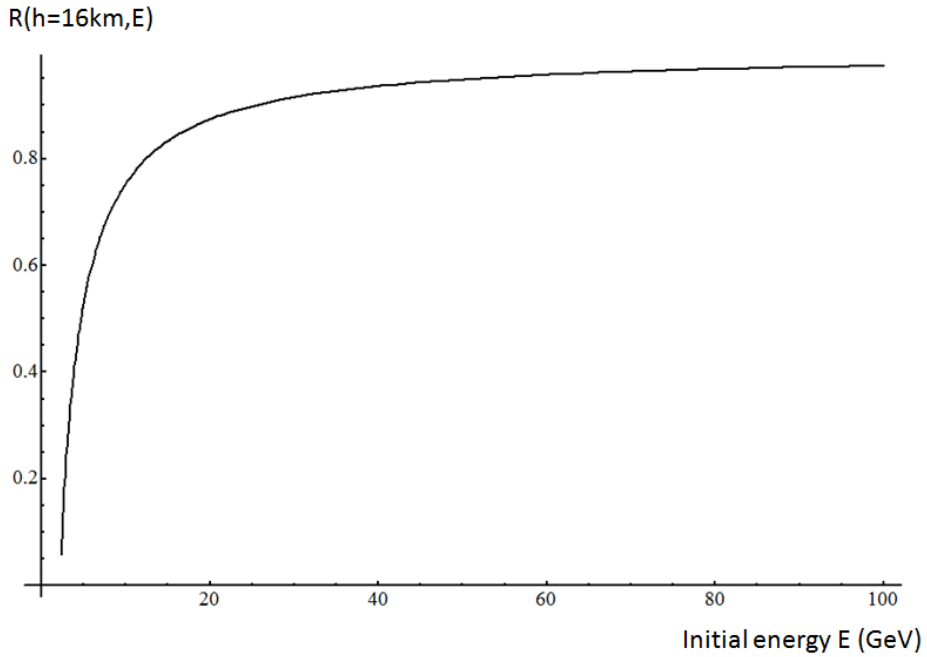

Figure 2.31: Fraction of muons reaching the ground from a production height of 16 km.

stopping power coefficient in air [44], ρ is the air density at height h according to the profile of Eq. 2.4. Hence, by solving the two differential equations, one obtains the fraction of muons reaching the ground $R(h, E)$:

$$R(h,E) = \exp\left[\int_{\frac{E}{m_\circ}}^{\frac{E}{m_\circ}+\frac{a_{stop}\rho_\circ h_\circ}{m_\circ}(e^{-\frac{h}{h_\circ}}-1)} \frac{h_\circ}{c\tau\sqrt{\gamma^2-1}(\frac{E}{m_\circ}+\frac{a_{stop}\rho_\circ h_\circ}{m_\circ}e^{-\frac{h}{h_\circ}}-\gamma)}d\gamma\right], \tag{2.9}$$

where E is the initial energy of the produced muon. $R(h, E)$ is numerical integrated for different initial energies E and production heights h. The result for $h = 16$ km is shown in Fig. 2.31 as an example. The plot shows that the fraction changes rapidly at low initial E, implying that the counts of low energy muons are sensitive to changes in the atmospheric density.

The muon energy spectrum N_{ground} received on surface from a certain produc-

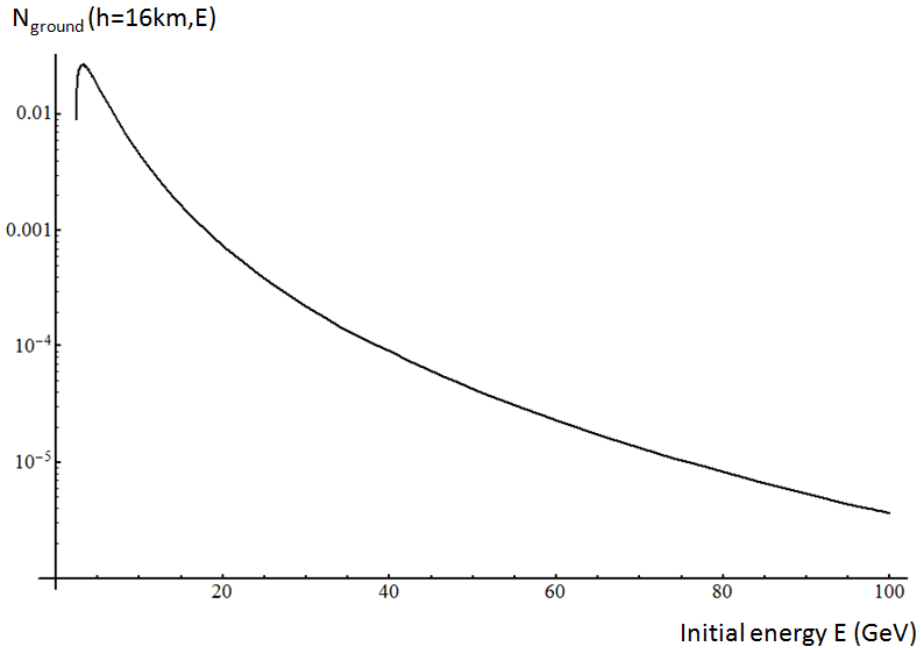

Figure 2.32: The energy spectrum N_{ground} of muons from a production height of 16 km.

tion height is obtained by:

$$N_{\text{ground}}(h, E) = N_{p.h.}(E)R(h, E). \tag{2.10}$$

The energy spectrum N_{ground} of muons from a production height of 16 km is shown in Fig. 2.32 as an example. There is a threshold of initial energy around 2 GeV for muons to reach the ground.

Finally, the number of muons reaching the ground N_μ is calculated by:

$$N_\mu = \int_{0km}^{100km} \int_{m_\circ + a_{stop}\rho_\circ h_\circ (1-e^{-\frac{h}{h_\circ}})}^{\infty} P_{\text{pcol}} N_{\text{ground}}(h, E) dE dh. \tag{2.11}$$

The mean energy of the muons from the model is calculated to be 4.8 GeV, which is close to the results of 4.4 GeV found by the modified Gaisser formula for vertical

muons.

The calculated N_μ is dependent on $\rho_\circ$ and $h_\circ$, which correspond to atmospheric changes. The dependence of the fractional change $\frac{\partial N_\mu}{N_\mu}$ on $\rho_\circ$ and $h_\circ$ is found by perturbing $\rho_\circ$ and $h_\circ$ separately. The results are shown in Fig. 2.33. From the plots, the ratios of the fractional changes are quite linear in the region of interest. Therefore, the fractional change of the muon counts $\frac{\partial C}{C}$, which is proportional to $\frac{\partial N_\mu}{N_\mu}$, is written as:

$$\frac{\partial C}{C} = a_c \frac{\partial \rho_\circ}{\rho_\circ} + b_c \frac{\partial h_\circ}{h_\circ}, \tag{2.12}$$

where a_c and b_c are the slopes determined from the linear fittings in Fig. 2.33, with a_c = -0.7 and b_c = -2.1. The dependencies are reasonable since the increases in $\rho_\circ$ and $h_\circ$ would increase the mass in the atmosphere. This would shift up the production height and hence make the muons travel through denser air for longer distances.

The total column mass $M_\circ$ of the atmosphere is found by:

$$M_\circ = \int_0^\infty \rho_\circ e^{-\frac{h}{h_\circ}} dh = \rho_\circ h_\circ. \tag{2.13}$$

The surface pressure is supposed to be proportional to the total column mass. This was proven by calculating the column mass from the measured density profile which was acquired from weather balloon measurement by the Hong Kong Observatory twice a day. A typical density profile of the measurement at noon of 1^{st} of May is shown in Fig. 2.34. The time series of the calculated total column mass and surface pressure $P_\circ$ are shown in Fig. 2.35. As expected, they show a good agreement. Hence, we assume:

$$M_\circ = kP_\circ, \tag{2.14}$$

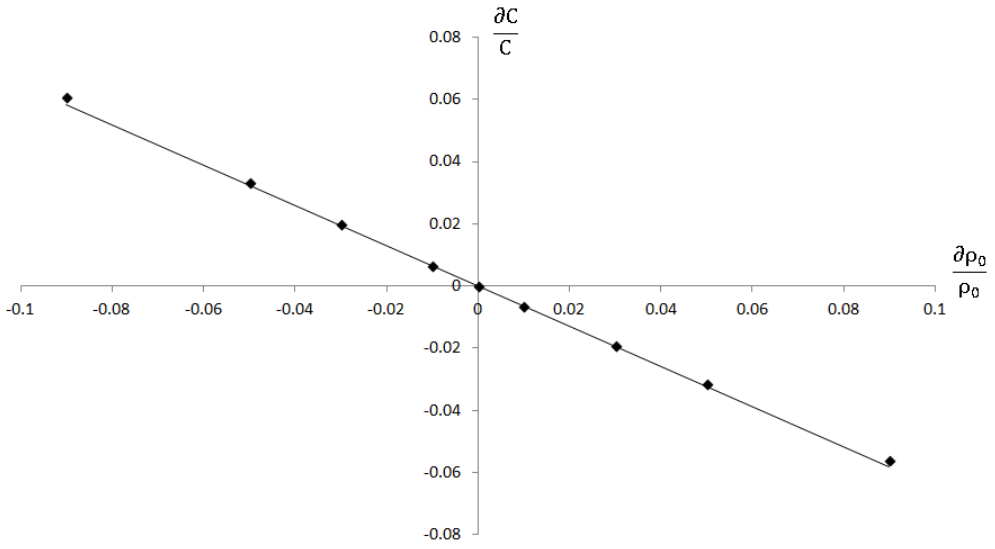

(a)

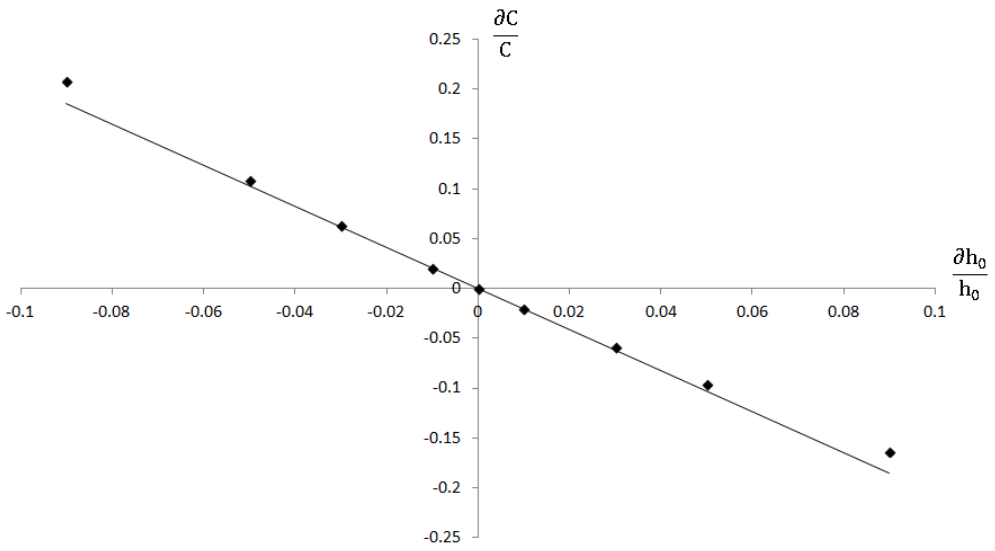

(b)

Figure 2.33: The fractional change of counts with perturbation of (a) surface air density $\rho_\circ$ at $h_\circ = 9.5$km, (b) scaled height $h_\circ$ at $\rho_\circ = 1.2$ kgm^{-3}.

where k is a proportional constant. Now Eq. 2.14 becomes:

$$kP_\circ = \rho_\circ h_\circ, \tag{2.15}$$

and therefore $h_\circ$ can be eliminated. Eq. 2.12 becomes:

$$\frac{\partial C}{C} = -\alpha_c \frac{\partial P_\circ}{P_\circ} + \beta_c \frac{\partial \rho_\circ}{\rho_\circ} = -2.1 \frac{\partial P_\circ}{P_\circ} + 1.4 \frac{\partial \rho_\circ}{\rho_\circ}, \tag{2.16}$$

where α_c and β_c were coefficients of surface pressure and surface density respectively. Alternatively, we can express $\frac{\partial C}{C}$ in terms of the surface pressure and temperature:

$$\frac{\partial C}{C} = -1.4 \frac{\partial T_\circ}{T_\circ} - 0.7 \frac{\partial P_\circ}{P_\circ}, \tag{2.17}$$

where -1.4 and -0.7 were coefficients of temperature and barometric effect, respectively, determined from the model. Eq. 2.17 shows the temperature and pressure dependencies with the cosmic muon counts, which agree with the correlations shown in Table 2.2 previously. Eq. 2.16 can be rearranged as:

$$\frac{\partial C}{C} + \alpha_c \frac{\partial P_\circ}{P_\circ} = \beta_c \frac{\partial \rho_\circ}{\rho_\circ}, \tag{2.18}$$

and hence:

$$\frac{\partial C_{correct}}{C_{correct}} = \beta_c \frac{\partial \rho_\circ}{\rho_\circ}, \tag{2.19}$$

where the pressure term can be regarded as a correction factor for the muon counts due to the increase in column mass of air. The effect of the increase of the surface air density would decrease the average production height and hence increase the muon counts.

The correction is applied to the data shown in Fig. 2.20 and 2.24 based on the form of Eq. 2.19 but leaving the coefficients as adjustable parameters. α_c was tuned first such that the correlation of the corrected muon counts – surface air

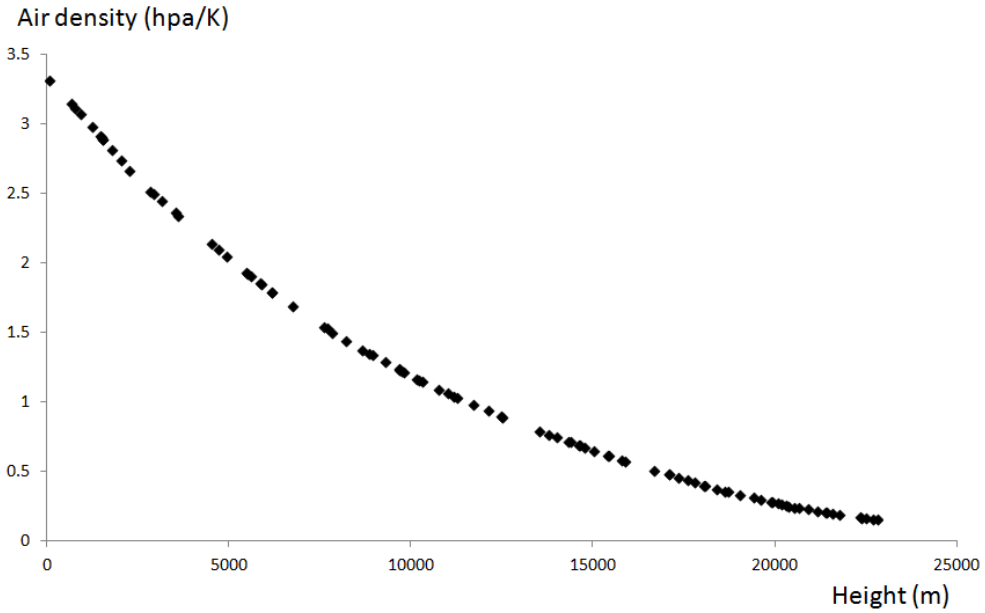

Figure 2.34: A typical density profile of the HKO weather balloon measurement at noon of 1^{st} of May.

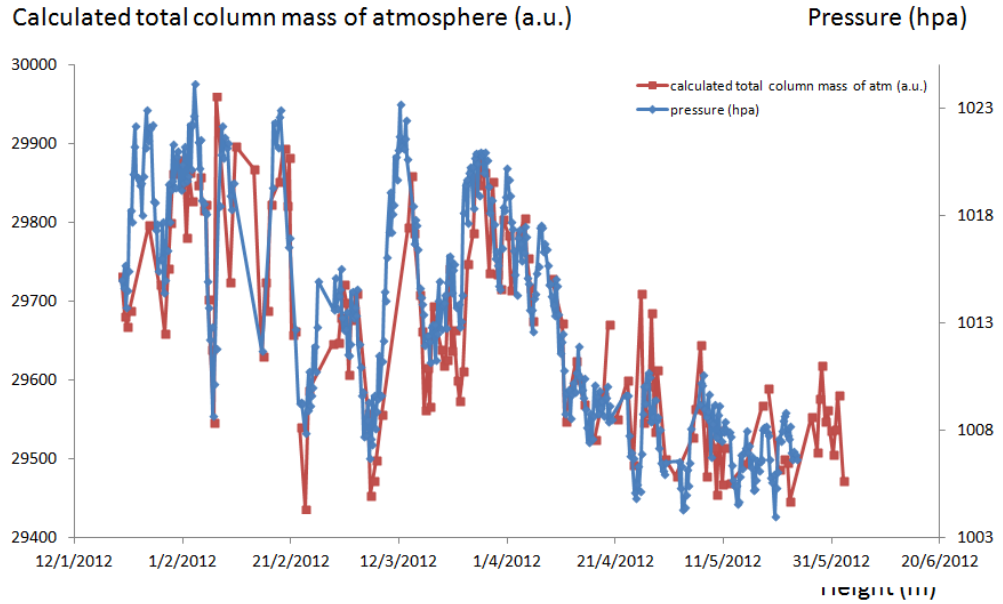

Figure 2.35: The time series of the calculated total column mass and pressure.

density is increased but not sensitive to the tuning. Then β_c was tuned to get a least-squared difference with the corrected muon counts. The tuned results are shown in Table 2.3 and the corrected muon counts plots are shown in Fig. 2.36 and 2.37. The dependence of the correlations on α_c are shown in Fig. 2.38.

Table 2.3: Tuned results and correlations between the muon counts (corrected muon counts) and the surface air density at different ranges of time moving average.

	α_c	β_c	Correlation of muon counts and surface air density	Correlation of corrected muon counts and surface air density
24-hour series	8	3	0.69	0.91
Monthly series	5	0.6	0.55	0.79

After the correction, the correlation of the muon counts and surface air density has been increased. However the coefficients deviated by a few times from the results of the model in Eq. 2.16. This can be due to the simplified assumptions used in the model, such as the hydrostatic equilibrium density profile, energy dependence of the proton - air cross section and muon stopping in air, absence of the pion decay model and the 10-20 km averaged energy spectrum of muon from the simulation. Despite the deviations of parameter values from model expectation, the complicated physics of the CR generation and time dependence can be captured in such a simple model. Taking the averaged values of α_c and β_c in Table 2.3 and expressing the fractional change of the muon counts in the form of Eq. 2.17 gives:

$$\frac{\partial C}{C} = -1.8\frac{\partial T_\circ}{T_\circ} - 4.7\frac{\partial P_\circ}{P_\circ}, \tag{2.20}$$

or:

$$\frac{\partial C}{C} = -0.6(\%/^\circ C)\partial T_\circ - 0.5(\%/\text{hpa})\partial P_\circ, \tag{2.21}$$

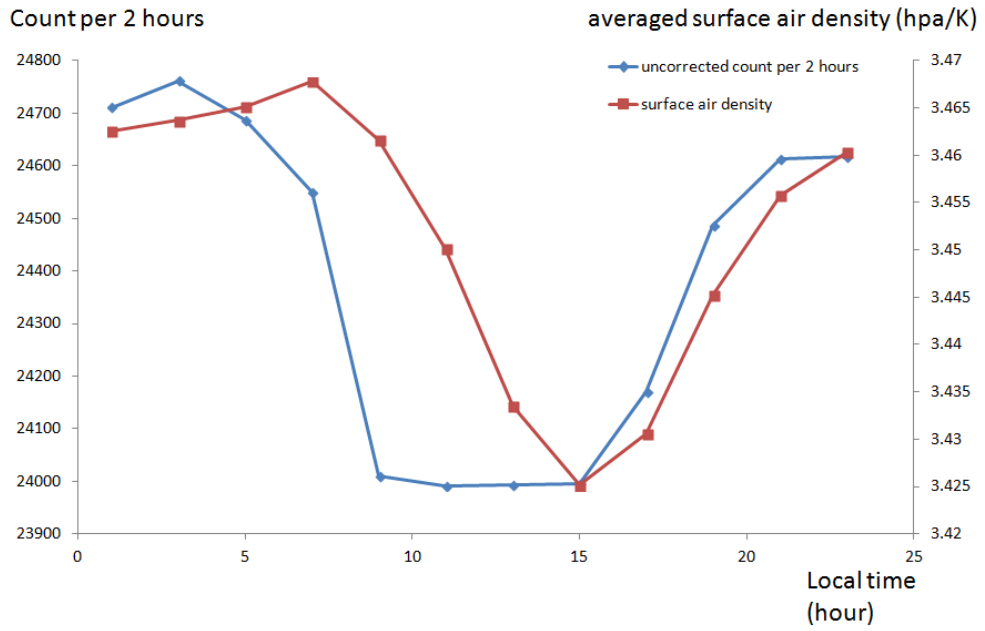

(a)

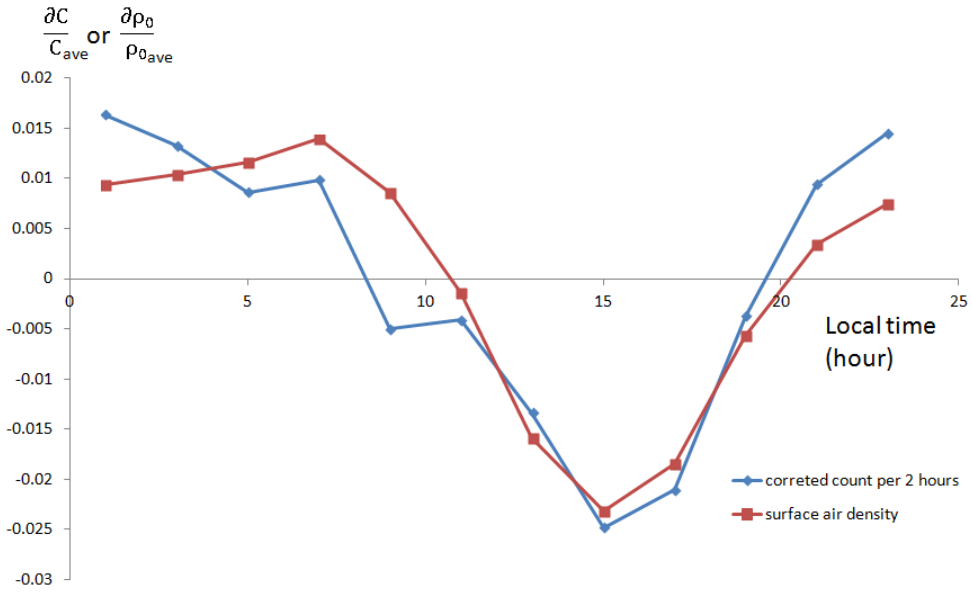

(b)

Figure 2.36: Comparison of time series of muon counts and surface air density. (a) Uncorrected muon counts and (b) corrected muon counts in 24-hour series.

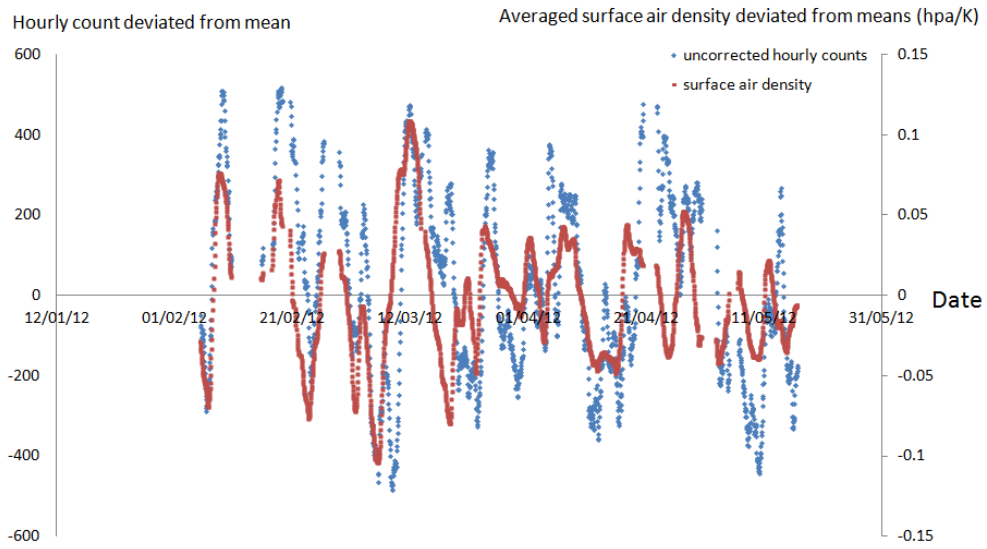

(a)

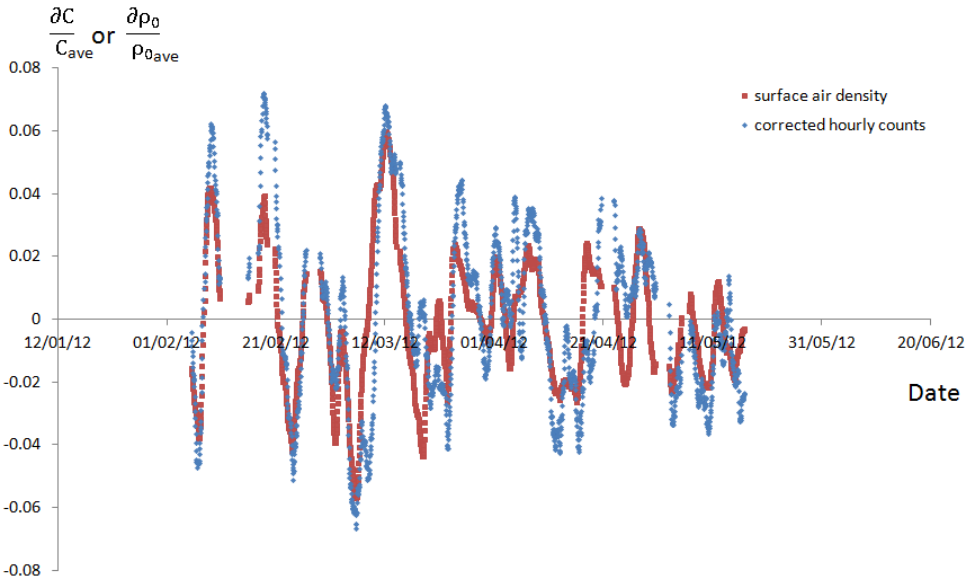

(b)

Figure 2.37: Comparison of time series of muon counts and surface air density, using (a) uncorrected muon counts and (b) corrected muon counts in monthly series.

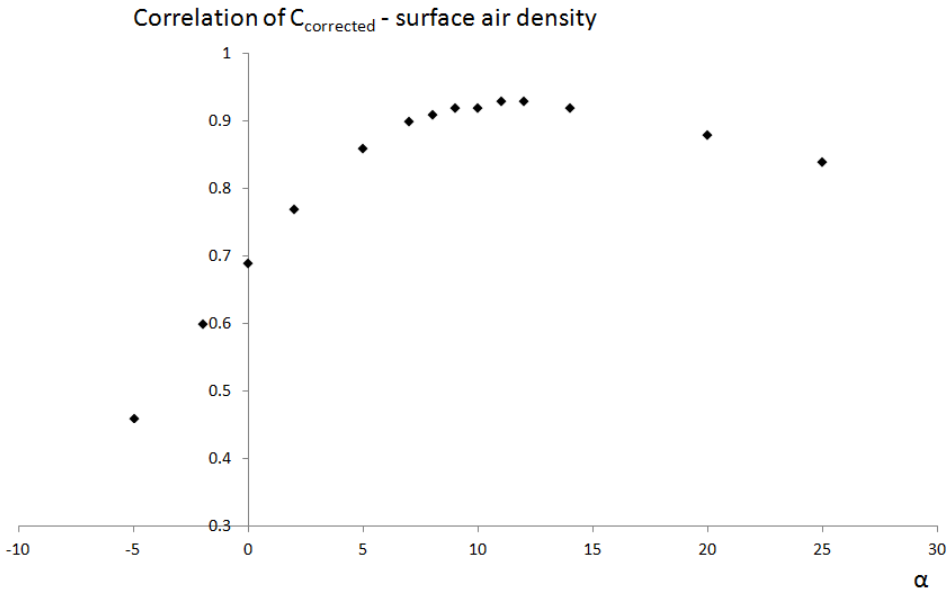

(a)

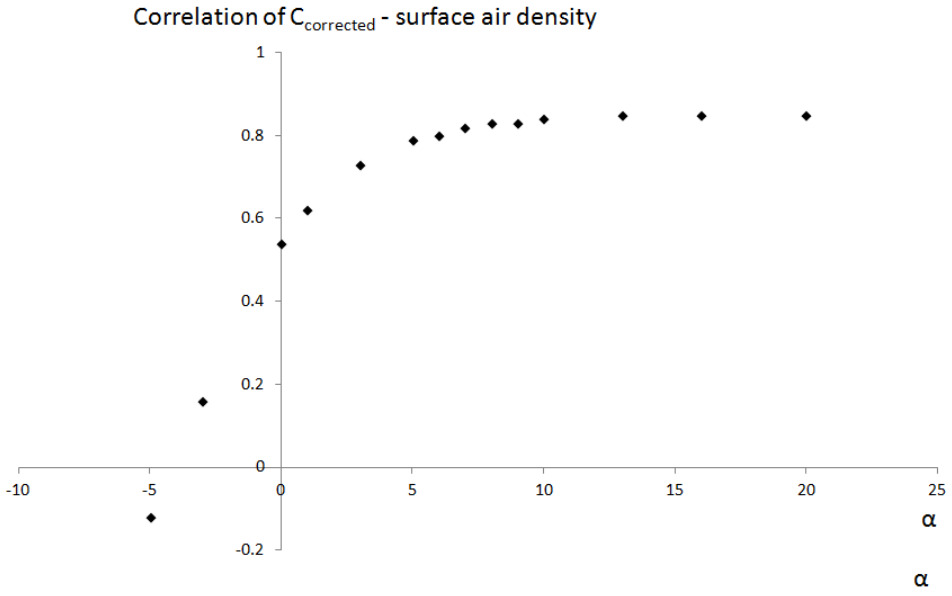

(b)

Figure 2.38: Dependence of correlation of corrected muon counts – surface air density on α for (a) 24-hour series, and (b) monthly series.

at the standard values of $T_\circ = 293$ K and $P_\circ = 1010$ hpa. The results are close to the other experimental results [24, 26].

Chapter 3

The Aberdeen Tunnel Experiment

The purpose of the Aberdeen Tunnel Experiment is to study muon induced neutrons and muon flux angular distribution in an underground laboratory where the environment is similar to those of the Daya Bay experimental halls. These studies can be a useful reference for the cosmogenic background for the neutrino measurement in Daya Bay.

The Aberdeen Tunnel Laboratory is located at 22.23°N and 114.6°E, in the cross tunnel of Aberdeen Tunnel. The vertical overburden is around 235 m of mostly granite, which is equivalent to 611 m water depth. Fig. 3.1 shows a 3D map of the mountain profile near the laboratory. Mount Nicholson and Mount Cameron, each of over 400 m in height, are nearby, making an overburden asymmetry, with more overburden in the southeast and west directions.

The rock compositions of the Aberdeen Tunnel and Daya Bay experimental sites were compared by X-ray fluorescence spectroscopy [48]. The results are shown in Fig. 3.1 The compositions are very close to each other, and hence the background radiations from the rocks are more or less the same.

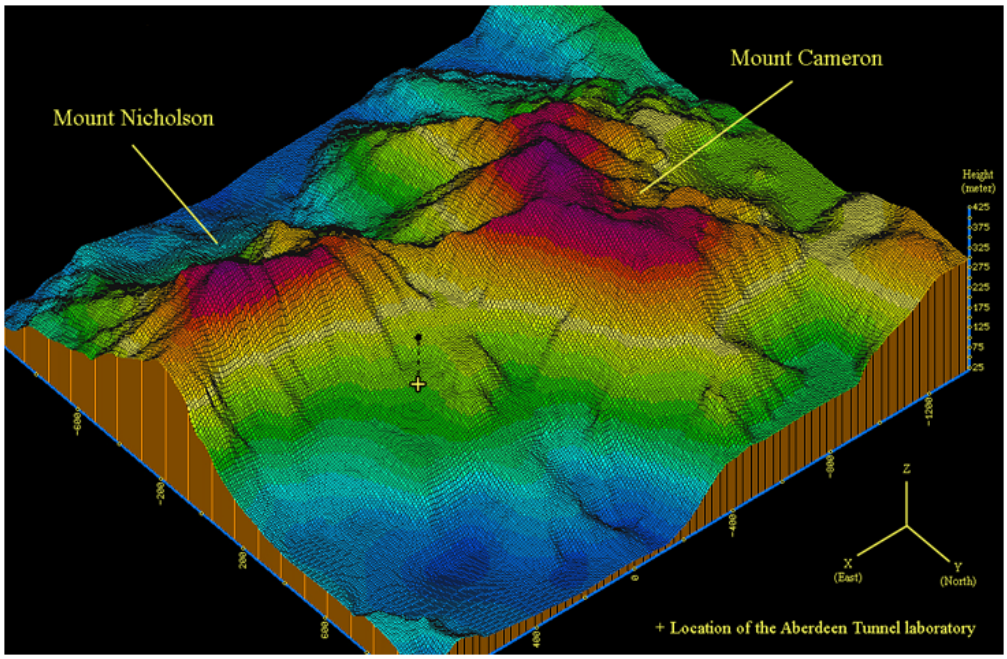

Figure 3.1: A 3D map of the mountain profile near the Aberdeen Tunnel Laboratory located at (0, 0, 22), indicated by the cross. This map is generated by T. Kwok [48].

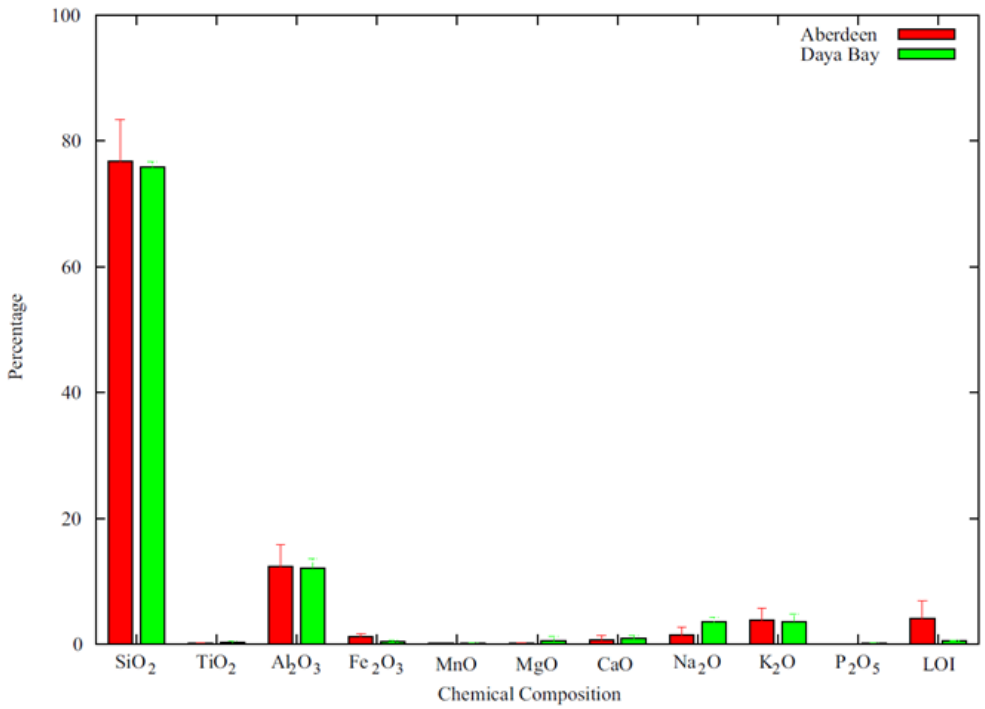

Figure 3.2: Rock Compositions of the Aberdeen Tunnel Laboratory and Daya Bay experimental halls measured by XRF. The figure is adapted from Luk [49].

3.1 Detector Configuration

The detector in the Aberdeen Tunnel Laboratory consists of two parts, the muon tracker and neutron detector. The muon tracker tracks the incoming muons and gives a prompt signal to the neutron detector which detects neutrons produced by the muons.

3.1.1 Muon tracker (MT)

The configuration of the tracker was similar to the CUHK muon telescope. A schematic drawing is shown in Fig. 3.3. There are ten hodoscopes in each layer. The details of the hodoscopes and PMTs are shown in Table 3.1. Each hodoscope consists of a plastic scintillator, light guide and PMT. The structural details were similar to the hodoscopes of the CUHK muon telescope, as discussed in Chapter 2.

There were 6 layers of hodoscopes, with each layer orthogonally oriented with respect to its neighbours, to give a 10x10 grid structure in 3 levels, where the grid sizes were 2.54 cm x 2.54 cm. The top and middle level separation was 22 cm while the separation for the middle and bottom levels was 181 cm. In between the levels, sheets of 2 mm lead were placed to block the background gamma radiations.

Table 3.1: Details of the hodoscopes and PMTs in the Aberdeen Tunnel muon tracker.

Hodoscope	Dimensions (cm)	PMT (photocathode diameter)	Orientation
1 m	100 × 10 × 2.54	1 × EMI PMT (2 inch)	East-West
1.5 m	150 × 10 × 2.54	1 × EMI PMT (2 inch)	North-South
2 m	200 × 9.3 × 2.54	2 × H7826 SPMT (1.9 cm)	North-South

All detectors were placed on a steel frame as shown in Fig. 3.3. The upper

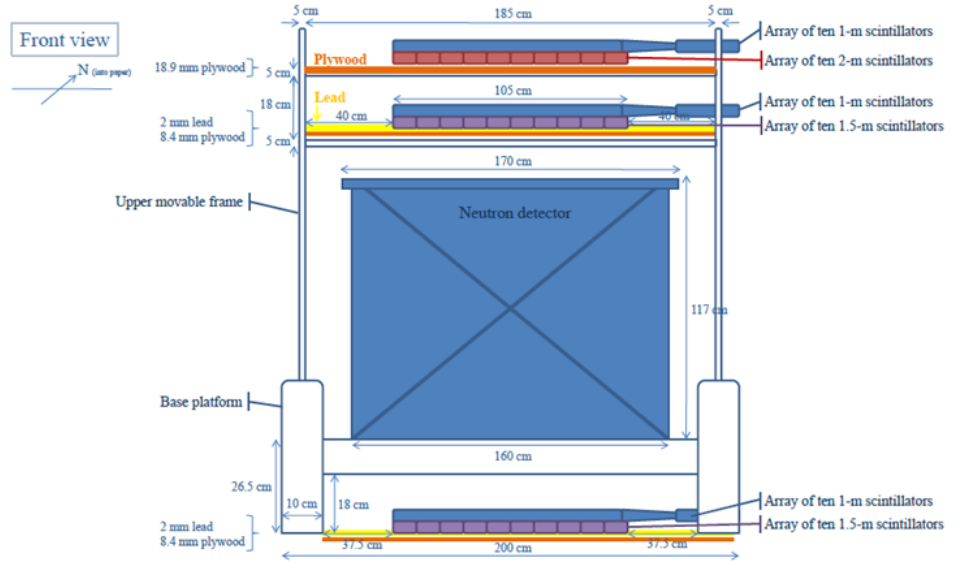

(a)

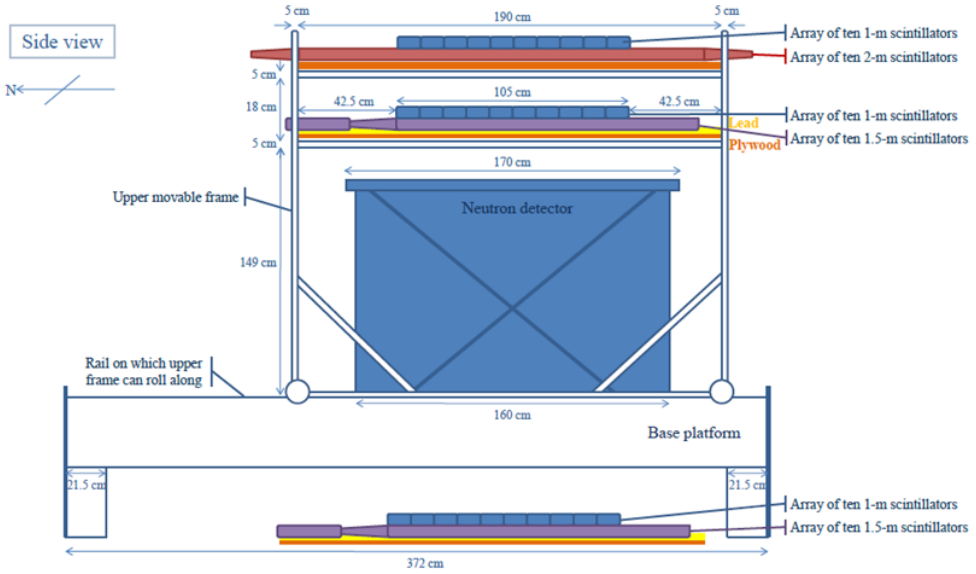

(b)

Figure 3.3: Schematic drawing of the muon tracker and the neutron detector, (a) Front and (b) Side, in Aberdeen Tunnel Laboratory. The figure is adapted from Lau [50].

frame, with top and middle levels laid on, was movable so that the centers of the grids can be aligned vertically.

3.1.2 Neutron detector (ND)

The neutron detector (ND) was sandwiched in between the centers of middle and bottom levels as shown in Fig. 3.3. The structure of the ND is shown in Fig. 3.4. A cylindrical acrylic vessel with inner diameter of 110 cm, which has above 80 % transmittance at 350 nm of light [48], was sitting in the center of stainless steel tank with inner dimensions of 160 cm (L) $\times$ 160 cm (W) $\times$ 117.3 cm (H).

0.65 ton of Gadolinium doped liquid scintillator (Gd-LS) and 1.63 ton of mineral oil (MO) were filled in the acrylic vessel and the stainless steel tank respectively. There were 3 calibration ports for deploying calibration sources on the acrylic vessel and the stainless steel tank. They were the central port (C port), north port (N port) (25 cm away from center) and south port (S port) (45 cm away from center). A calibration box was put on the ports of the top lid of the stainless steel tank for deploying the sources. Details of the calibration box will be discussed in the calibration section. There are also gate valves and an overflow tank [48] on the top lid of the ND.

Sixteen 8-inch diameter Hamamatsu R1408 PMTs were located in the corners of the stainless steel tank. There were 4 PMTs in each corner forming a ring structure of four PMTs at 4 different heights. Two specular reflectors of 140 cm diameter, with reflectivity 95% [51], were attached to the top and bottom inner surfaces of the stainless steel tank, in order to increase the PMT coverage and thus minimize the loss of scintillation photons. Besides, four diffusive reflectors were attached to the inner side surfaces of the stainless steel tank for improving the uniformity of the energy response and also minimizing the loss of scintillation photons. The details of the fabrication and structure of the ND were discussed by

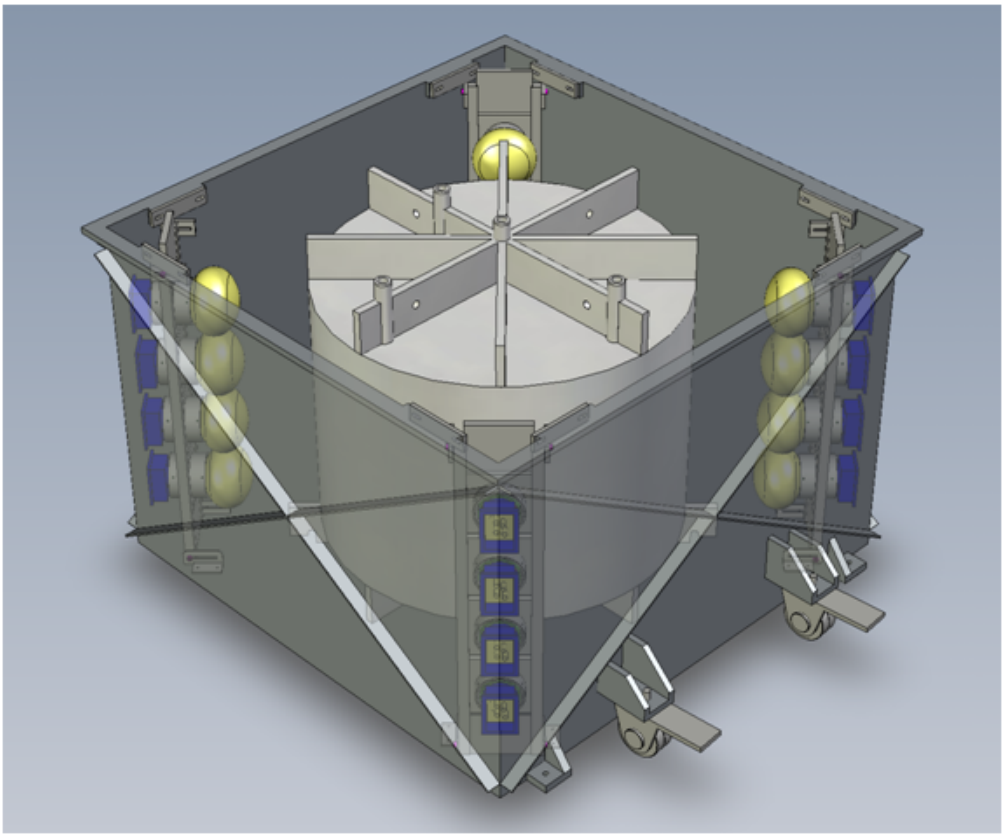

Figure 3.4: Drawing of the inner structure of neutron detector from Ngai [52]. A cylindrical acrylic vessel is sitting in the center of a stainless steel tank. Sixteen 8" diameter PMTs are located on the corners of the stainless steel tank. Top lid cover and reflectors are not shown here.

Kwok [48].

3.2 Detection mechanism

3.2.1 Muon tracker

The physics of the muon detection of the Aberdeen Tunnel hodoscopes was the same as that of the CUHK muon telescope, details of which were discussed in Chapter 2. Tracks can be reconstructed from the hit patterns of the hodoscopes.

3.2.2 Neutron detector

The ND is used to detect free neutrons in its active volume. Neutrons are thermalized in the mineral oil or GD-LS, in about 20 μs. The thermalized neutrons are then captured either by hydrogen or Gadolinium. For the hydrogen (^{155}Gd, ^{157}Gd) capture, with cross section of about 300 mb (60 kb, 250 kb) [53], the process gives a total of about 2.2 MeV (8 MeV) of gamma radiations, which are converted into scintillation photons in the liquid scintillator. Some of the photons may escape detection. As a result, the detected captured energy would be smaller than the expected value. Therefore, a buffer region of MO has to be filled in the region of PMTs to separate the PMT from the liquid scintillator. This can increase the photon detection coverage and hence the energy resolution. In addition, the MO also absorbs unwanted fast neutrons and gamma radiations coming from outside or the PMT glass. In order to minimize the refraction and reflection of scintillation light coming from the Gd-LS region, the refractive indices of the MO, acrylic vessel and the Gd-LS were matched.

The number of photons detected by the PMTs depends on the solid angles of the PMTs as viewed from the source, the photon reflection from the reflectors and photon attenuation in liquids. The energy and position of an event can be reconstructed by an iteration procedure. The procedure is to vary the trial source energy and position, so as to match the calculated result with the measured number of photons received by each PMT.

3.3 Data Acquisition (DAQ)

Schematic of the DAQ of the experiment is shown in Fig. 3.5. It was divided into two parts, one each for the muon tracker and the neutron detector.

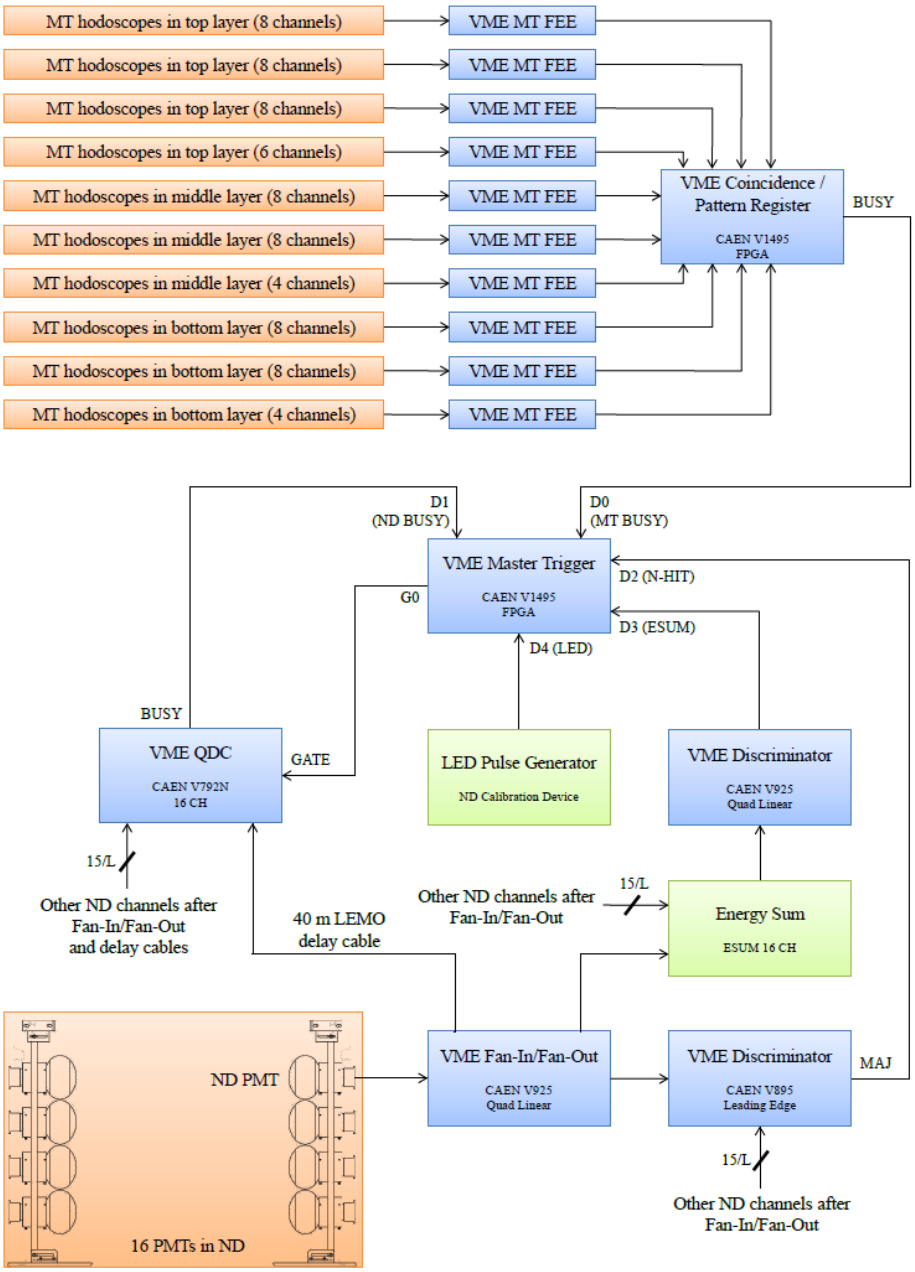

Figure 3.5: Schematic of the DAQ of the experiment, adapted from Ref. [52]. Blocks in blue can be configured remotely through the VMEbus.

3.3.1 Muon Tracker

Similar to the DAQ of the CUHK muon telescope, the outputs of the Aberdeen Tunnel hodoscopes are connected to the FEE. There are ten mother boards of FEE, each having four daughter boards. Each daughter board has two channels for the hodoscopes. First, in the daughter board, the signal from a hodoscope is inverted and amplified. The amplified signal is then processed in the discriminator by comparing with a threshold of 35 mV. The output of the discriminator goes to a fast flip-flop for handling input pulse widths down to 400 ps, which cannot be processed by the circuit of monostable. The flip-flop outputs a logic signal of ECL pulse greater than 4 ns to the monostable circuit. The monostable circuit outputs an adjustable width to determine the trigger time window of the True logic signal of the ECL. Currently the width is set to be 100 ns. Fig. 3.6 and 3.7 show the schematics of the inverted amplifier, the discriminator, the flip-flop and the monostable. The mother board, with inserted daughter boards, provides power and 10-bit DAC setting for the threshold and the output width of ECL in the monostable. Such mother boards are inserted in a VME crates, a CAEN SY1527LC power supply system.

The logic signals are then processed in a VME module of CAEN FPGA V1495 with 100 MHz clock. Similarly, the FPGA processes the coincidence and the event builder for the hit pattern and timestamp, similar to that discussed in Chapter 2. The triggering condition is set to be 4-fold coincidence, with 2x and 2y. Before the event words are read out by the computer, they are stored in a buffer with size of 500. The computer reads the data from the VME crate through a high speed USB 2.0.

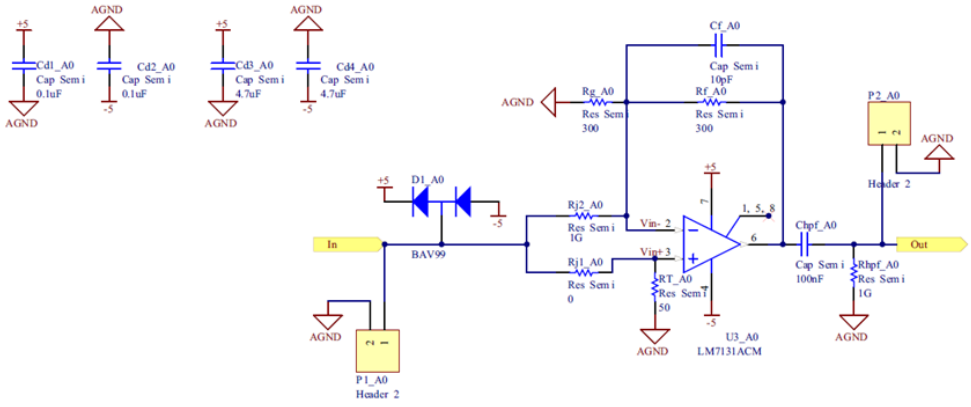

(a)

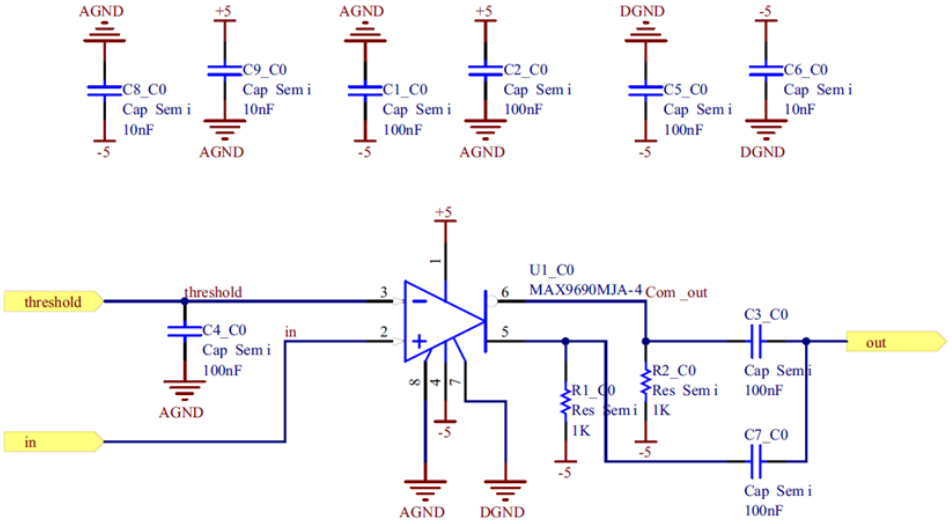

(b)

Figure 3.6: Schematics of the FEE by Y.C. Lin and K.K. Kwan. (a) Schematic of the inverted amplifier. (b) Schematic of the discriminator.

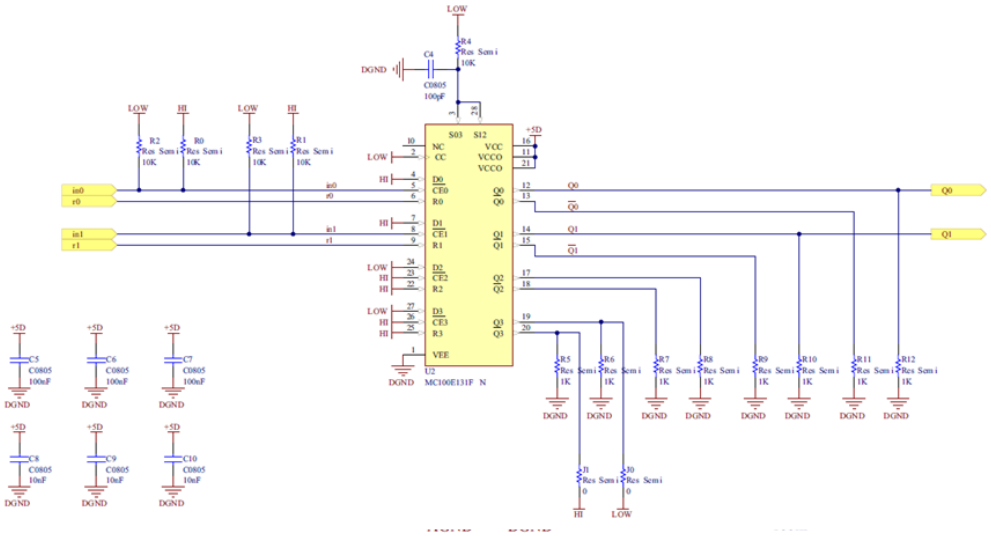

(a)

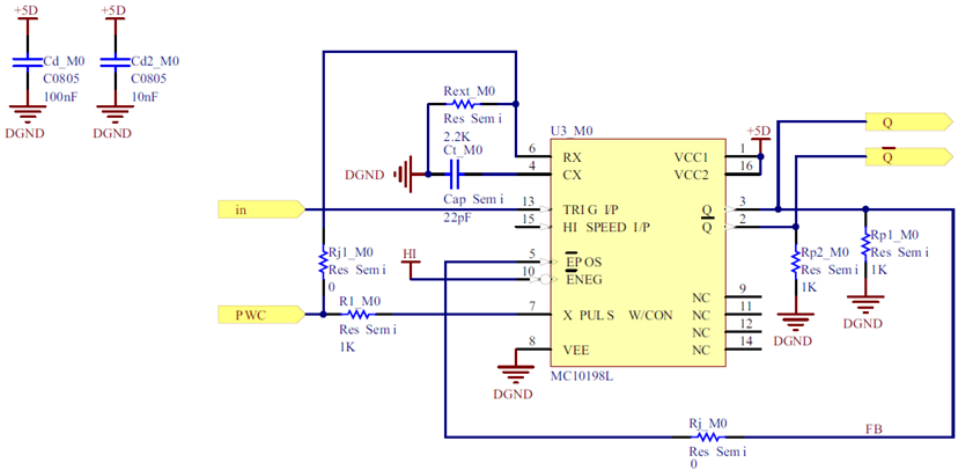

(b)

Figure 3.7: Schematics of the FEE by Y.C. Lin and K.K. Kwan. (a) Schematic of the flip flop. (b) Schematic of the monostable.

3.3.2 Neutron detector

As shown in Fig. 3.5, the outputs of 16 PMTs are connected to the VME module of linear fan-in/fan-out, which outputs three copies of input signals. One copy goes to a VME module of charge-digital converter (QDC) (CAEN V792N, 12 bits resolution, 100 fC/count) for PMTs' charge measurement. The other two go to an energy sum module (ESUM) and a discriminator of n-hit majority (NHIT) (CAEN V895).

A schematic of the ESUM module is shown in Fig. 3.8. The module includes a summing amplifier with adjustable gain, shaping and inverting amplifier and buffer amplifier [54]. The performance, of summing various numbers of identical 20 ns width pulses, is shown in Fig. 3.9. The R^2 of linear fitting is 0.998. A discriminator, CAEN V925, with threshold of -96 mV (-6 mV x 16) is used to discriminate the summed signal. True logic of the trigger is given to the VME master trigger board (MTB), another FPGA module of CAEN V1495 with 100 MHz clock.

For the n-hit majority triggering, each PMT signal is discriminated with a threshold of -6 mV first. If the number of channels passing the comparison is greater than or equal to the selected number of majority, a true logic of the trigger is sent to the MTB.

The jobs of the MTB are generation of gates for QDC, prescaling triggers of the NHIT and the ESUM modules, and processing the event builder for timestamp. The QDC measures charge only when it received a gate signal coming from the MTB. The criteria of gate generation are shown in Fig. 3.10. The criteria can be conceptually divided into two parts, muon correlated and muon uncorrelated. For the muon correlated events, it would first trigger the tracker. The MTB receives a MT BUSY signal, from the module of VME Coincidence/ Pattern Register, and then the MTB generates a true logic called MT time window, with a width of

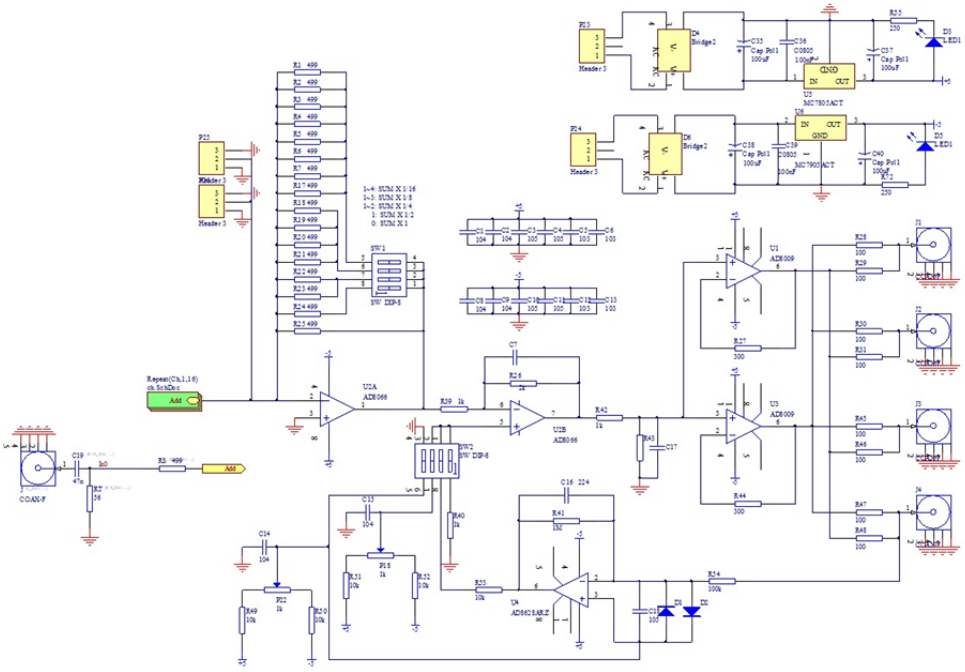

Figure 3.8: Schematic of ESUM module [54] used in the Aberdeen Tunnel ND.

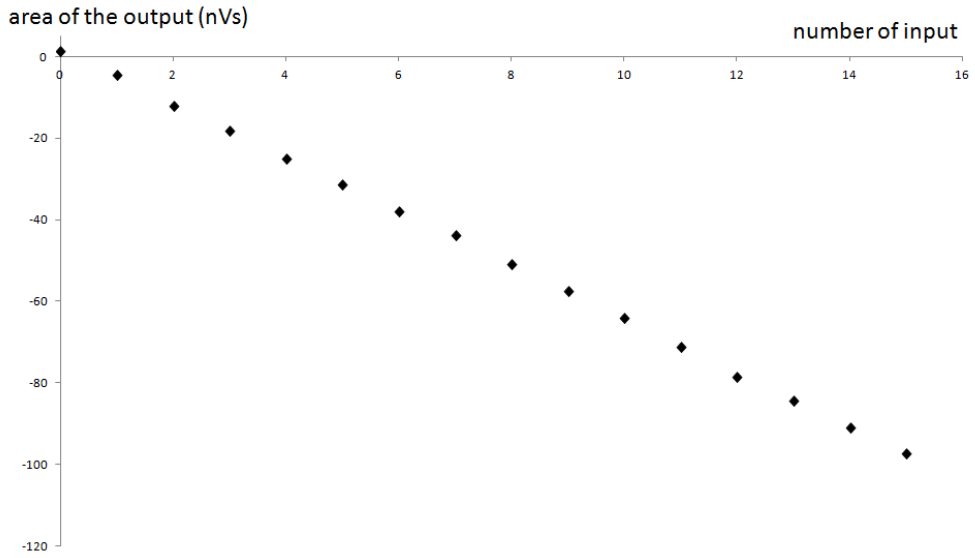

Figure 3.9: Area of the summed output against various input numbers of identical 20 ns width pulses in the ESUM module.

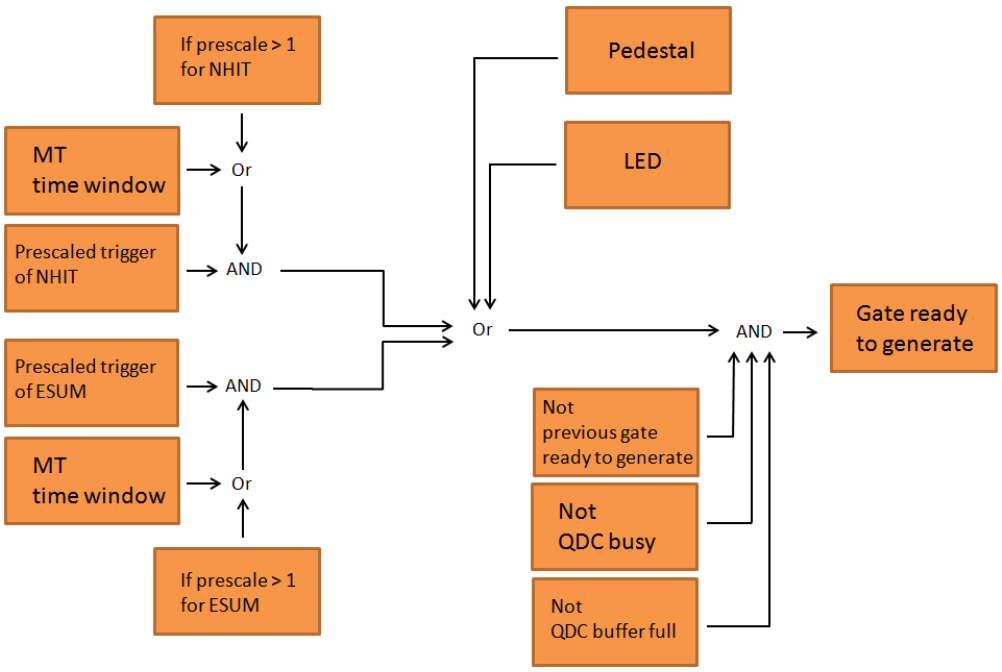

Figure 3.10: Schematic of the logic flow for generation of the gate for the QDC.

about 100 ms. During the time window, if there is a prescaled trigger (currently, no prescale) from the NHIT or the ESUM passing the three "NOT" conditions - no previous order of gate generation, not busy of QDC and not full of QDC buffer - a gate is ready to be generated. After 40 ns, a gate with 300 ns width is sent to the QDC. The reason of the delay of the gate generation is to match the arrival times of the gate and the PMT signals reaching the QDC.

Currently, only the background, which is muon uncorrelated, is prescaled by 1000 with the ESUM trigger. Other muon uncorrelated triggers are the pedestal and LED. They are also required to pass the three "NOT" conditions for the gate generation. The pedestal is a periodic trigger of 50 Hz, which is used for triggering the QDC to monitor its offset for the charge measurement. The pedestal can correct the offset in real time. The LED trigger (not yet completed) is used for the PMT linearity calibration. After all, the event builder of the MTB records the

trigger type and the time stamp of the trigger. The event word is stored in a 32 sized buffer. Typically, the time difference between an MT trigger and the follow ND trigger is about 100 ns.

The QDC receives the gate and delayed PMT signals, through 40 m LEMO cables, and then starts the charge measurement. During the measurement, a busy logic signal of about 5.7 μs width, called the QDC dead time, is sent to the MTB. After that, the 12-bit charge value is stored in the 32 sized buffer. The computer reads the data from the MTB and QDC in the VME crate through a high speed USB 2.0 interface.

3.3.3 Software and setup connection

A schematic of the setup connection for the experiment is shown in Fig. 3.11. The front end computer is connected to two VME crates, for the MT and the ND, the calibration device, and the slow control system. The slow control system contains temperature and humidity sensors for environmental monitoring, ND calibration system and power supply system CAEN SY1527 for the PMT high voltage.

The communications are programmed by a software called MIDAS. It also manages the routines of the buffer management, the message system, the history system and the online database (ODB). All of the software are written in C language and running on LINUX operation system. The back end computer is connected to the front end computer via TCP/IP for data storage. Details of the software are discussed in Ref. [52].

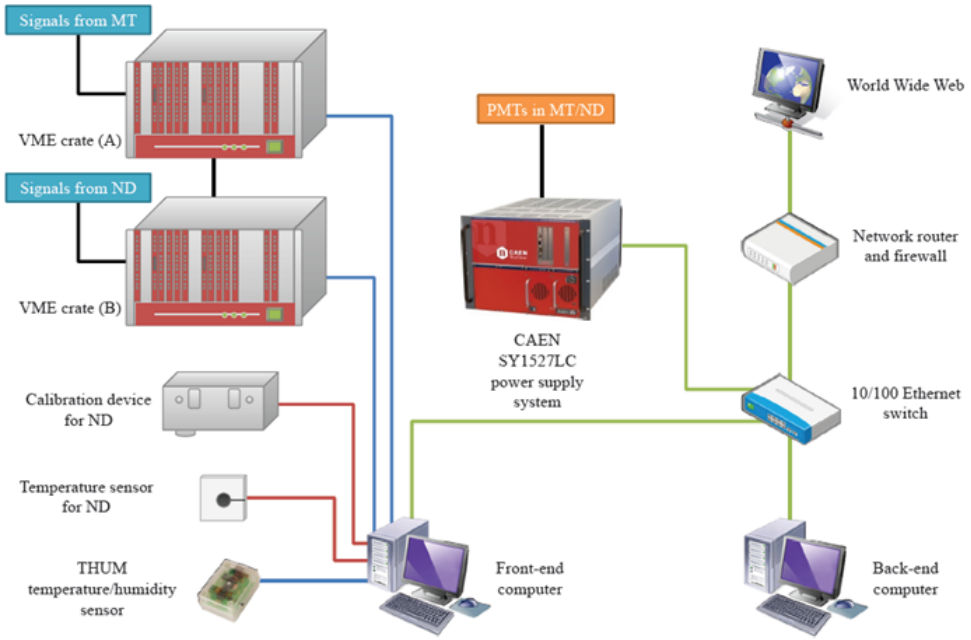

Figure 3.11: Schematic of the setup connection for the experiment, adapted from Ref. [52]. Lines in black: signal or power cable, green: Ethernet, blue: USB and red: RS232.

3.4 Calibration

3.4.1 Muon Tracker

For the muon flux measurement, the tracker counts have to be corrected by its angular response, defined by:

$$R(\theta, \phi) = A(\theta, \phi)\epsilon(\theta, \phi), \tag{3.1}$$

where A is angular effective area of the tracker, and ϵ is the angular efficiency of the hodoscopes. Ngai [52] worked out ϵ by Monte Carlo simulation. It was based on finding the number of muons counted, resulting from incidence of an isotropic muon flux to the tracker with the hodoscope arrangement, as shown in Fig. 3.3. The measured efficiencies of each individual hodoscope were input in the simulation. The hodoscopes were calibrated to be operating at the plateau region, where the efficiency is optimized with an appropriate high voltage applied. The plateau region of each individual hodoscope were found out by Lau in the University of Hong Kong by measuring the ratio of counts with triggering conditions of 3-fold to 2-fold at different high voltages [55]. The measured average efficiencies of the hodoscopes were about 95%. Using the inputs in the simulation, the equation for ϵ [52] was:

$$\epsilon(\theta, \phi) = \frac{N_{\text{eff}}(\theta, \phi)}{N_{\text{trg}}(\theta, \phi)}, \tag{3.2}$$

where N_{eff} was the number of muons triggering the real tracker (with $< 100\%$ efficiency for each hodoscope) and N_{trg} was the number of incoming muons triggering an ideal muon tracker (100% trigger efficiency for each hodoscope). The calculation of the angular effective area was based on the projection method, as discussed on Chapter 2. The angular response distributions for 2-x 2-y and 3x-3y triggering conditions were shown in Fig. 3.12 and 3.13. The errors shown in

Fig. 3.12(b) and 3.13(b) were propagated from the statistical uncertainties of the efficiency measurement and simulation. The uncertainty was dominated by the measurement except at the edge region where the statistics of the simulation was insufficient.

3.4.2 Neutron detector

Radioactive gamma sources ^{241}Am-Be, ^{60}Co and ^{137}Cs were used for the calibration of the ND. The calibration included PMT gain, energy scale of the QDC, energy resolution and energy response linearity.

Calibration device

All of the calibration sources were placed into a liquid proof acrylic source holder. The calibration was carried out through a motorized device called the calibration box. The schematic of the calibration box with source holder is shown in Fig. 3.14. The source holder was tied to a Teflon wrapped steel cable which was supported by the acrylic wheel B and rolled to the acrylic wheel A. The stepping motor rotated the acrylic wheel A through the rubber belt, so that the position of the source holder can be controlled. The limiting switch prevents breaking of the steel wire when the motor overshoot the home position of the source holder. This was because the motor would be stopped when the source holder hit the limiting switch. Besides, an IR camera was used to monitor the position of the source holder and whether it was resting in the home position when opening or closing the gate value, which was connecting the ND to the calibration box. An IR LED provided lighting for the camera inside the box. An image recorded from the camera is shown in Fig. 3.15.

The control box included power supply, stepping motor driver, controller PCB and a FPGA board (Spartan 3E). The controller PCB and programmed FPGA

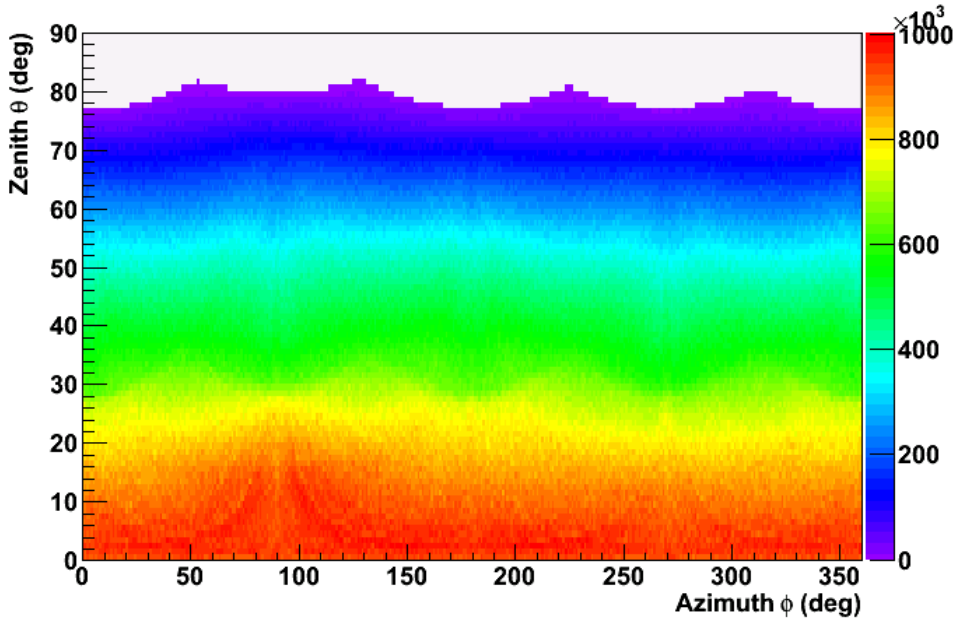

(a)

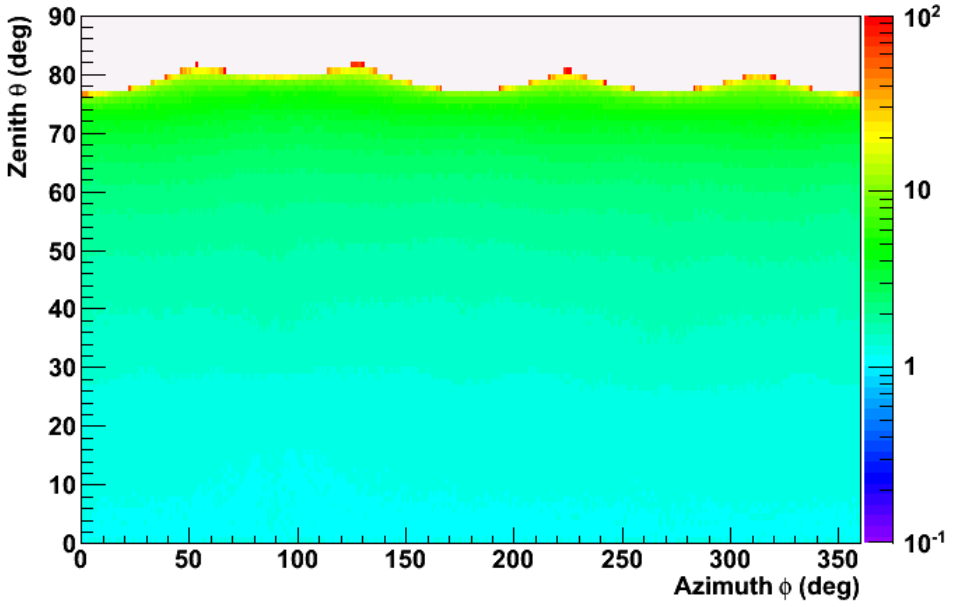

(b)

Figure 3.12: The angular response distributions for (a) 2-x 2-y triggering condition (unit: cm^2) and (b) its percentage error (unit: %). $\phi = 0°$ and 90° represents East and North respectively.

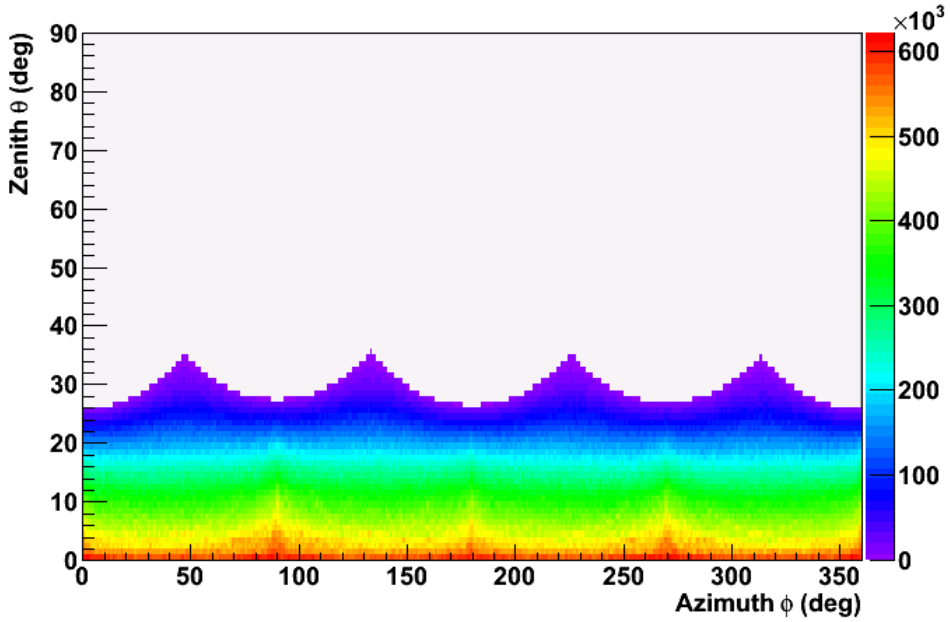

(a)

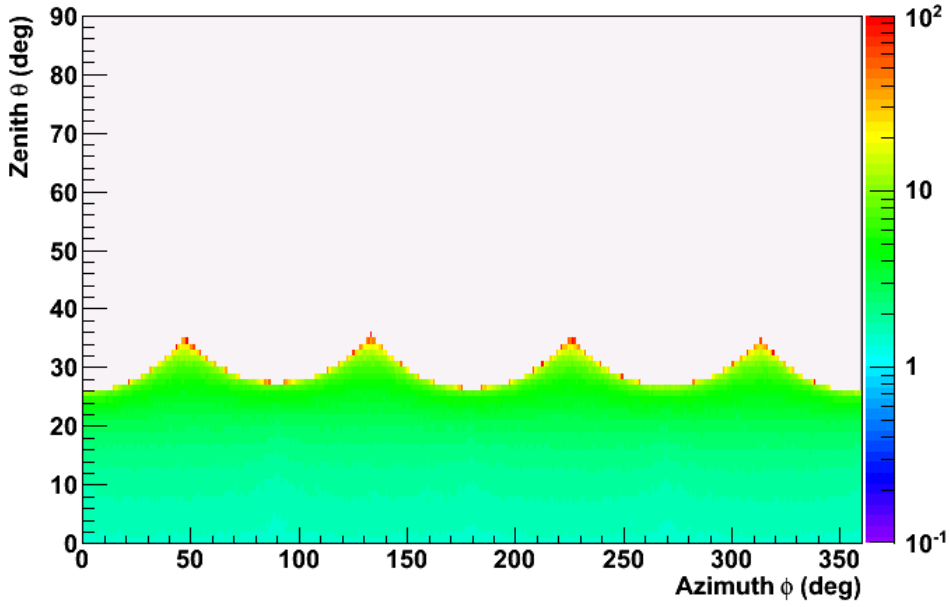

(b)

Figure 3.13: The angular response distributions for (a) 3x-3y triggering condition (unit: cm^2) and (b) its percentage error (unit: %). $\phi = 0°$ and 90° represents East and North respectively.

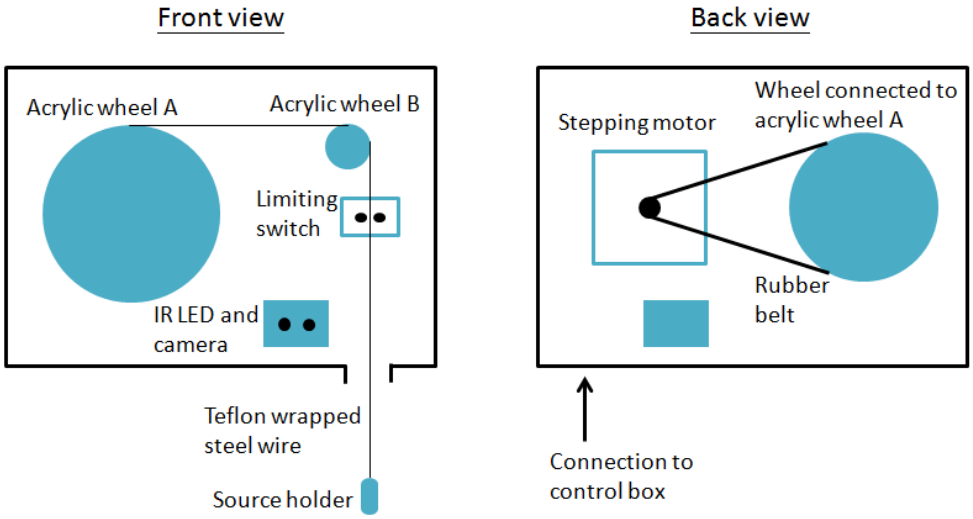

Figure 3.14: Schematic drawing of the calibration box.

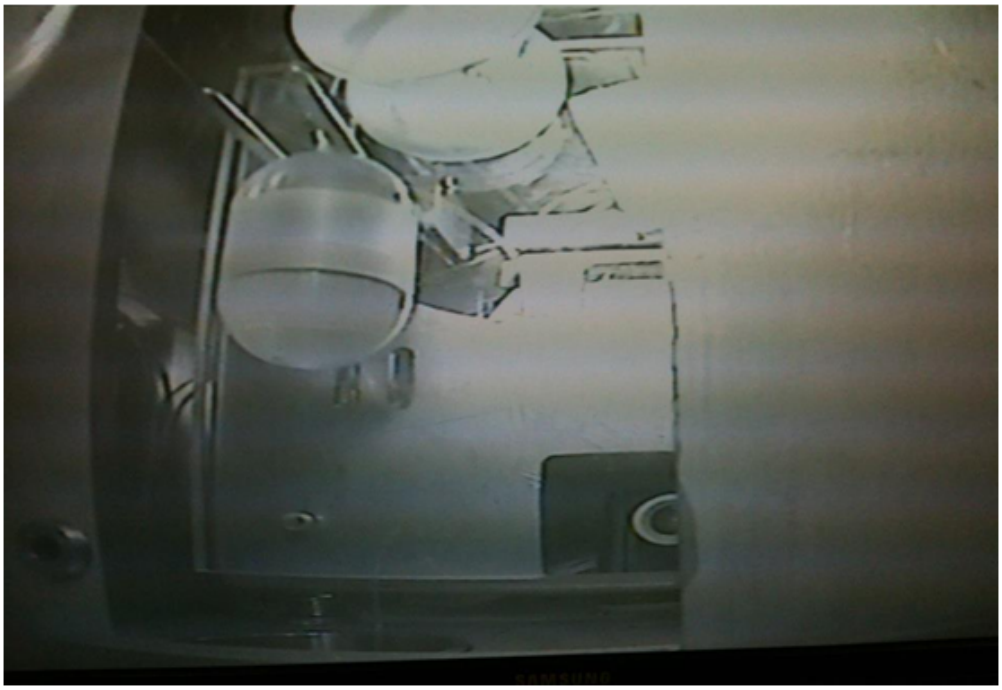

Figure 3.15: An image recorded by the IR camera inside the calibration box (the IR LED was on).

processed control of the motor, control of the IR LED and control of the LED pulser for calibration (not yet completed). Schematic of the controller PCB is shown in Fig. 3.16. For the motor control, the FPGA sent a number of pulses, which was the input step number, to the stepping motor driver. The numbers of steps for the motor to move needed for the source holder to be moved to the PMT ring positions were measured and used in MIDAS. The performance was tested in CUHK, and Table 3.2 shows the test result. 0 mm is the position corresponding to the ND PMT ring 1 and so on. The accuracy of the delivery was about 1 mm.

Table 3.2: The input and measured positions of the source holder.

Input position (mm)	Measured position (mm) Downward trip	Measured position (mm) Upward trip
0	0 ± 1	0 ± 1
209.2	209	210
313.8	315	314
418.4	419	419
627.6	629	629

Besides, a gas flow system was installed for the calibration box and connected through its gas inlet and outlet (not drawn on Fig. 3.14). It was used for gas purging (nitrogen) before and during calibration. Before a calibration, with the gate valve closed, the calibration box was purged with nitrogen at a large flow rate for a few minutes. After that, during the calibration, a smaller gas flow rate was used for purging the calibration box and the interior of ND tank. A schematic of the gas flow system is shown in Fig. 3.17. The pressure relief bubbler protected the system from high pressure of about 480 Pa, while the return bubbler provided a leaving path of the gas at about 15 Pa. For larger gas flow rate, Switch A and

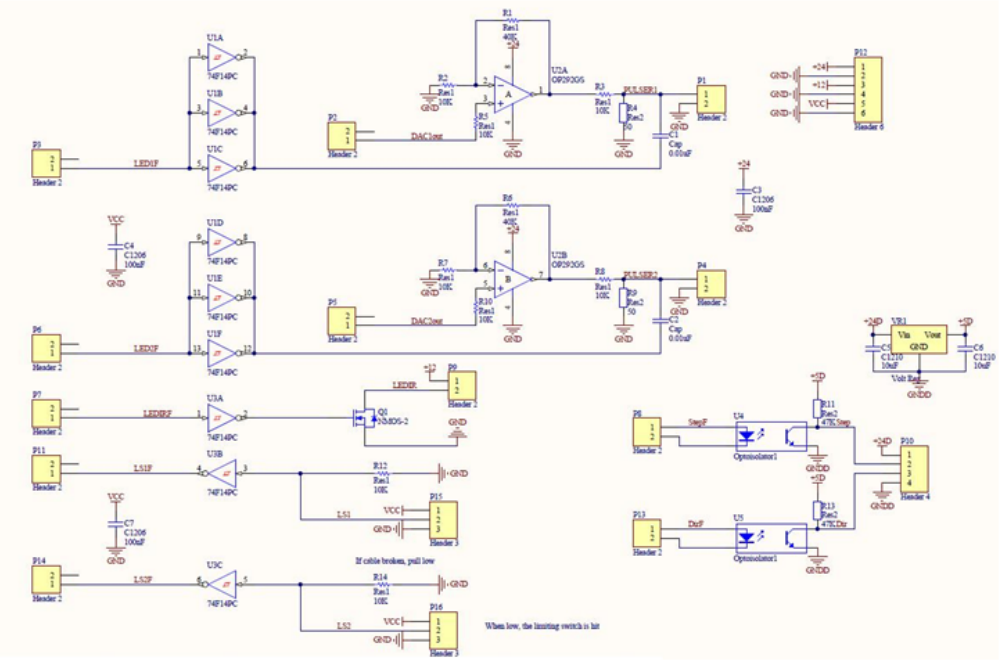

Figure 3.16: Schematic of the controller PCB for the control of the IR LED, LED pulser and motor.

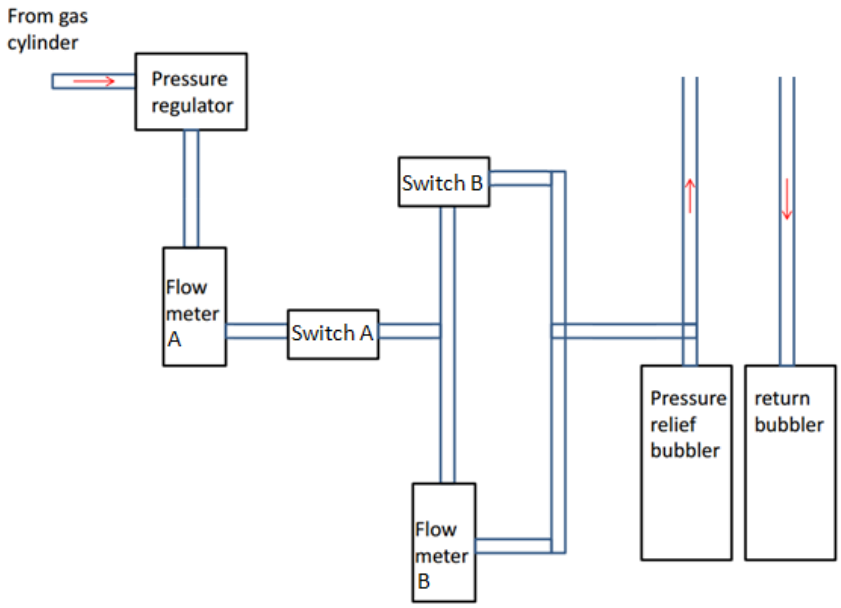

Figure 3.17: Schematic of the gas flow system for purging the ND.

Switch B were opened. The flow meter A reads the flow rate. For smaller gas flow rate, Switch A was opened but Switch B was closed. The flow meter B reads the flow rate.

Energy scale

Three radioactive sources were used for calibration, each having unique energy peaks of gamma emission. The ^{60}Co emits 2 gammas through the beta decay process:

$$^{60}\mathrm{Co} \longrightarrow ^{60}\mathrm{Ni} + e^{-} + \bar{\nu_e} + 2\gamma, \tag{3.3}$$

where the sum energy of the two gammas is 2.5 MeV, one 1.17 and the other 1.33 MeV. Fig. 3.18 shows the histograms of the sum of 16 analog to digital channels of the QDC, called ADCsum, with or without ^{60}Co deployed in the ND center. With the background subtraction, the net ADC spectrum from the source can

be obtained. Hence, by dividing the peak value of the ADCsum channel of the sum of the 2 gammas of 2.5 MeV, the energy scale (channel per MeV) can be obtained. Fig. 3.19. shows the calibrated reconstructed energy distribution of the ^{60}Co source. There is a peak of about 1.5 MeV due to events with either one of the gamma's escaped detection.

Since the energy scale depends on the PMT gains, which fluctuate a little bit with time, calibration of energy scale was done weekly [56]. The history of the energy scale is shown in Fig. 3.20 [57].

The ^{137}Cs emits a 0.667 MeV gamma through the beta decay process:

$$^{137}\mathrm{Cs} \longrightarrow^{137} \mathrm{Ba} + e^{-} + \bar{\nu_e} + \gamma. \tag{3.4}$$

The reconstructed energy distribution, based on the energy scale from ^{60}Co, with the ^{137}Cs deployed at the ND center is shown in Fig. 3.21. The peak was about 0.71 MeV which was greater than the expected value. Ngai reported that the peak would shift to lower energy if the trigger condition was reduced to 12 out of 16 [52]. This indicated that the lower energy part of the spectrum has lower trigger efficiency, due to the PMTs being closer to their thresholds. Therefore the measured peak would shift toward higher energy with the 16/16 trigger condition.

The AmBe emits neutrons through the following process:

$$^{9}\mathrm{Be} + \alpha \longrightarrow^{13} \mathrm{C}^{*} \longrightarrow^{12} \mathrm{C} + n + \gamma, \tag{3.5}$$

where the alpha particle is coming from the decay process of the Am, and the γ is from the relaxation of ^{13}C*. The gamma energy is 4.438 MeV and the neutron capture energy after thermalization [58] are 2.2 MeV (nH) or 8 MeV (nGd). Fig. 3.22 shows the reconstructed energy distribution, based on the energy scale from ^{60}Co, with the AmBe deployed at the ND center. Three peaks, 2.17 (nH), 5.42

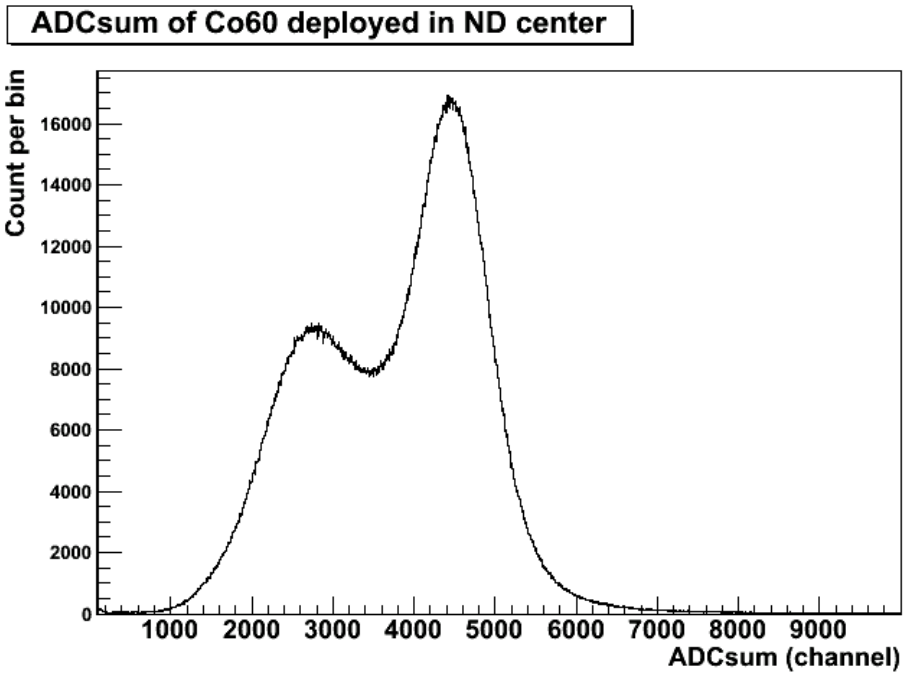

(a)

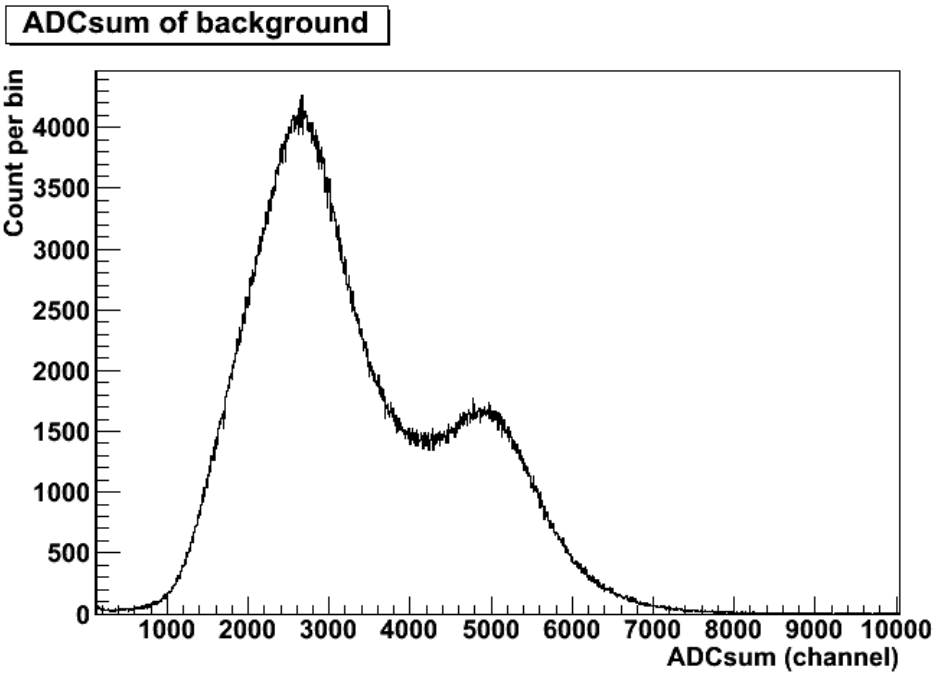

(b)

Figure 3.18: Histogram of ADCsum of 16 channels of QDC (a) with or (b) without ^{60}Co deployed in the ND center.

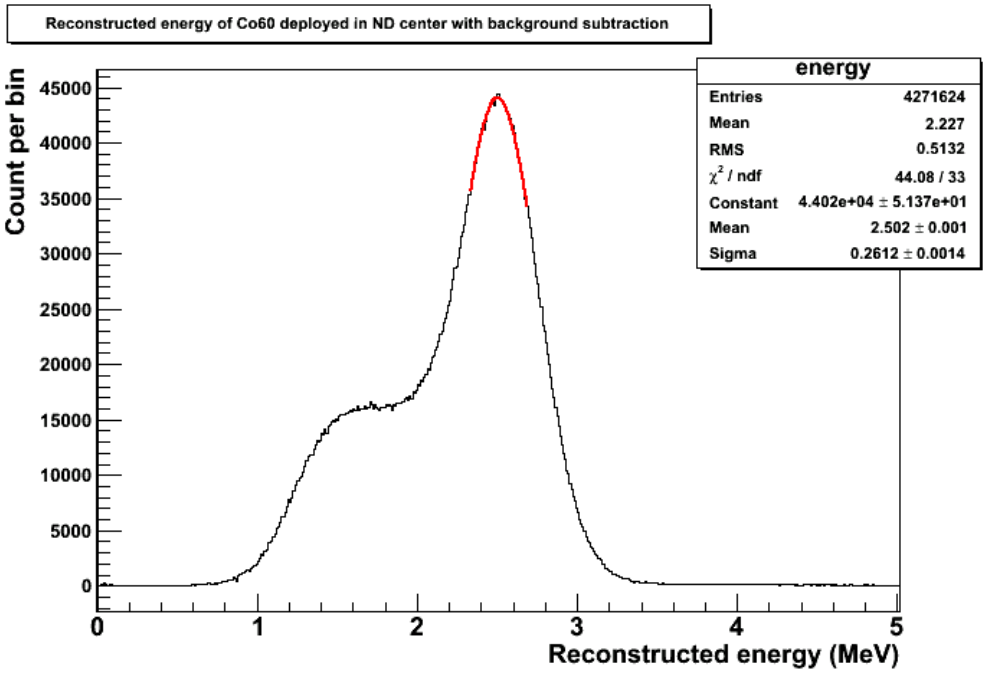

Figure 3.19: The reconstructed energy distribution for the ^{60}Co source deployed at the ND center. A Gaussian fitting, indicated as red, is applied near the peak of the sum of the two gammas' emission.

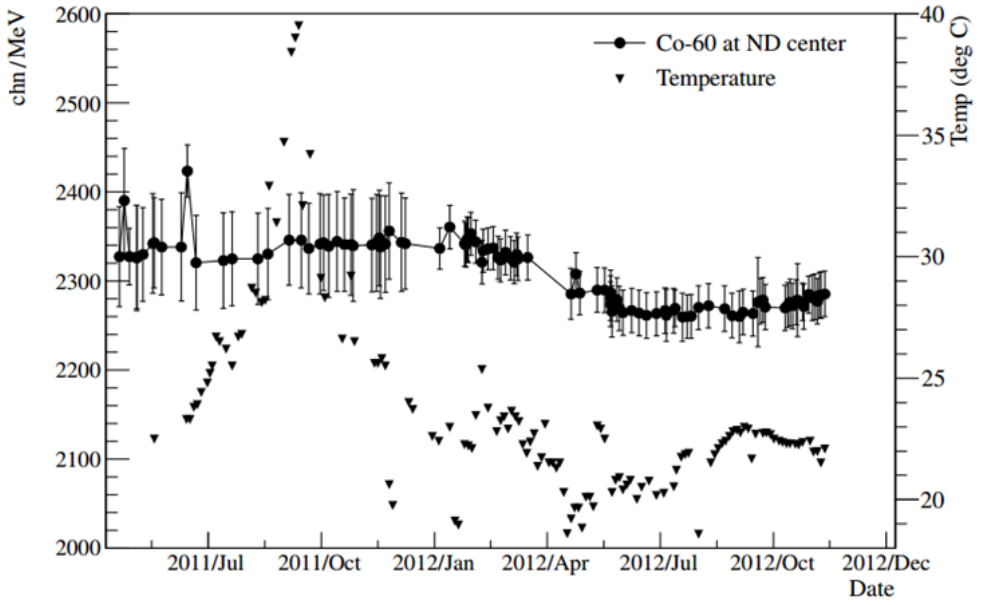

Figure 3.20: The calibration constants of the energy scale for the ND from the ^{60}Co source. The temperature of the laboratory is also shown as a reference. The rise in temperature during August was due to a failure of the air conditioning unit.

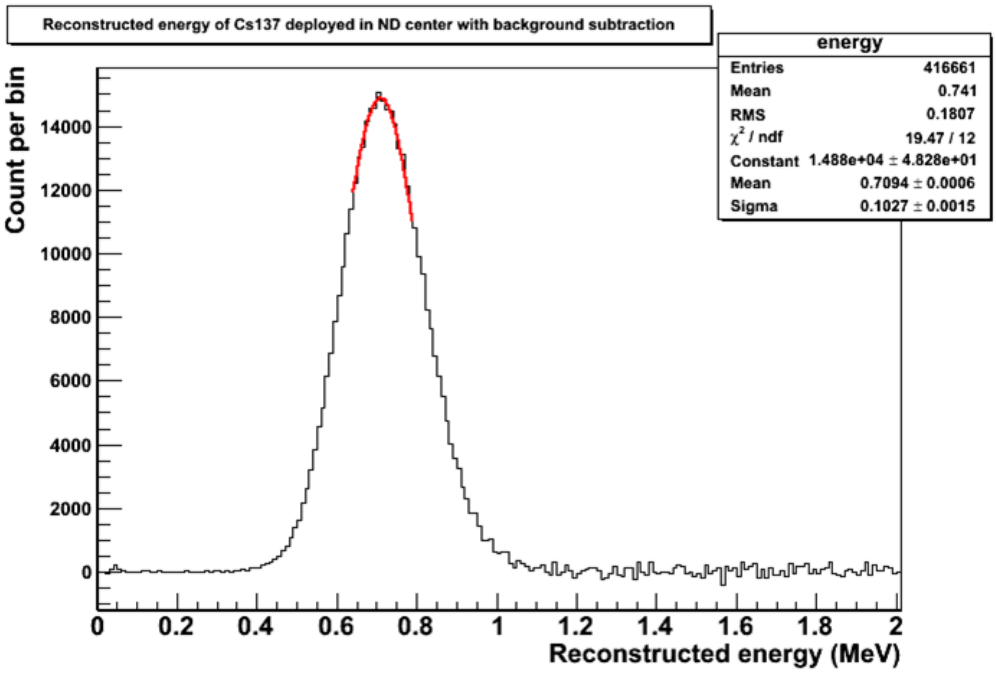

Figure 3.21: The reconstructed energy distribution for the ^{137}Cs source at the ND center. A Gaussian fitting, indicated as red, is applied near the peak of the gamma emission.

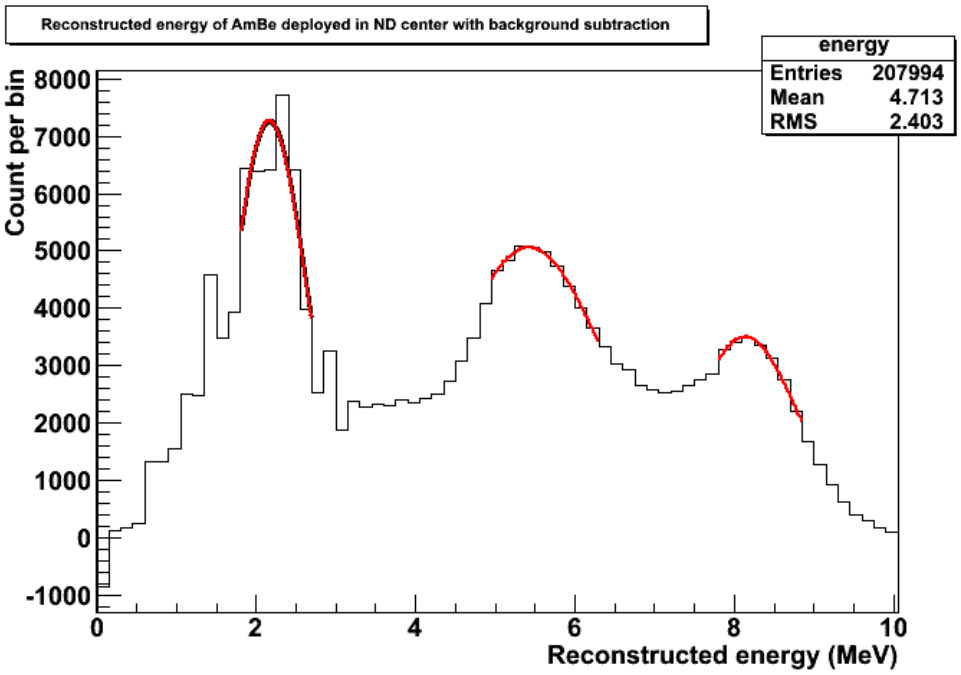

Figure 3.22: The reconstructed energy distribution of the AmBe events when it is deployed at the ND center. Gaussian fittings, indicated as red, are applied near the peaks. The fitted peaks are 2.17 (nH), 5.42 (γ) and 8.13 (nGd) MeV.

(γ) and 8.13 (nGd) MeV were obtained. The deviation of the 5.42 MeV peak from 4.44 MeV was due to the proton recoil with energy about 1 MeV during thermalization of the neutron [59]. For the neutron-Gd capture, the deviation in energy was accounted for by the non-linearity of the ADC scale.

A linear fitting of the energy expected, E_{truth}, against energy reconstructed, E_{rec}, of the peaks (nH and nGd of AmBe and ^{60}Co) gave:

$$E_{truth} = (0.975 \pm 0.004)E_{rec} + (0.07 \pm 0.02). \tag{3.6}$$

The deviation of the data from the ideal slope of 1 was about -2.6 %.

3.5 Event reconstruction

The events triggering the muon tracker or the neutron detector were reconstructed. After the reconstruction, for the case of the muon tracker, incidence angles and points of interception are known. The total energy and vertex are known for each event of the neutron detector.

3.5.1 Muon Tracker

The tracks have to be reconstructed from the hit patterns of the hodoscopes. Unlike the structure of the muon telescope, there are 6 layers of hodoscopes with 3 in x and 3 in y directions. The available triggering conditions are "2-x and 2-y" and "3-x and 3-y".

The reconstruction algorithm was worked out by Tsang [60] and Ngai [52]. The reconstruction is first applied to the x-z and y-z plane separately. For each plane, linear track fittings are applied to the combinations, which are selections of clusters for the fitting. Each layer has only one cluster, having one or more consecutive hit hodoscopes. If the hit hodoscopes are not consecutive, which can be due to showers of secondary particles or noise, the "Fitness" parameter, which will be discussed soon, would be 0. Totally, there are 4 combinations for 3 clusters in the 3-fold triggering and at least 2 combinations for 2 clusters in the 2-fold triggering. In each combination, there are 10 tracks of candidates. The candidates are fitted from linear regression of random sampled points in the clusters. Therefore, there are 40 track candidates in the 3-fold triggering and at least 20 track candidates in the 2-fold triggering. Finally, the candidate with the greatest "Fitness" parameter is chosen. The "Fitness" parameter represents how good a hit pattern matches

with a track. The "Fitness" F is defined as [60]:

$$F = \prod_{i=1}^{N} P(A_i, E_i), \tag{3.7}$$

where N is the total number of hodoscopes, A_i and E_i (= 0 or 1) are the actual and expected hits, from the given track, of the i^{th} hodoscope. P is defined as [60]:

$$P(A_i, E_i) = \begin{cases} P_{E,i} & \text{if } A_i = 1 \text{ and } E_i = 1 \\ 1 - P_{E,i} & \text{if } A_i = 0 \text{ and } E_i = 1 \\ 1 - P_{N,i} & \text{if } A_i = 0 \text{ and } E_i = 0 \\ P_{N,i} & \text{if } A_i = 1 \text{ and } E_i = 0 \end{cases}, \tag{3.8}$$

where $P_{E,i}$ is the efficiency of the i^{th} hodoscope and $P_{N,i}$ is the probability of hit by chance coincidence from noise, which is approximated from the hodoscope singles rate (typically about 1kHz) $\times$ the trigger time window of 100 ns. Details of the reconstruction performance was discussed by Ngai [52]. Finally, the combination of the two-best fitted tracks from each of the plane give a three dimensional track.

3.5.2 Neutron detector

The reconstruction of visible energy and vertex is achieved by the maximum likelihood of 16 Poisson functions of PMT measured and calculated photon numbers N_m and N_c respectively, based on the source vertex and energy. The N_c received by the i^{th} PMT is calculated by:

$$N_{ci} = f(\theta_i)\epsilon\eta_Y E \frac{A_{cathode}}{|\overrightarrow{r}_{PMT_i} - \overrightarrow{r}_{source_i}|^2} e^{-\frac{|\vec{r}_{PMT_i} - \vec{r}_{source_i}|}{\lambda_\circ}} + \sum_{j=1}^{k} R^j N_{reflect_{1,j}} + \sum_{j=1}^{k} R^j N_{reflect_{2,j}}, \tag{3.9}$$

where ϵ is the PMT efficiency, η_Y is the light yield of the liquid scintillator, E is the total energy emitted from the source, $A_{cathode}$ is the area of photocathode, $|\overrightarrow{r}_{PMT_i} - \overrightarrow{r}_{PMT_i}|$ is the distance between the PMT_i and the source, $\lambda_\circ$ is the attenuation length of the liquid, and $f(\theta)$ is the angular response function of the PMT for the photon incident angle θ [61]:

$$f(\theta_i) = 0.378 + 0.5099\cos(\theta) + 0.1131\cos^2(\theta), \tag{3.10}$$

where θ is the angle between incident photon and PMT longitudinal axis and the function for the 8" PMTs of the Daya Bay Experiment has been adopted. $N_{reflect_1}$ and $N_{reflect_2}$ are the photon numbers received from reflections of the specular reflectors with reflectivity R, for photons first hitting top and bottom reflectors respectively. The functional form of $N_{reflect}$ is the same as the first part of Eq. 3.9 with $\overrightarrow{r}_{source_i}$ and θ_i for the corresponding image positions of the source, which depend on the number of reflections j. The maximum number of reflections k is 5 or a value such that the line joining the image of source and the PMT didn't intercept the reflector.

The initial guessing of E and $\overrightarrow{r}_{source_i}$ makes use of the charge center method. These two parameters are then iterated to maximize the likelihood until convergence. Details of the reconstruction performance were discussed in Ref. [52].

3.6 Muon flux measurement and results

Unlike the CUHK muon telescope, the muon tracker can't be freely rotated to point at different directions for data taking. The flux measurement was made under the configuration shown in Fig. 3.3 with triggering condition 2x and 2y. Time averaged and time dependent muon fluxes were studied from the same set of data. Events with Fitness larger than zero were used for the time averaged case,

while no Fitness selection criterion was applied for the time dependent case.

3.6.1 Time averaged CR variations

The angular flux distribution depends on the overburden distribution and zenith angle dependence of the surface muon flux. Using the mountain profile shown in Fig. 3.23(a), the angular distribution of the overburden was calculated. The calculation algorithm is by summing the thickness of rock along a line in the direction of θ and ϕ starting from the laboratory. Along the line, the summation is done only when the z-coordinates of the line are smaller than the interpolated z-coordinates of the mountain profile. By scanning all values of θ and ϕ, the angular distribution of the overburdens viewing from the laboratory was obtained. The error of the overburden of a bin was estimated by finding the standard deviation of the overburdens within that bin during the scan. Besides, in order to test whether the profile map size is large enough, the leaving x-y coordinates, where the line does not intercept the profile anymore, were recorded. The results are shown in Fig. 3.23(b) and 3.24. Fig. 3.23(b) shows that the leaving points touch the boundary of the map at $\theta = 80°$, but not 70°. Therefore, the map is sufficiently large for studying the flux for $\theta < 70°$. In Fig. 3.24(a)., there are overburdens more than 600 m around $\phi = 150°$ and 320° with $\theta = 60°$ - 70°. This is because of the appearance of Mount Cameron and Nicholson.

The angular muon count distribution was measured for about a year. Division of the angular counts by the angular responses, shown in Fig. 3.12(a), gave the angular flux. The result and its percentage error, which was propagated from its statistics and the uncertainties of the angular responses, are shown in Fig. 3.25. There was asymmetry of the flux in ϕ, which was due to the appearance of the two mountains. In addition, simulation of muon flux reaching the laboratory was worked out by Luk using the "Muon Simulation Code", MUSIC [49]. The

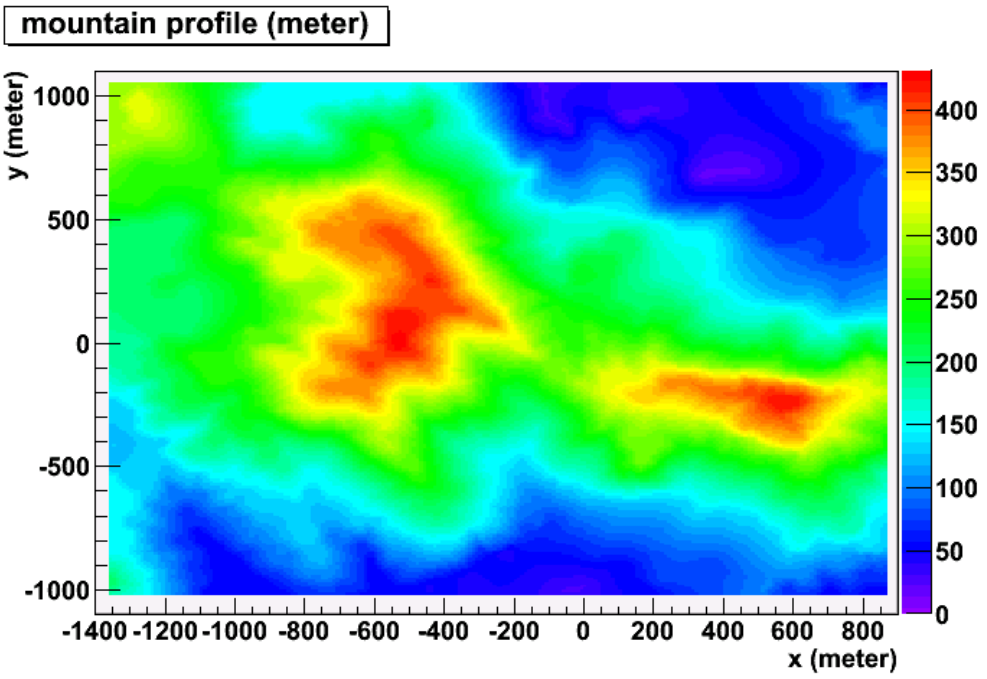

(a)

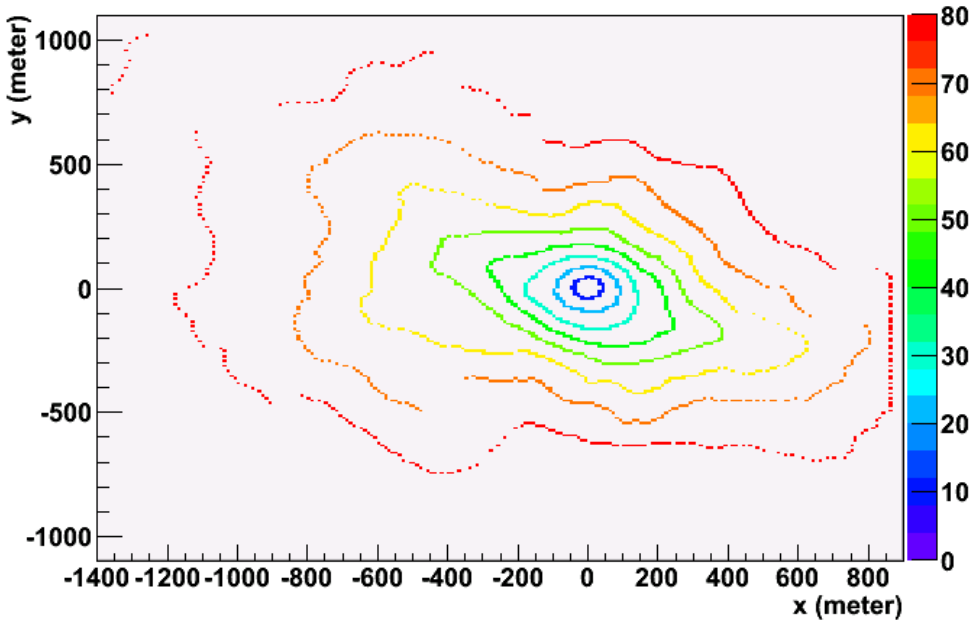

(b)

Figure 3.23: (a) Mountain profile in contour plot. Positive x and y are toward east and north respectively. (b) Boundary of the lines leaving the profile. The z-axis is the zenith angle of the leaving point, represented by the color codes, in steps of 10 degrees. The boundary of 80° touches the boundary of the map.

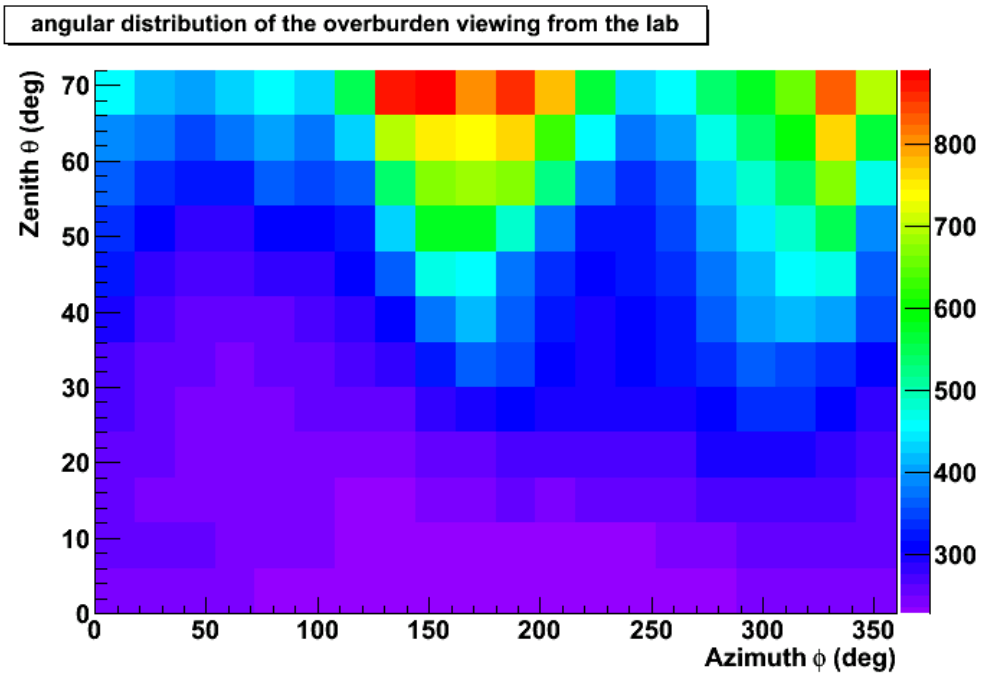

(a)

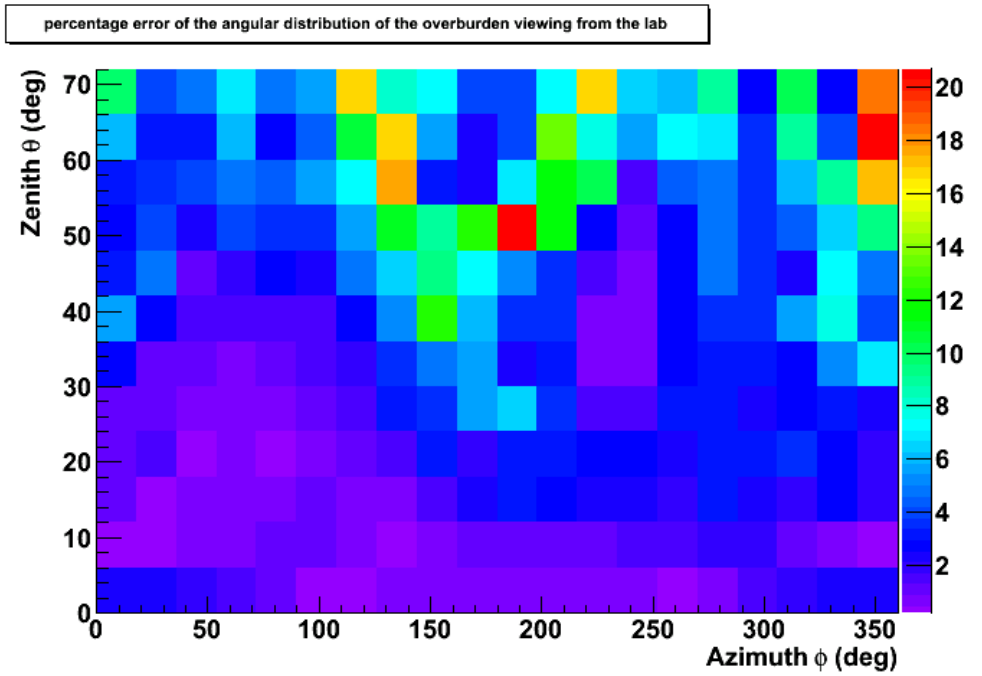

(b)

Figure 3.24: (a) Angular distribution of the overburdens (unit: m) viewing from the laboratory. (b) Percentage error of the angular distribution of the overburdens viewing from the laboratory. $\phi = 0°$ and $90°$ represent East and North respectively.

simulation was started with generation of muons on surface with flux and energy according to the modified Gaisser formula. The overburden distribution with standard rock density of 2.5 gcm^{-3} was input for the propagation of muons in rock. The tracker was triggered by these simulated muons, and the reconstructed distribution is shown in Fig. 3.26. For a more quantitative comparison, the bin-by-bin ratio of the measurement to the simulation was plotted and shown in Fig. 3.27. Most of the entries are close to 1, showing good agreement, except for the entries for $\theta \approx 60°$. Those entries correspond to the direction of pointing towards the mountains. The disagreement may be due to insufficient resolution of the map or the errors in the density of rock. Fig. 3.28 shows the averaged fluxes, of three ranges of $\theta(0° - 24°, 24° - 48°, 48° - 72°)$ against ϕ.

3.6.2 Time dependent CR variations

The hourly time series and monthly averaged counts during the same period of data taking of the CUHK muon telescope is shown in Fig. 3.29. In Fig.3.29(a), the discontinuities were due to a system crash. The count rate was quite stable over the time, as compared to the results of the CUHK muon telescope. The difference may be due to the fact that only high energy muons on the surface are measured in the underground laboratory, since the high energy muons are much less affected by the atmosphere.

The day-night variation in the count rates was also studied. The averaged count rate over a year according to the local time is shown in Fig. 3.30. In the plot, the uncertainty was statistical only, over a year of counts. On average, the day counts were higher than the night counts with variations of about 1% from the mean. This was much smaller than the variations accounted for by atmospheric change measured on surface. Besides, there was a small peak around 14 o'clock local time with amplitude of about 0.6%.

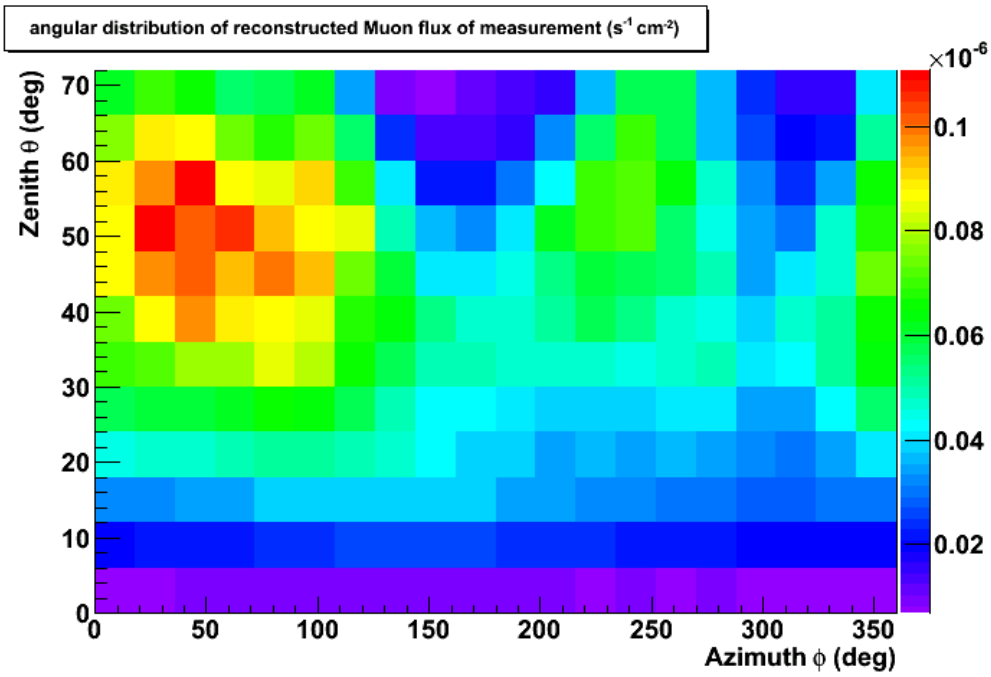

(a)

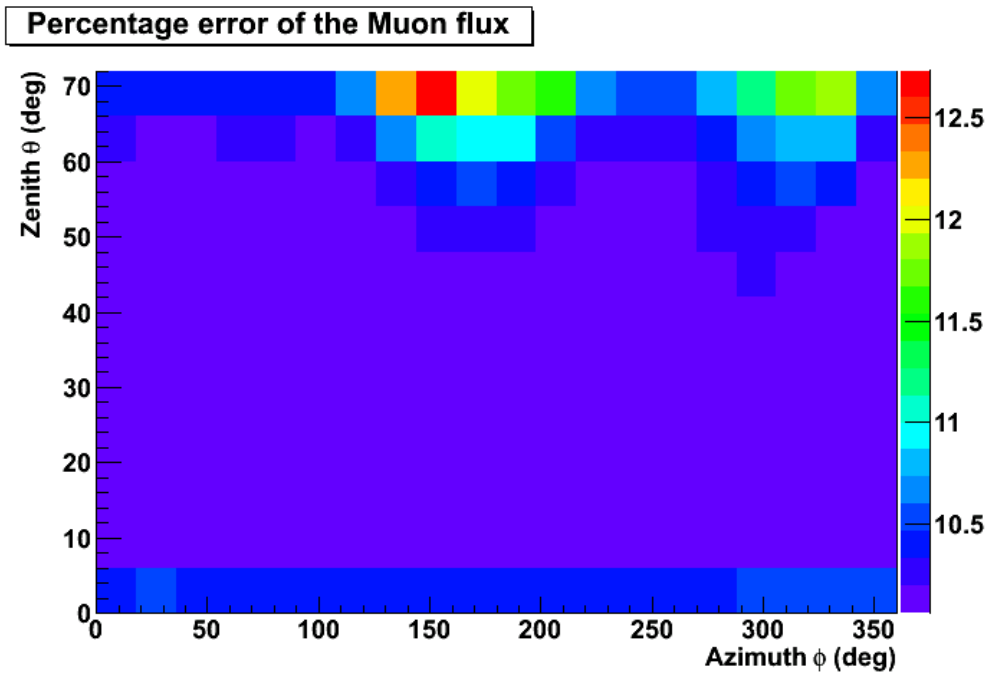

(b)

Figure 3.25: (a) Angular distribution of the reconstructed muon flux from measurement. b) Percentage error of the muon flux. $\phi = 0°$ and $90°$ represent East and North respectively.

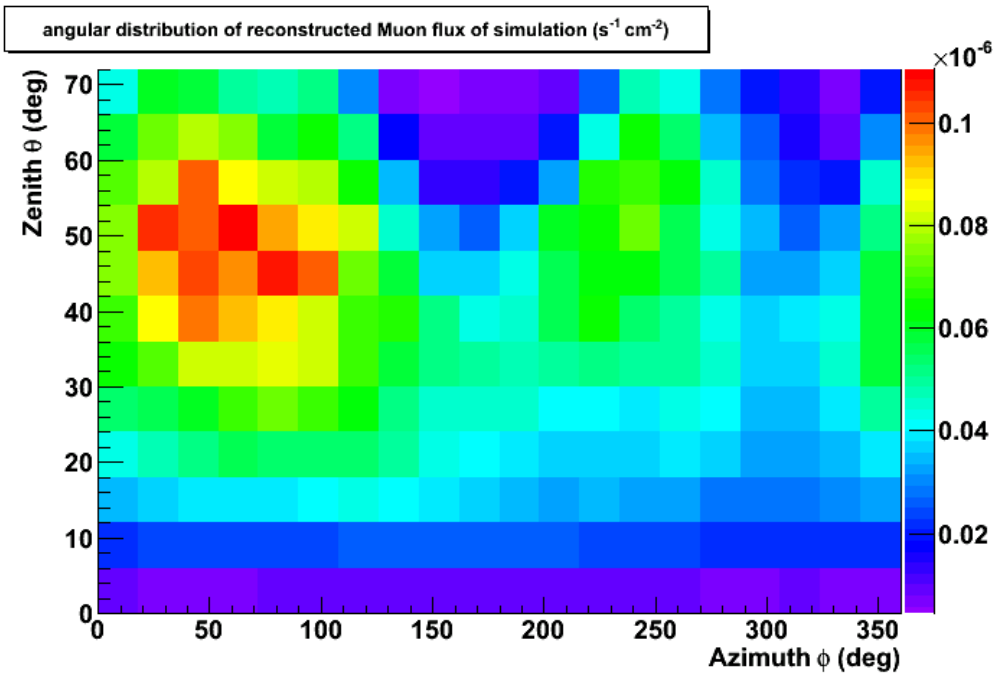

Figure 3.26: Angular distribution of the reconstructed simulated muon flux entering the Aberdeen Tunnel Laboratory.

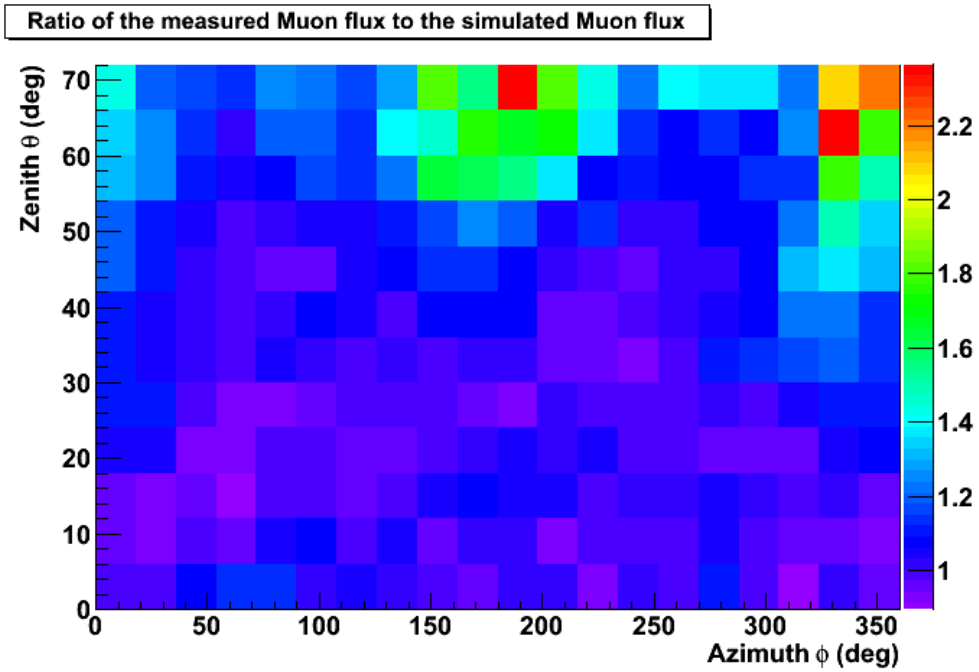

Figure 3.27: Ratio of the measured to simulated muon flux detected by the Aberdeen Tunnel muon tracker.

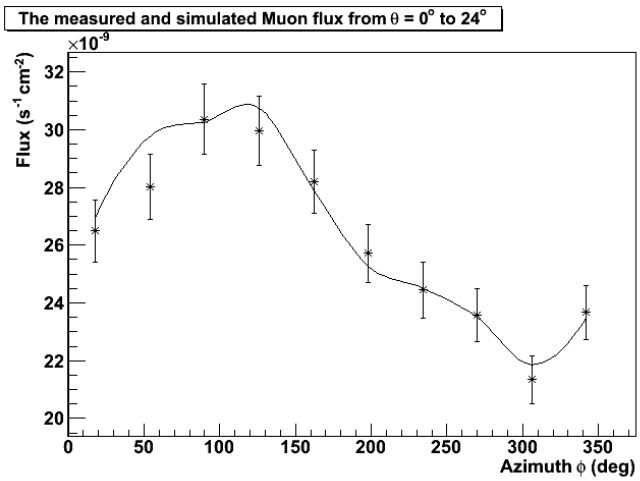

(a)

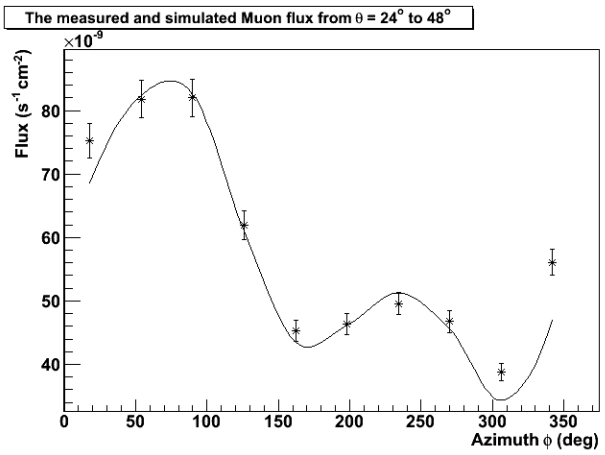

(b)

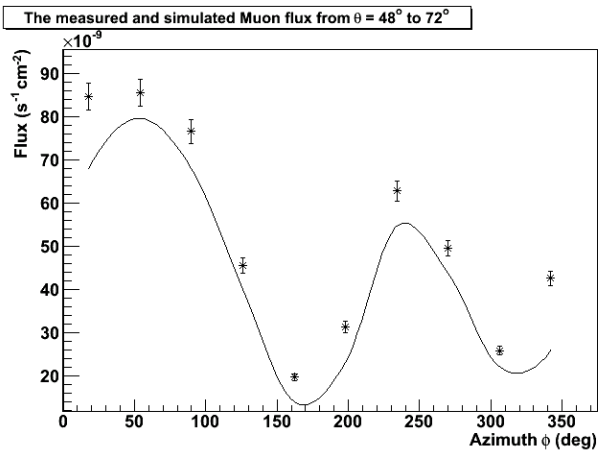

(c)

Figure 3.28: The averaged fluxes against ϕ, for (a) θ from $0° - 24°$, (b) θ from $24° - 48°$, and (c) θ from $48° - 72°$. Crosses: measurement, line: simulation.

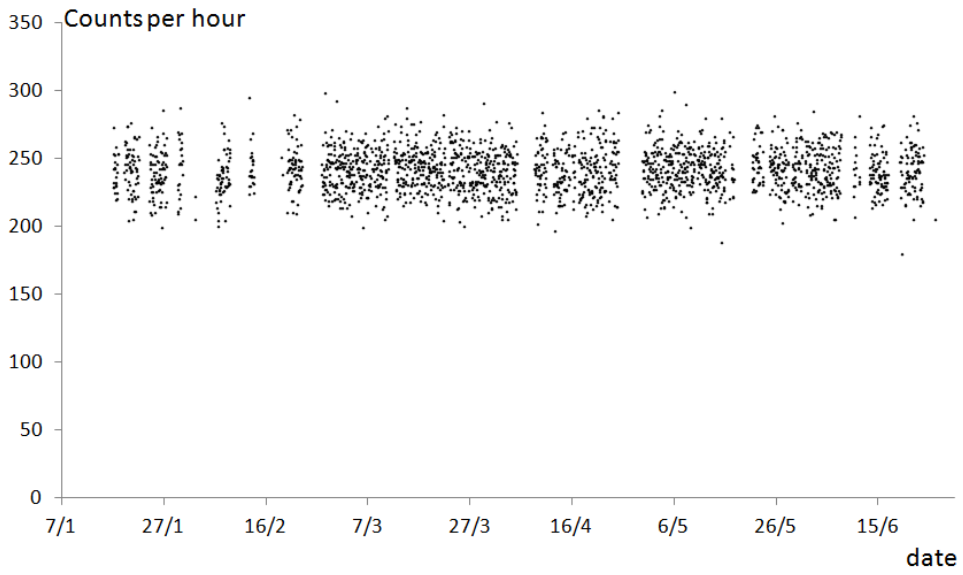

(a)

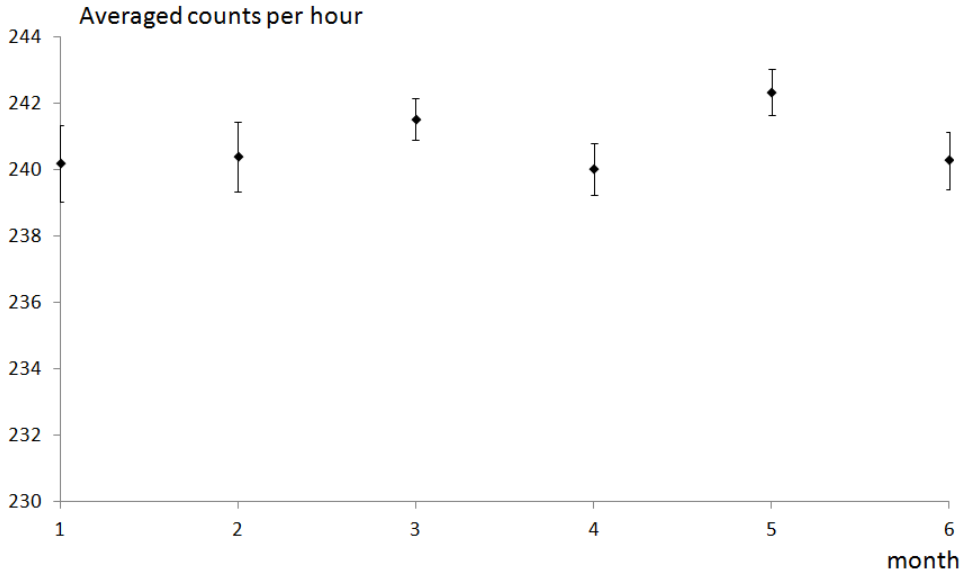

(b)

Figure 3.29: (a) Time series of the muon counts per hour in 2012, measured using the Aberdeen Tunnel muon tracker. (b) Monthly averaged muon counts per hour in 2012, measured using the Aberdeen Tunnel muon tracker.

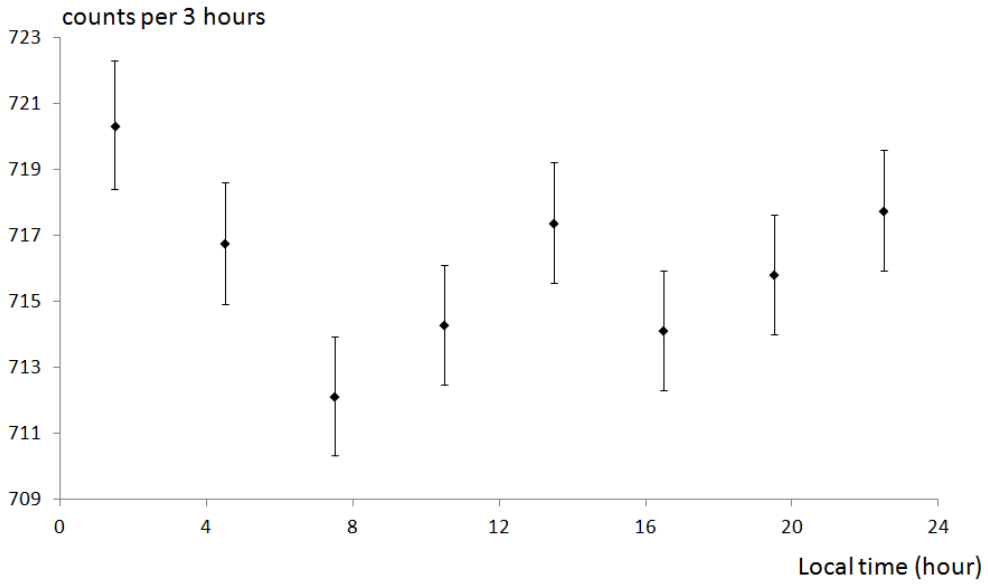

Figure 3.30: 24-hour series of the muon tracker counts, averaged from the entire time series in 2012, measured by the Aberdeen Tunnel muon tracker.

3.7 Muon induced neutron measurement and results

The data taking for the muon induced neutrons was carried out together with the muon measurement. The triggering condition for the neutron detector is NHIT 16 out of 16. Data for 2012 with accumulated run time of about 175 days was analyzed.

3.7.1 Event selection and systematic uncertainty

A reconstructed track intercepting the top and bottom surface of the acrylic vessel (AV) acted as a prompt signal for the muon induced neutrons. Fig. 3.31(a) and 3.31(b) show the number of ND triggers against reconstructed energy and time after the prompt muons. In Fig. 3.31(a), there were much more ND triggers with

energy above 4 MeV just after the prompt muons. Those were mainly the signals of the Gd capture of the muon induced neutrons. The background, such as fast neutrons or electronic noise, contributed a lot in the triggers shown in both Fig. 3.31. Therefore, it was necessary to eliminate the background. The life time of Gd-capture of the muon induced neutrons was about several tens of μs. Hence, the time of 1000 μs after the prompt muon was chosen for the background estimation.

An event within an appropriate reconstructed energy range, near the nGd capture of 8 MeV energy, and appropriate time after the prompt muon trigger, was considered as a neutron candidate N. For the background estimation N_{bkg}, events happening within the same reconstructed energy range and time range after 1000 μs of the prompts were considered. Selection of the ranges was based on the minimum of the total uncertainty ratio, defined as:

$$\begin{aligned} &\text{total uncertianty ratio} \\ &= \frac{\sqrt{\text{statisical uncertainty}^2 + \text{systematic uncertainty}^2}}{N - N_{bkg}} \\ &= \frac{\sqrt{N + N_{bkg} + [(N - N_{bkg})E_{sys}]^2}}{N - N_{bkg}}, \end{aligned} \tag{3.11}$$

where E_{sys} is the percentage of systematic uncertainty. The systematic uncertainties were due to the reconstructed energy cut, time cut, energy scale in the measurement, and the neutron detection efficiency in simulation. Table 3.3 summarized the systematic uncertainties. The uncertainty of the reconstructed energy cut arises from the deviation of the slope of 1 in the linear fit of energy scale from the calibrations in Eq. 3.6. The uncertainty of the time cut was contributed from the timing uncertainty [52], and the uncertainty of the energy scale was the size of its fluctuations [48]. There were differences in the energy scale for the simulation to match the various peaks from the calibration sources [62] in the measurement. The uncertainty of the neutron detection efficiency can be estimated from the

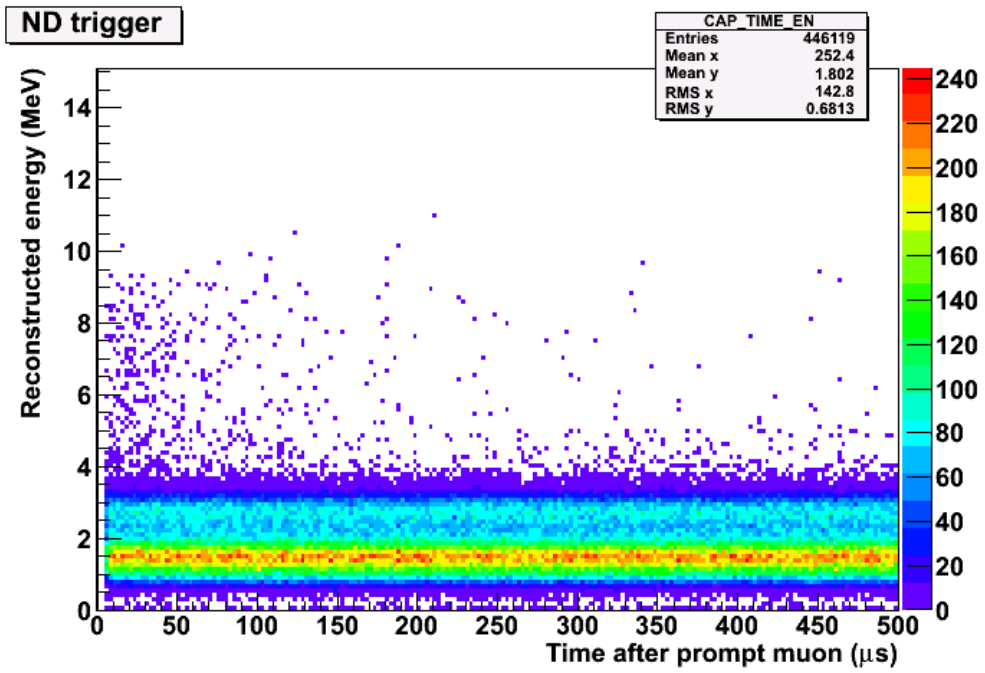

(a)

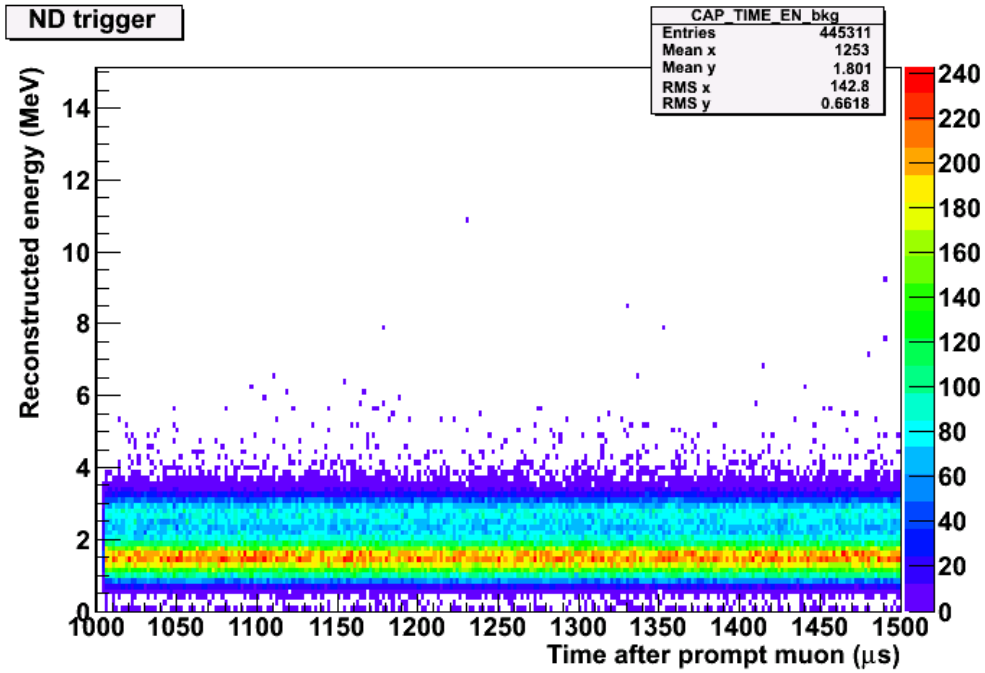

(b)

Figure 3.31: Number of ND triggers against reconstructed energy and time after the prompt trigger of the muon tracker. (a) Neutron candidate counting. (b) Background counting.

different efficiencies in the simulation using different energy scales.

Table 3.3: Summary of the systematic uncertainties in muon induced neutron measurement.

Contributions to systematics	uncertainties
reconstructed energy cut	2.6%
time cut	0.4%
energy scale	2%
neutron detection efficiency	5%
Total systematic uncertainty	6%

The dependence of the total uncertainty ratio on the energy range and time window were obtained by scanning over the lower limit of the energy range $E_\circ$ and upper limit of the time window $T_\circ$ respectively, where the energy range was from $E_\circ$ to 30 MeV and the time window was from the dead time of QDC, 5.7 μs, to $T_\circ$. The result is shown in Fig. 3.32. From the figure, $E_\circ = 4.5$ MeV and $T_\circ = 150$ μs were chosen. The total uncertainty ratio under this configuration was 0.087 or 8.7%.

3.7.2 Neutron detection and DAQ efficiency

Chan has simulated the muon induced neutrons under the detector configuration in NUWA [62]. In the simulation, the total number of muon induced neutrons generated in the GdLS region was 35106. Under the selected energy cut, using mean value of the energy scales, and time window for the reconstructed events, the number of passed events was 10412, which included the effects of spill in and spill out. As a result, the neutron detection efficiency was 10412/35106, or 29.7%.

Besides the simulation, the QDC dead time and number of lost events were

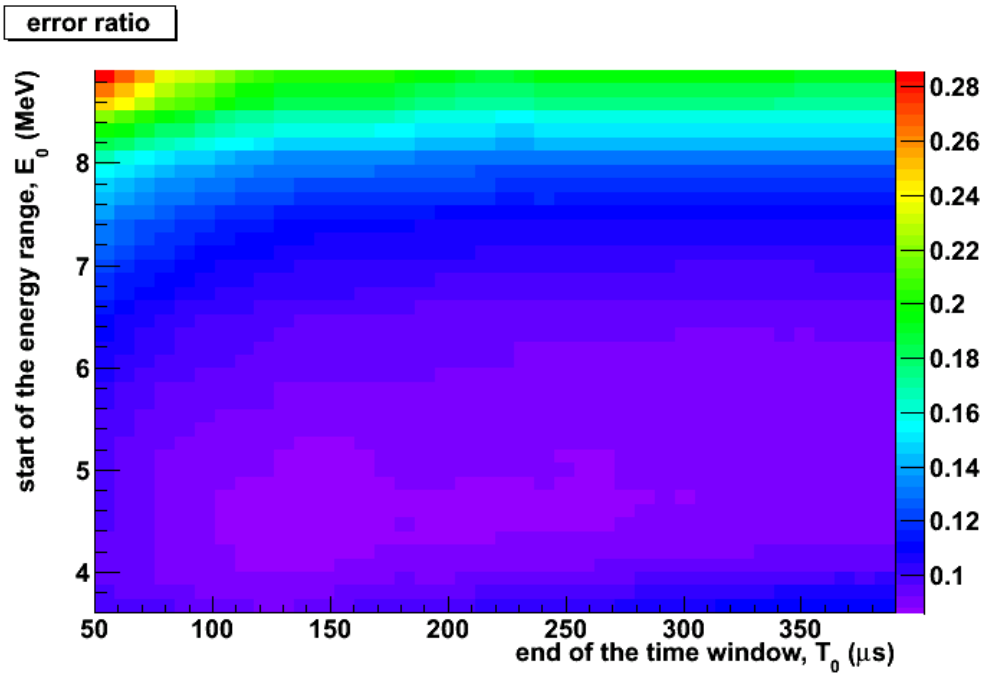

(a)

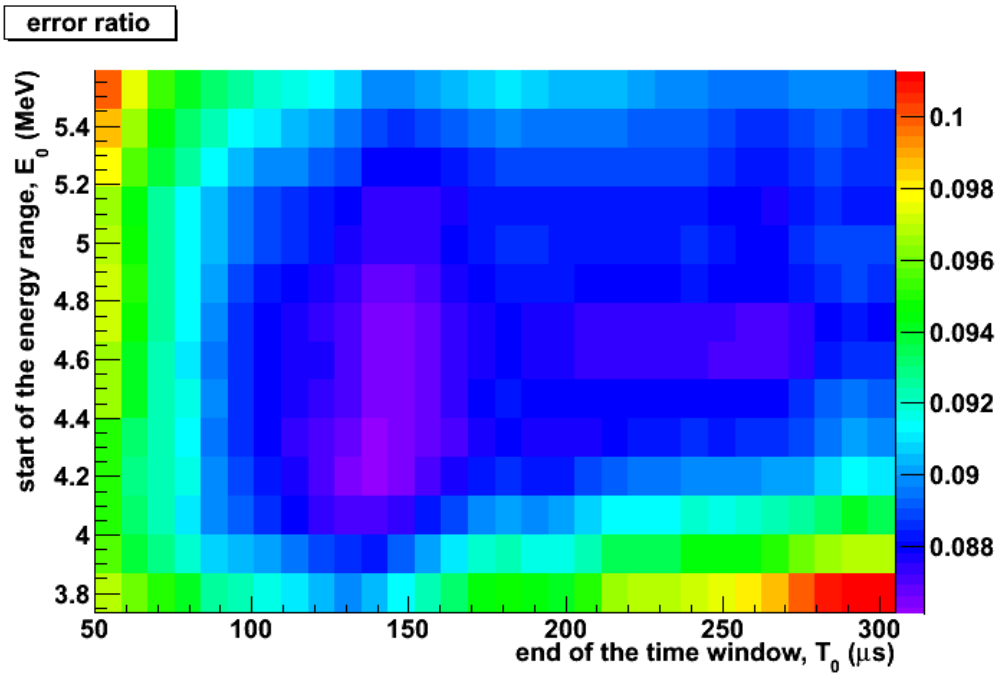

(b)

Figure 3.32: Dependence of the total uncertainty ratio on the energy range, $E_\circ$ to 30 MeV, and the time window, 5.7 μs to $T_\circ$ for the delayed signal and 1005.7 μs to 1000+$T_\circ$ for background. (a) Plot in a large scale size. (b) Zoomed in plot near the region of the uncertainty ratio minimum.

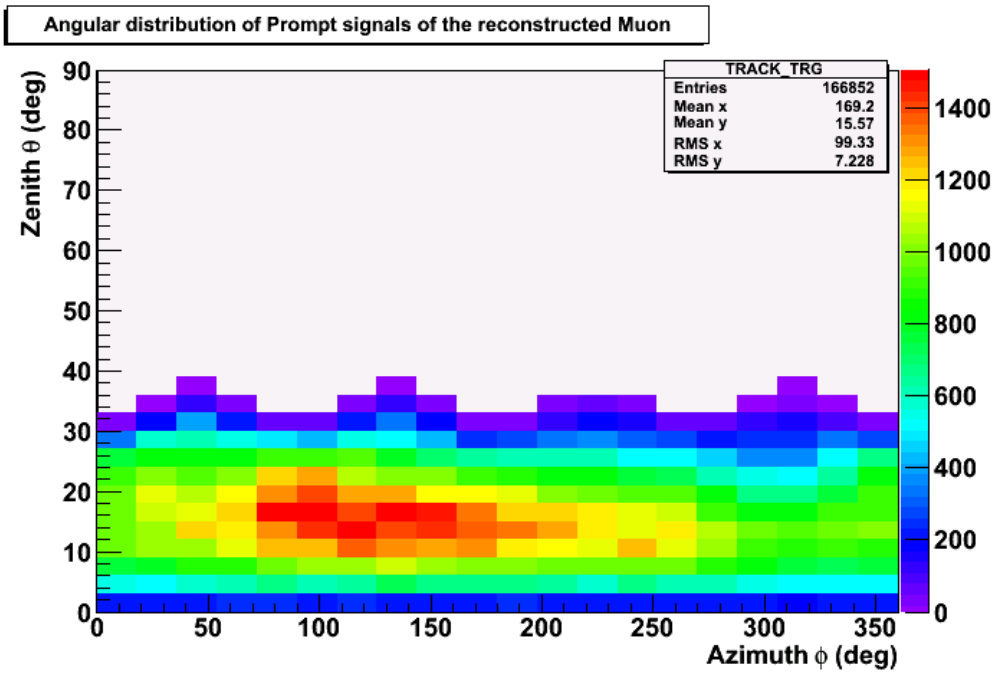

Figure 3.33: Angular distribution of the prompt signals.

reported by Cui [63]. These contributed to the DAQ trigger inefficiency of about 5%.

3.7.3 Results and discussion

The total number of analyzed prompt signals was 166852. The angular distribution of the prompt signals is shown in Fig. 3.33. Since only the muons intercepting top and bottom surface of the AV were considered as prompt signals, the angular distribution was just up to θ around 30°. For those muons, the track length inside the GdLS was calculated using the track information and shown in Fig. 3.34. The total muon track length was 166852×83.8 cm, or $(140 \pm 0.3)\times10^5$ cm.

The distributions of the time and energy of the ND triggers after the prompt signals were shown in Fig. 3.31(a) and 3.31(b) before. The distribution of neutron capture time with reconstructed energy $>$ 5.3 MeV was shown in Fig. 3.35. A

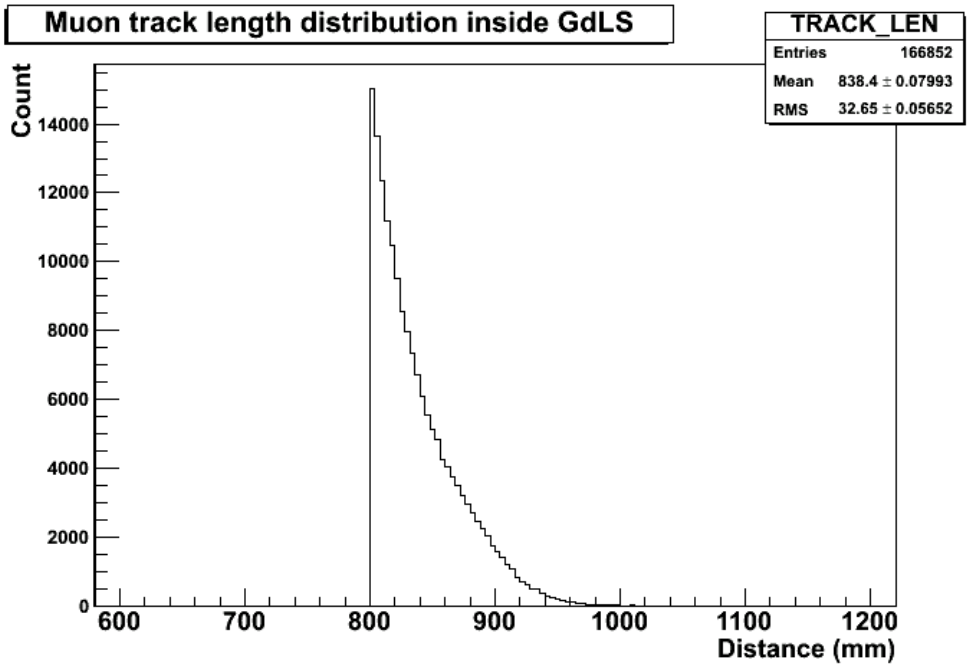

Figure 3.34: Muon track length distribution inside the GdLS.

function $f(t)$ was used to fit the distribution. It was defined as:

$$f(t) = p0e^{p1t} + p2, \tag{3.12}$$

where $p0$, $p1$ and $p2$ are the fitting parameters. The best fit result for $p1$ was -0.01935 $\pm$ 0.00199, corresponding to the capture time constant of (51.7 $\pm$ 6.0) μs. This agreed with the capture time from simulation of (52.8 $\pm$ 1.4) μs.

The neutron candidates within the energy range, 4.5-30 MeV, and the time windows, after prompt, 5.7-150 μs (delayed signal) and 1005.7 – 1150 μs (background) were counted. The total number of neutron candidates in the delayed and background time windows were 343 and 36 respectively. Therefore, the number of neutrons with background subtracted was 307. The number of neutrons generated in GdLS was 307/(DAQ trigger efficiency $\times$ neutron detection efficiency) =

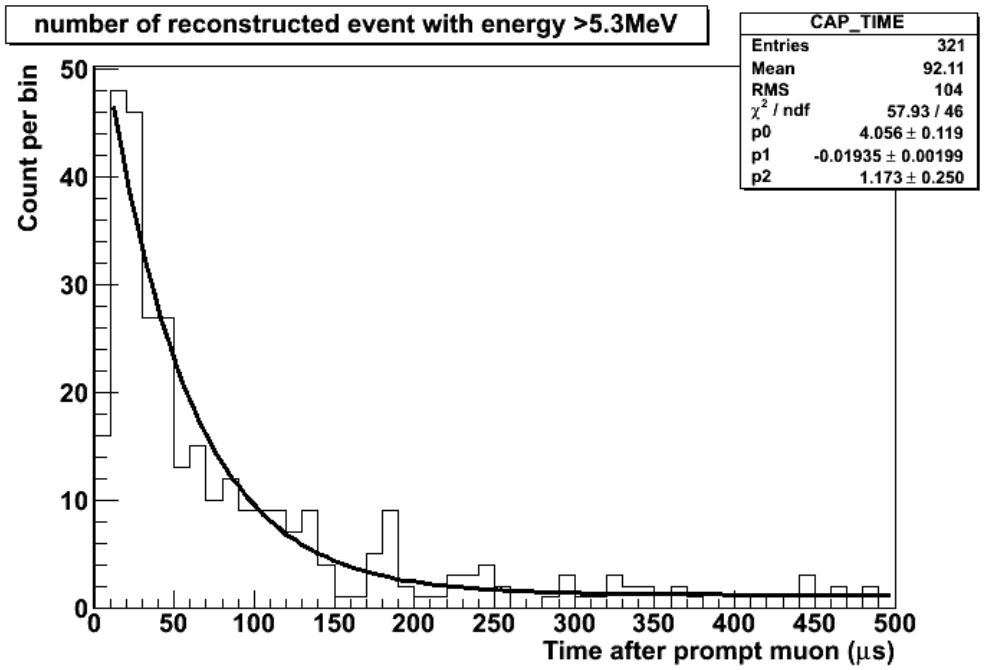

Figure 3.35: The distribution of neutron capture time with reconstructed energy > 5.3 MeV. The solid line is the fitted function $f(t)$.

307/(29.7%×95%), or 1088 ± 70(stat.) ± 65(sys.). With GdLS density of 0.855 gcm^{-3} and total muon track length of 1.4×10^7 cm, the muon induced neutron yield in GdLS was determined:

$$N_\mu = [0.91 \pm 0.06(\text{stat.}) \pm 0.05(\text{sys.})] \times 10^{-4}(n/(\mu\text{gcm}^{-2})). \tag{3.13}$$

Together with the simulation of the muon energy distribution shown in Fig. 3.36 [49], the angular distribution of the prompt muons shown in Fig. 3.33 were used for the calculation of the average muon energy. The mean of the energy of the prompt muons was calculated as:

$$< E >= \sum_{i=1}^{N_{bin}} f_i E_i / \sum_{i=1}^{N_{bin}} f_i, \tag{3.14}$$

where N_{bin} was the number of bins in Fig. 3.36, f_i was the count of the prompts in bin i, and E_i was the average muon energy in bin i. Eq. 3.14 gave the mean muon energy to be 92.5 GeV. The average neutron yield calculated using Wang's parameterization (Eq. 1.16) was,

$$< N_\mu >= \sum_{i=1}^{N_{bin}} f_i (4.14 \times 10^{-6} E_i^{0.74}) / \sum_{i=1}^{N_{bin}} f_i, \tag{3.15}$$

$1.01\times10^{-4}(n/(\mu\text{gcm}^{-2}))$.

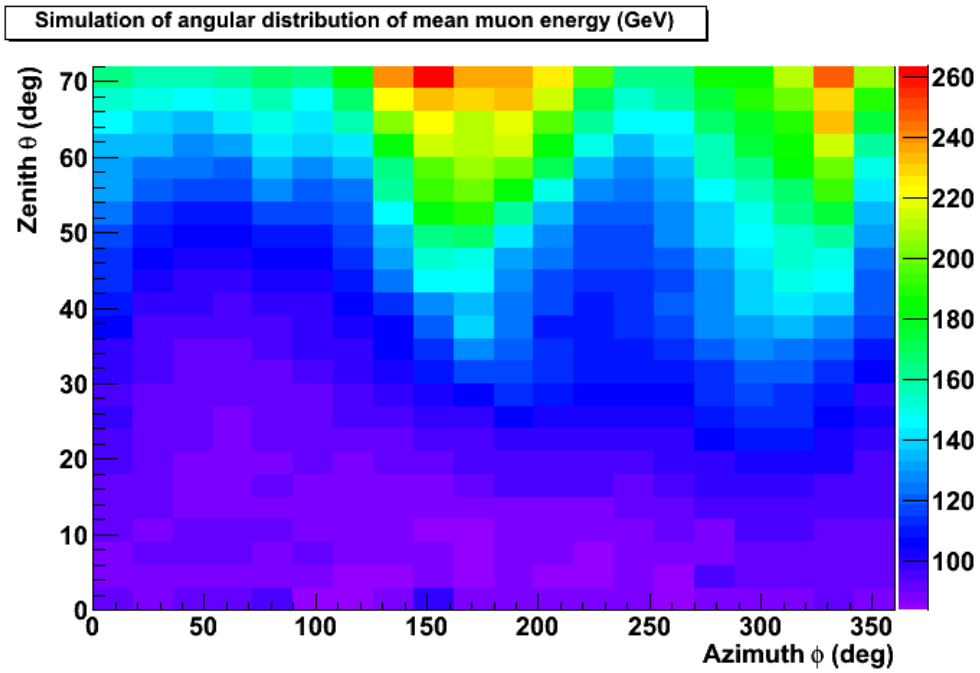

Figure 3.36: Simulation of the angular distribution of muons with average muon energy by LUK [49].

Chapter 4

Measuring muon induced neutrons using the Daya Bay anti-neutrino detectors

Muon induced neutrons were one of the backgrounds of the anti-neutrino detection in the Daya Bay experiment. Most of the neutrons can be effectively vetoed by the system in the anti-neutrino measurement [64, 10]. Yet, an accurate measurement of their rate was valuable for the background estimation of other underground particle physics experiments. My study was based on the analysis of the events triggered in the anti-neutrino detectors (AD) located in three experimental halls (EH).

The vertical overburden, muon rate, mean muon energy and number of ADs in the three EHs were shown in Table 4.1 [64, 10]. A 3D map of the mountain profile near the experimental halls was shown in Fig. 4.1 [65]. Among them, EH3 has the largest overburden while the other two were similar. Data of AD 1-6 was analyzed.

In this chapter, since the study was based only on the ADs, the detail structures

and working mechanisms of other detectors, such as the resistive plate chamber (RPC) and water pools, will not be discussed.

Table 4.1: Vertical overburden, muon rate, mean muon energy and number of anti-neutrino detectors in the three experimental halls [64, 10].

	Vertical overburden (water equivalence depth, m)	muon rate (Hz/ m^2)	mean muon energy (GeV)	Number of anti-neutrino detectors
EH1	250	1.27	57.4 ± 0.1	2 (AD1, 2)
EH2	265	0.95	58.5 ± 0.2	2 (AD3, 7)
EH3	860	0.056	136.1 ± 0.4	4 (AD4, 5, 6, 8)

4.1 Detector configuration

The ADs were more or less the same as the Aberdeen Tunnel neutron detector. Fig. 4.2 showed the schematic of the ADs in Daya Bay. Each AD consisted of a 5 m diameter stainless steel vessel (SSV) holding two UV transparent acrylic vessels (AV). The inner 3.1 m diameter AV, called the Inner AV (IAV), was holding 20 tons of Gadolinium doped liquid scintillator(GdLS). It was surrounded by a 4m diameter AV, called the Outer AV (OAV), which was filled with 20 tons of liquid scintillator (LS). Thirty seven tons of mineral oil (MO) were filled inside the SSV, surrounding the OAV. 192 8-inch Hamamatsu R5912 PMTs were attached on the inner walls of the SSV for the detection of scintillation light. A black radial shield and specular reflectors were installed on the SSV inner walls and top-bottom outer surfaces of OAV respectively. The black radial shield and the specular reflectors can improve the uniformity of the energy response and photon coverage. The GdLS density used was 0.866gcm^{-3}, which was 0.011 gcm^{-3} larger than that for

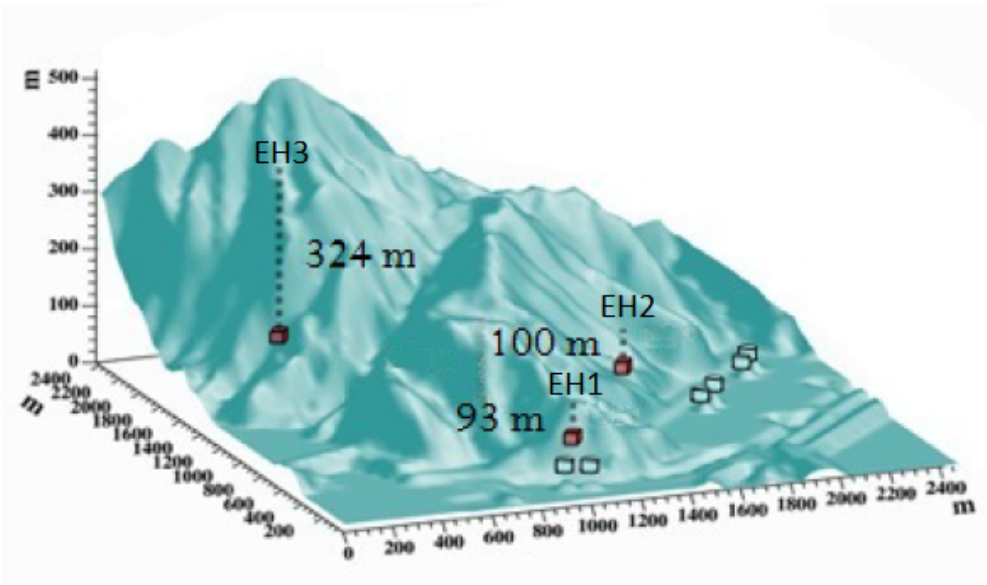

Figure 4.1: A 3D map of the mountain profile near the experimental halls [65].

the Aberdeen Tunnel neutron detector.

Three automatic calibration units, called ACU, were located on the top lid of the SSV. All of them had calibration pipes for the connection to the inner volumes. Two of them were connected to the center and edge, which was 135 cm from the center, of the IAV. The third one was connected to the OAV, 177 cm from the center. Radioactive sources (^{68}Ge, ^{241}Am^{13}C and ^{60}Co) and light sources were used for the calibration. Monitoring devices were installed to monitor the attenuation lengths of the liquids [11] (GdLS, LS and MO). Besides, sensors were installed to monitor different conditions of the detectors, such as liquid temperatures and levels. These monitoring devices were parts of the slow control system.

4.2 Detection mechanism

The mechanism for detecting a neutron was similar to that of the Aberdeen Tunnel neutron detector, details of which were discussed in Chapter 3, with the exception

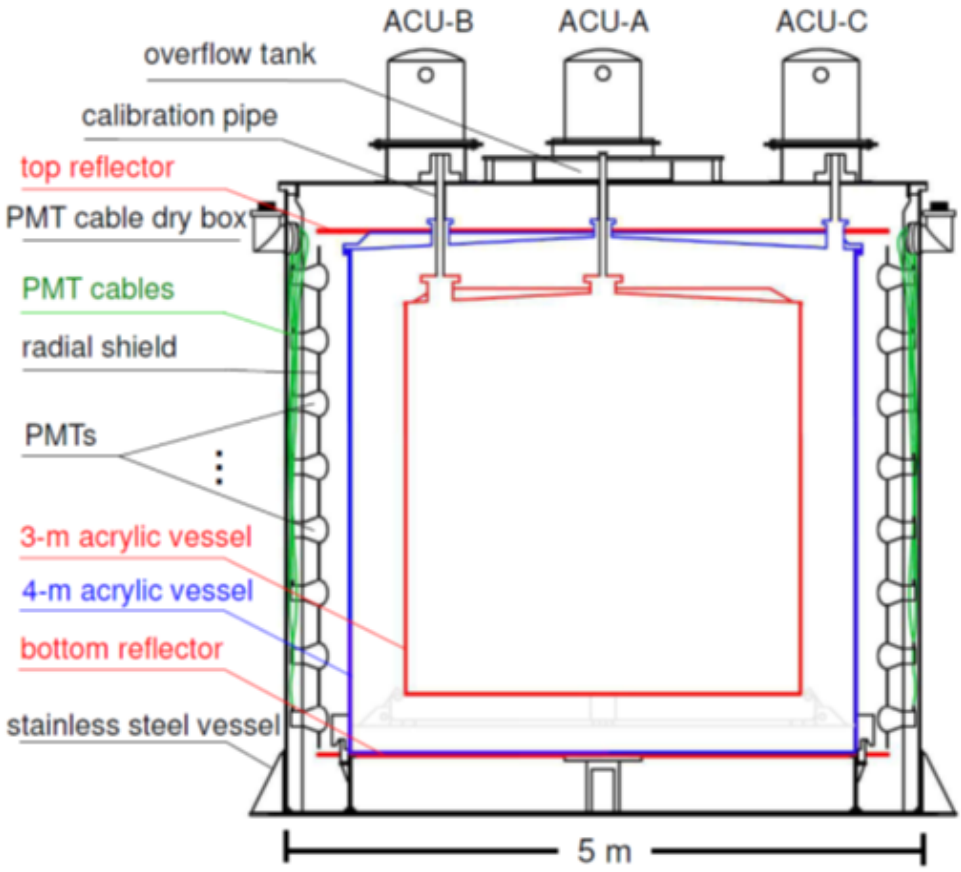

Figure 4.2: Schematic of the anti-neutrino detector in the Daya Bay Experiment [11].

that the ADs had an extra region between the OAV and IAV called the gamma catcher where only bare LS was filled. It was used for detecting the gamma's escaping from the target GdLS volume. As a result, the gamma escape is reduced, and hence the energy resolution is improved.

4.3 Energy scale calibration

From the baseline subtracted ADC values, quantities of charge (in unit of photoelectrons, or p.e.s) were converted in each read out channel, using the calibration constants for single photoelectron (spe), which were obtained by using low intensity LED and updated weekly. An example of the ADC distributions for spe of various PMTs was shown in Fig. 4.3.

From the total charge sum, Q_{tot}, over 192 PMTs in each AD of an event, the visible energy, E_{vis}, of the events was reconstructed by [11]:

$$E_{vis} = \frac{Q_{tot}}{C_E}, \tag{4.1}$$

where C_E was the energy calibration constant. In Eq. 4.1, C_E was determined in two ways. First, the energy of the ^{60}Co peak in the ^{241}Am^{13}C/^{60}Co source deploying in the AV center was constrained to be 2.5 MeV. This calibration was carried out once weekly. The reconstructed energy spectrum of the source was shown in Fig. 4.4. There were five peaks. For the AmC source, the peak at about 1 MeV was from the recoiled protons after collisions with neutrons, and the peaks at about 7.9 and 8.5 MeV were from the neutron capture by isotopes of ^{157}Gd and ^{155}Gd respectively. For the ^{60}Co source, the summed gamma emission peak was about 2.5 MeV, with a 1.5 MeV absorption peak by the source package materials [11]. The above double peaks are fitted with a Crystal ball function plus a Gaussian to avoid the bias from the asymmetry of the spectrum [11, 66].

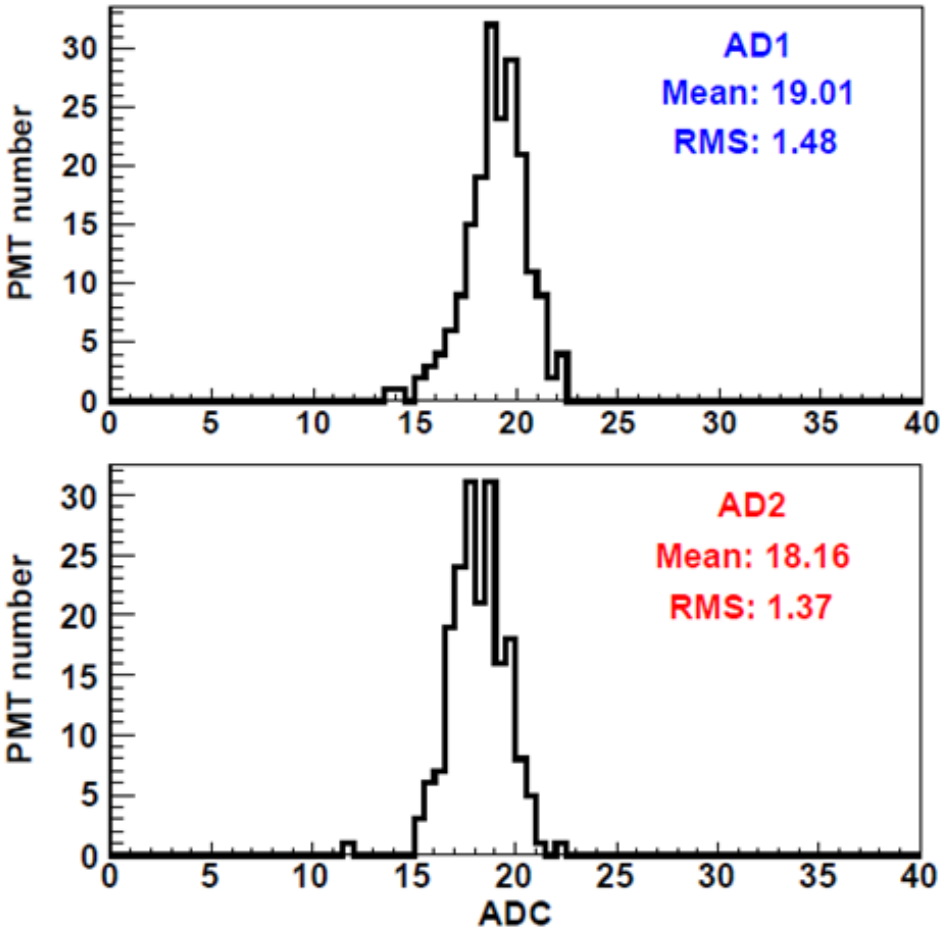

Figure 4.3: An example of the ADC, with baseline subtracted, distribution of spe's for various PMTs in AD1 and AD2 [11].

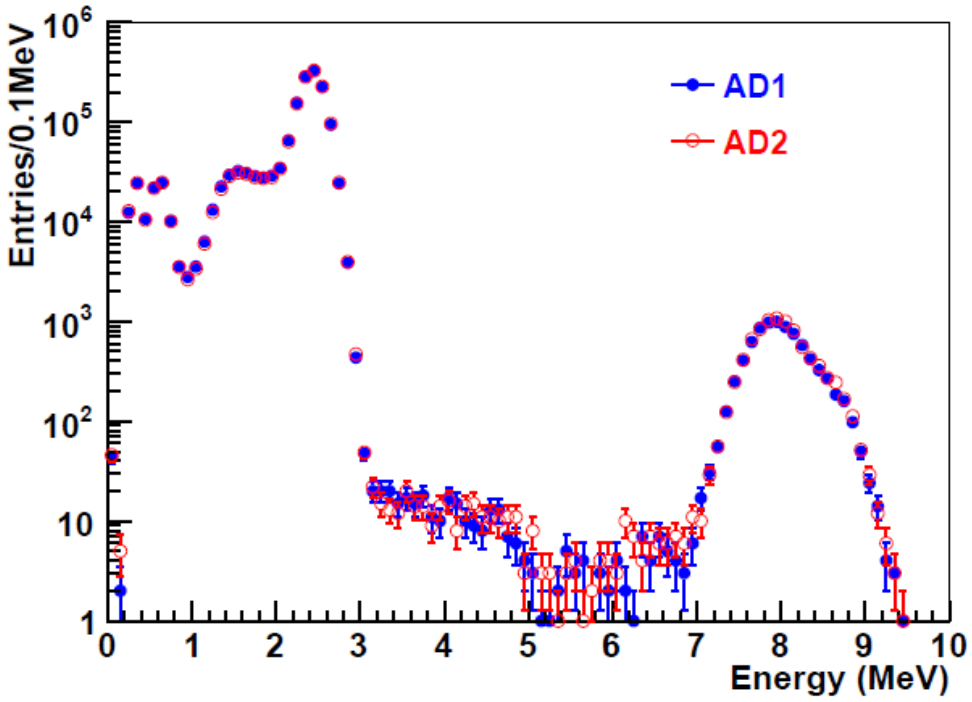

Figure 4.4: Reconstructed energy spectra of the combined source of ^{241}Am^{13}C/^{60}Co, for AD1 and AD2 [11].

Another way to determine C_E was to monitor the peak of muon induced neutron capture by Gd. This update, which was more frequent, can be done during regular physics runs. For AD1, C_E was about 160 p.e./ MeV. Fig. 4.5 showed the stabilities of the mean ADC to spe constant and the charge-energy constant.

4.4 Event reconstruction

For studying the muon induced neutrons, a vertex and energy reconstruction program called AdSimple was used. The PMT charge templates of numerous grid points (20 bins in R, 20 bins in Z and 24 bins in ϕ) distributed in the OAV generated by Monte Carlo (MC) simulation of Inverse Beta Decays (IBDs) were used in the vertex reconstruction. For each grid point, the PMT measured charge distribution of an event was compared with the corresponding PMT template charges, and the Chi-squared value of particular grid point was calculated by summing of a function of Poisson likelihood [11, 67] over all of the 192 PMTs. This results in a map of Chi-squared values for the grid points, and the grid point with the minimum value was located. Along each axis (R, Z and ϕ), two Chi-squared values of the adjacent grid points of the minimum point were picked up. Parabolic interpolation of these Chi-squared values along each axis was done to locate the position of the minimum Chi-squared value, which was the vertex. In the performance test, the overall mean and spread for the difference between the true and reconstructed Gd captured neutron event positions on the Gd captured neutron events were 14 mm and 179 mm respectively in R, and 1 mm and 202 mm respectively in Z [67].

For the energy reconstruction, the visible energy was calculated according to Eq. 4.1. However, the energy response of the AD was event position dependent. This was studied by examining muon induced neutron events. Parameterizations of the dependence along R and Z were applied as corrections. The corrected energy reconstruction of the Gd captured neutron events gave about 8.00 MeV

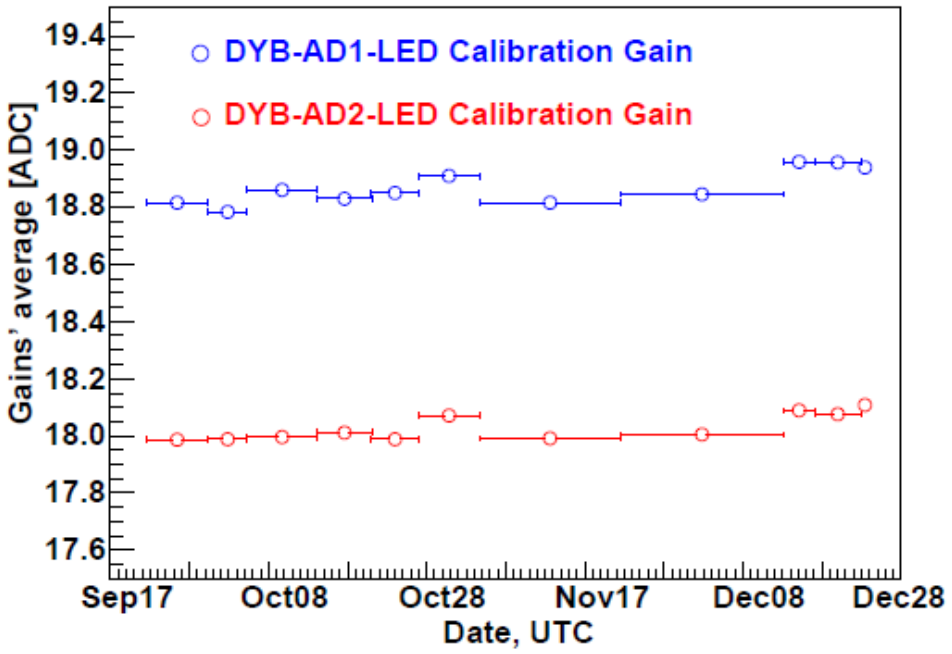

(a)

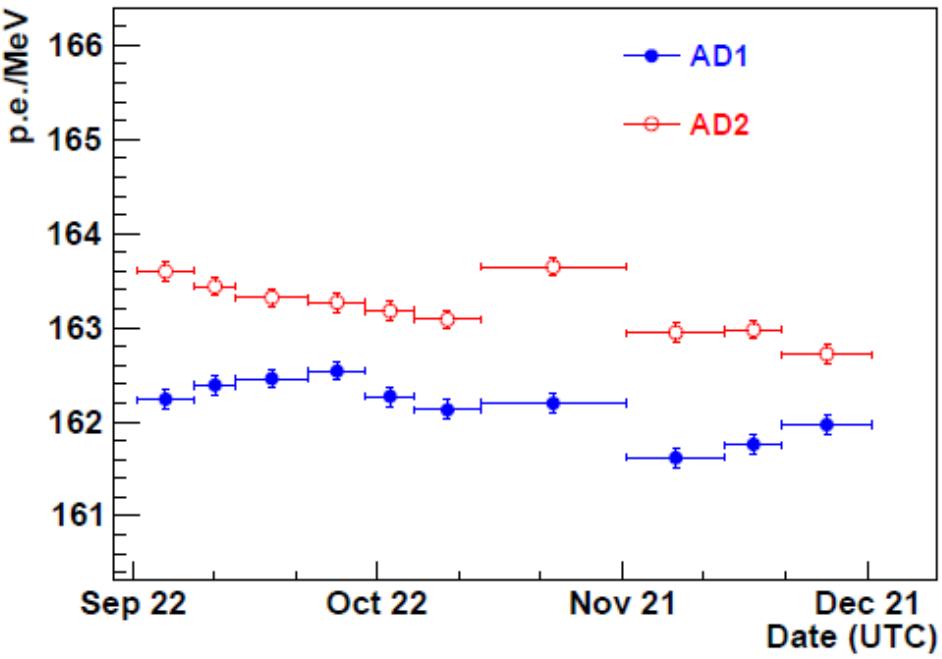

(b)

Figure 4.5: Stabilities of (a) the mean ADC to spe constant and (b) the charge-energy constant for AD1 and AD2 during 2011 [11].

mean energy with variations of ± 0.05 MeV along R and Z directions. Details of the reconstruction are discussed in Ref. [11].

4.5 Muon induced neutron measurement and results

Two AD triggering schemes, called NHIT and ESUM, were used. The threshold of individual PMT channel was 0.25 p.e.. For NHIT, the AD triggering condition was any 45 PMTs triggered out of the total 192 PMTs. For ESUM, events with total charge sum larger than 65 p.e.s, ($\sim$ 0.4 MeV) would trigger the AD. Under the NHIT or ESUM trigger conditions, the AD trigger rate was smaller than 280 Hz for each AD. The muon induced neutron measurement was taken during regular physics runs. Data taken during 2012 were analyzed. The muon induced neutron rates of the ADs were much higher than that in the Aberdeen Tunnel Laboratory, because of the much larger GdLS target volume. About a week of data for ADs of EH1 and EH2 (few times more for EH3) gave statistical uncertainty $< 1\%$.

Events with reconstructed energy larger than 3000 p.e.s ($\sim$ 20 MeV) were classified as muon events. The measured muon event rates per AD in EH1, EH2 and EH3 were 21 Hz, 16 Hz and 1 Hz respectively.

4.5.1 Event selection

Since the AD muon trigger rates were much higher than that in the Aberdeen Tunnel ND, a muon multiplicity cut was applied for the prompt selection criteria. Events with reconstructed energy (E_p) $>$ 20 MeV and no additional event with same criteria occuring within ± 1 ms, except within +10 μs (duration of ringing and after pulses, false DAQ signals [68, 10]), were treated as prompt events. Fig. 4.6 showed examples of the number of AD triggers in EH1 AD1 against re-

constructed energy and time since the prompts. In Fig. 4.6(a), there were more events of nGd capture around 8 MeV, while no time correlated peak was found for the background plotted in Fig. 4.6(b). The event selection criteria for neutron candidates and backgrounds were reconstructed energy of 6 MeV to 12 MeV and within time window of 10 μs to 210 μs (neutron candidates) and -10 μs to -210 μs (backgrounds). The lower limit of 10 μs of the time window was imposed to avoid counting the retriggered false signals due to ringings and after pulses happening within 10 μs after a prompt trigger.

4.5.2 Global parameters and efficiencies used for neutron yield calculation

The global efficiencies and parameters used for the three EHs were shown in Table 4.2. The Gd capture ratio ϵ_{Gd} was defined as:

$$\epsilon_{Gd} = \frac{nGd}{nH + nGd}, \tag{4.2}$$

where nH was the number of hydrogen captured neutrons and nGd was the number of Gd captured neutrons. The ratio was related to the cross sections of neutron capture and concentrations of Gd and H. All the parameters and efficiencies were determined by MC simulations [64, 10].

4.5.3 Results and discussion

For AD1 of EH1, with 5099105 $\pm$ 2300 prompt muons, the total number of‘ neutron candidates was 38359 $\pm$ 197, with 2304 $\pm$ 48 backgrounds. The results for other ADs will be summarized later. The nGd capture time distribution for neutron candidates was shown in Fig. 4.7. The solid line was the fitting. The functional form of the fitting was the same as Eq. 3.12 used in the case of the Aberdeen Tunnel

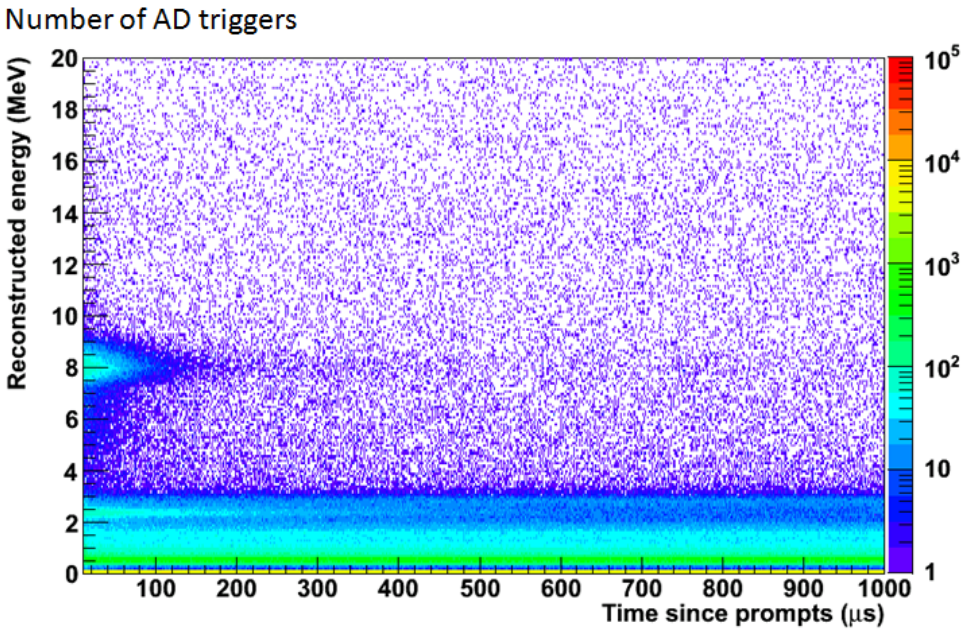

(a)

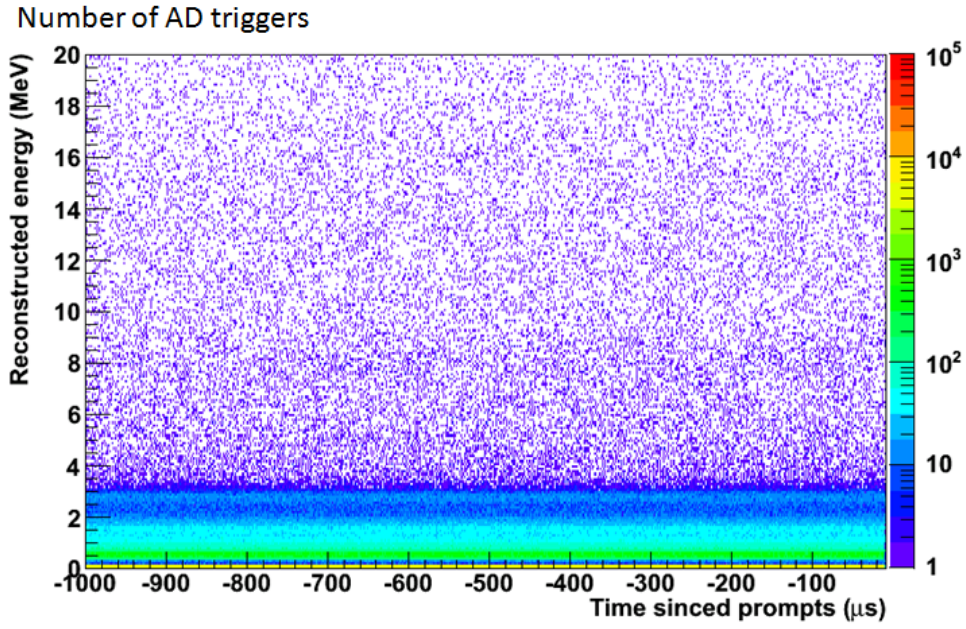

(b)

Figure 4.6: The number of AD triggers in EH1 AD1 against reconstructed energy and time since the prompts, for (a) neutron candidates, and (b) background.

Table 4.2: Global parameters and efficiencies used for neutron yield calculation.

	parameters or efficiencies	uncertainties
Gd capture ratio, ϵ_{Gd}	0.853	1%
GdLS density (gcm^{-3})	0.866	1%
Time cut efficiency, ϵ_{time} (%)	82.4	2.3
Energy cut efficiency, ϵ_{en} (%)	97.6	2

Experiment. The best-fit result for $p1$ was -0.03382 $\pm$ 0.00039, corresponding to the capture time constant τ_{cap} of (29.8 $\pm$ 0.3) μs. This agreed with the capture time from simulations of (29.9 $\pm$ 0.7) μs for muon induced neutrons.

The reconstructed energy distribution of neutron candidates and background were shown in Fig. 4.8. The long low energy tail of the 8 MeV nGd capture events was due to the energy leakage. The nH capture peak was about 2.2 MeV.

The reconstructed vertex positions of AD1 EH1 were shown in Fig. 4.9. In the figure, where R and Z were the radial and vertical distances from the AD center. There were nGd captures found outside the IAV (R and Z = 1.55 m). Those were the reconstruction falses from events happening near the inner edge of the IAV. This implied that most of background neutrons were captured there, as shown in Fig. 4.9(b). In Fig. 4.9(a), there was a grid like structure in the reconstructed event positions inside the IAV, which results from the reconstruction bias as discussed in Ref. [67].

A scaling analysis was used for the neutron yield calculation. It can correct for the spill-in/out of the neutron vertices due to either reconstruction or physical diffusion. The analysis can determine parameters which are detector geometry independent, called neutron detection density and total track length density for the neutron yield calculation. This was based on counting the included neutron

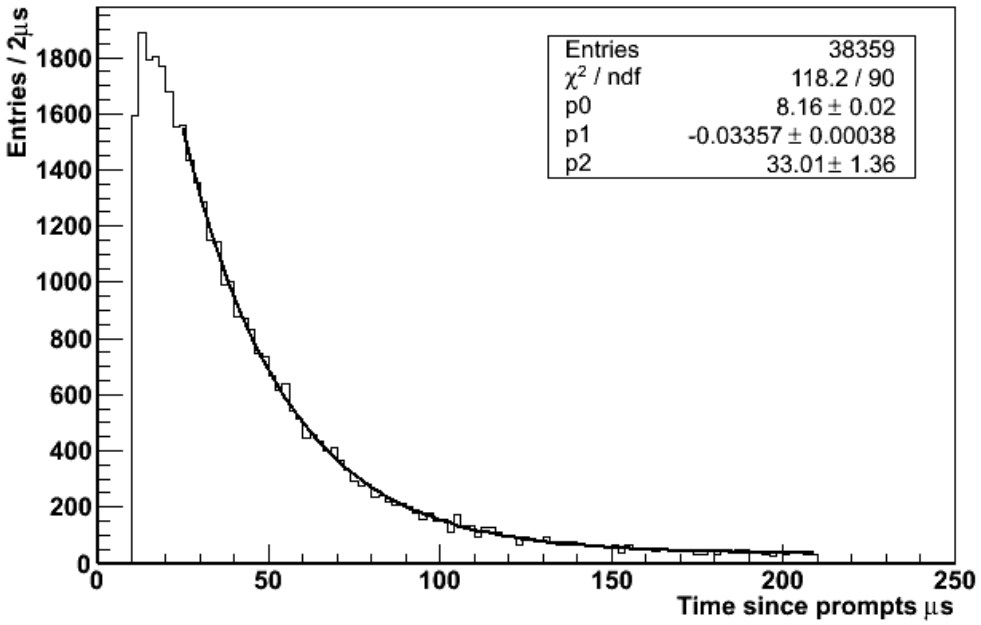

Figure 4.7: Distribution of neutron capture time of AD1 in EH1 with reconstructed energy > 6 MeV and < 12 MeV. The solid line was the fitted function.

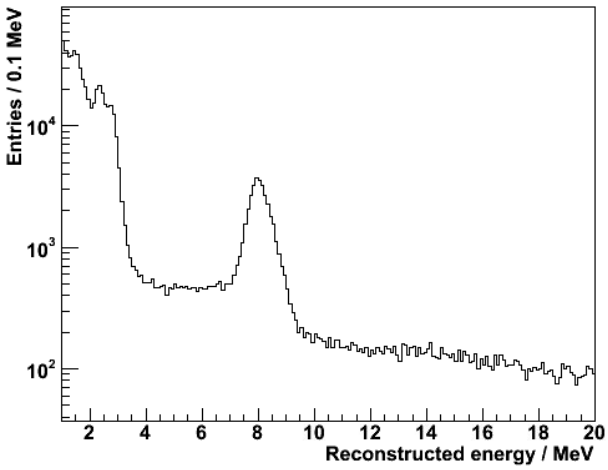

(a)

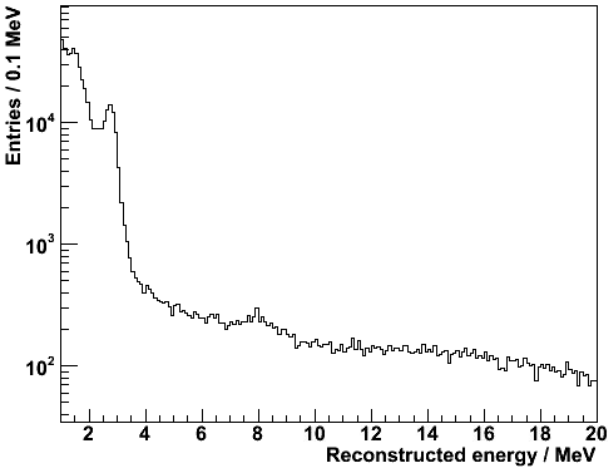

(b)

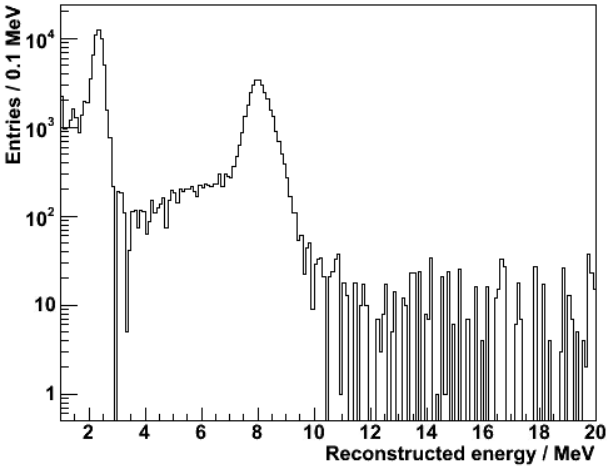

(c)

Figure 4.8: Reconstructed energy distribution, for AD1 EH1, of (a) the neutron candidates, 10 to 210 μs since prompts, (b) background, -10 to -210 μs since prompts and (c) the background subtracted neutron candidates, (a) - (b).

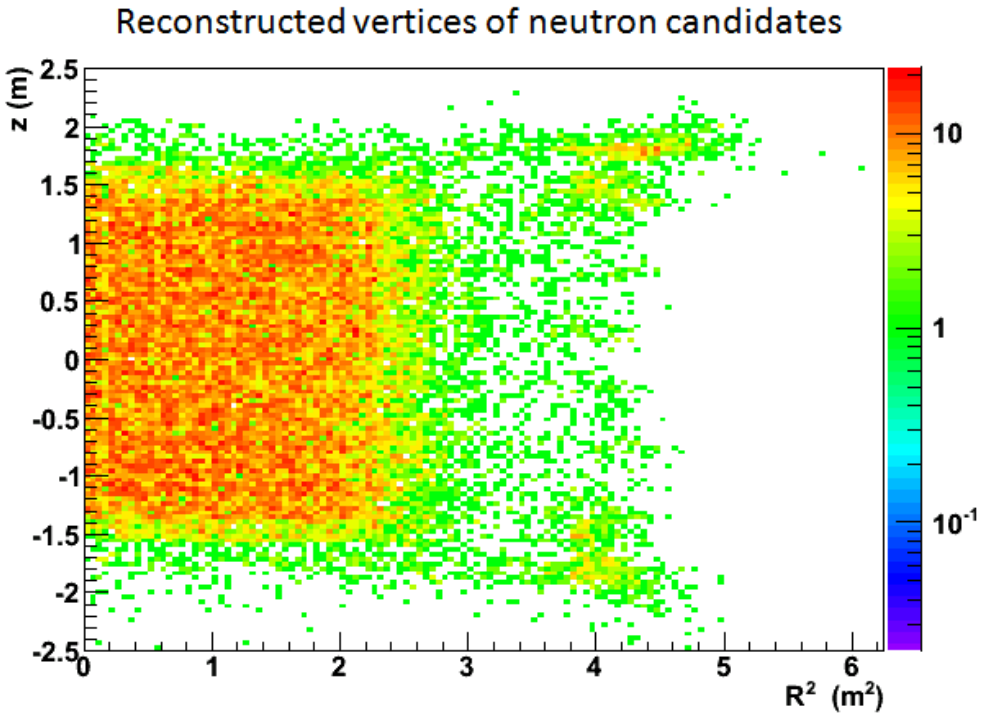

(a)

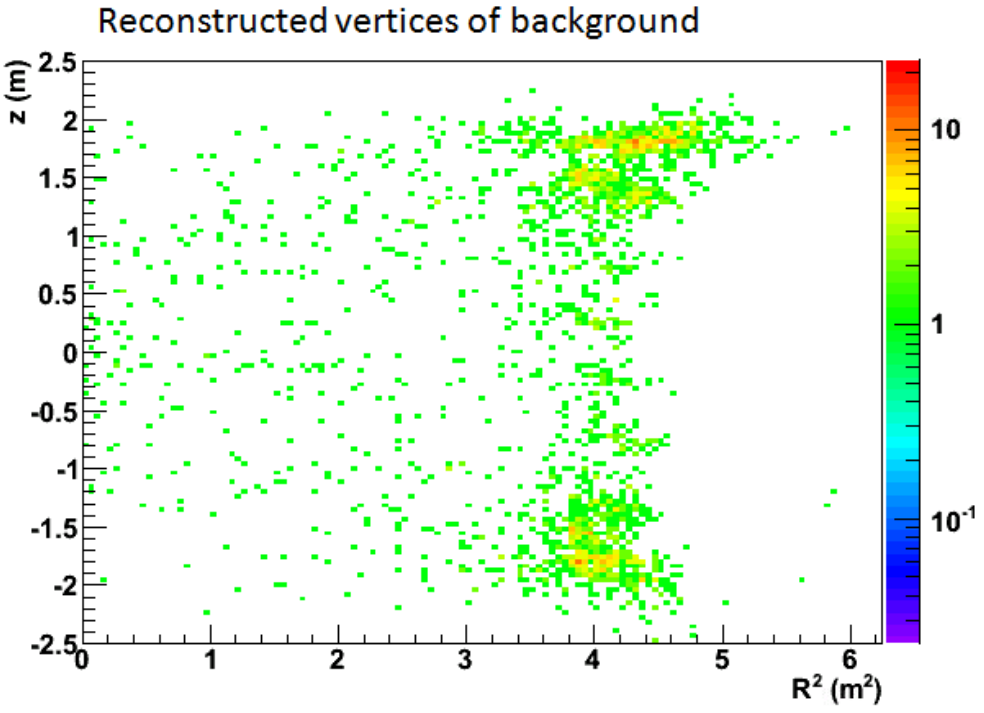

(b)

Figure 4.9: Reconstructed vertex positions for AD1 in EH1, for (a) neutron candidates, and (b) background.

vertices as a function of the fiducial volumes.

In the fiducial volume with an arbitrary shape, the number of neutron candidates measured N_m inside the volume was:

$$N_m = N_{gen} + N_{spill-in} - N_{spill-out}, \tag{4.3}$$

where N_{gen} was the number of neutron candidates generated inside the fiducial volume, $N_{spill-in}$ ($N_{spill-out}$) was the number of spill-in (spill-out) neutron candidates, ie., those generated outside (inside) but captured inside (outside) the fiducial volume. The only assumption we make is that N_{gen} scales as the volume V, while $N_{spill-in}$ and $N_{spill-out}$, being surface effects, both scale as the surface area S of the fiducial region. Eq. 4.3 can be written as:

$$N_m = aV + b_1 S - b_2 S = aV + bS, \tag{4.4}$$

where a, b_1, b_2 and b were proportionality constants called neutron detection volume density (unit: length^{-3}), spill-in, spill-out, and net spilling surface densities (unit: length^{-2}) respectively. a and b were constants if the fiducial volume was sitting in the region of isotopic and uniform vertex distribution. By scaling the size of the fiducial volume, a and b can be determined from the data. In order to minimize the effect of non-uniformity arising from the grid-like distribution of the reconstruction vertices, which was correlated with the AD coordinate system, a spherical fiducial volume was used for the analysis. Therefore, Eq. 4.4 became:

$$N_m = \frac{4\pi}{3} a R^3_{sphere} + 4\pi b R^2_{sphere}. \tag{4.5}$$

Rearranging the equation:

$$\frac{N_m}{R_{sphere}^2} = \frac{4\pi}{3} a R_{sphere} + 4\pi b, \tag{4.6}$$

where R_{sphere} was the radius of the fiducial volume. Hence, by changing R_{sphere} of the sphere, a and b can be determined from the slope and intercept of the plot of $\frac{N_m}{R_{sphere}^2}$ against R_{sphere} as shown in Fig. 4.10. Here, N_m was the number of the neutrons with background subtracted inside the radius R_{sphere} of the fiducial volume. The plot showed a deviation from linearity for $R_{sphere} > 1.4$ m, where the boundary effect of the detector appeared. The range of the linear fitting was $R_{sphere} = R_{scan}$ – 0.5 m to $R_{sphere} = R_{scan}$. R_{scan} was scanned and the results were shown in Fig. 4.11. The mean value fitted by the red lines for neutron detection density a and net spilling density b were 1553 ± 30 m^{-3} and -2 ± 9 m^{-2} respectively.

The scaling method was also applied for the total muon track length determination. A MUSIC simulation of muon angular distribution, shown in Fig. 4.12, was the input for the calculation. In order to normalize the total track length, the number of muons (N_{prompt}) having at least 100 mm track length, which was equivalent to 20 MeV deposited inside the OVA (LS plus GdLS regions, radius = 1982 mm, height = 3964 [69]) was found. The total track length per muon was proportional to the fiducial volume:

$$\frac{L_{tot}}{N_{prompt}} = cV, \tag{4.7}$$

where L_{tot} was the total track length spanned by the N_{prompt} muons inside the volume and c was the proportional constant called normalized total track length density (unit: length^{-2}), which was independent of the shape of the fiducial volume. Analyses using cylindrical and spherical fiducial volumes were applied. Fig.

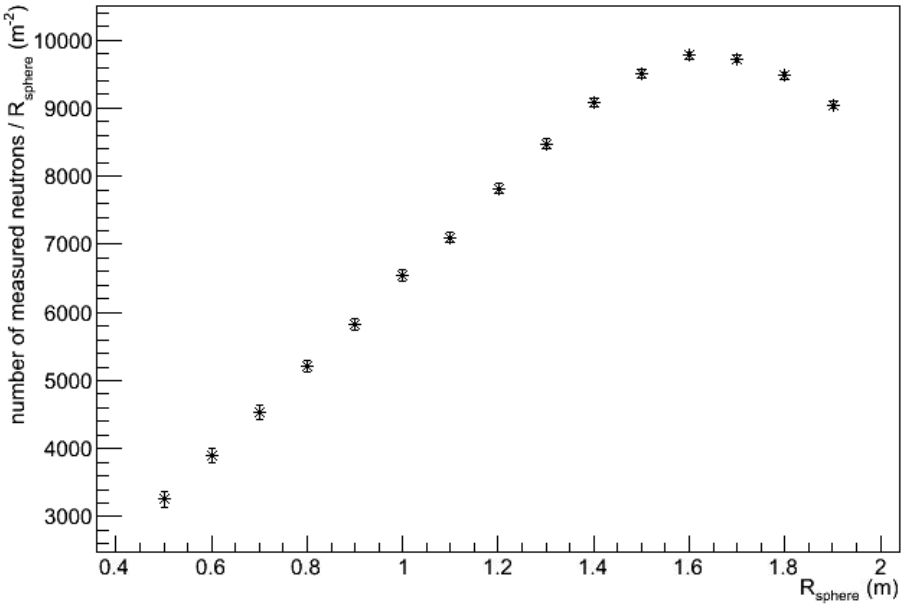

Figure 4.10: A plot of $\frac{N_m}{R^2_{sphere}}$ against R_{sphere} for AD1 in EH1.

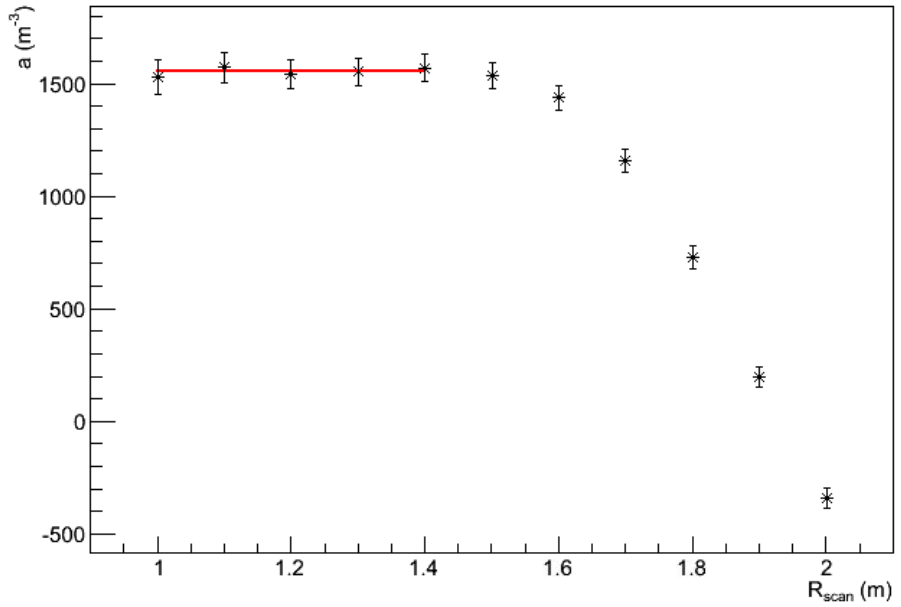

(a)

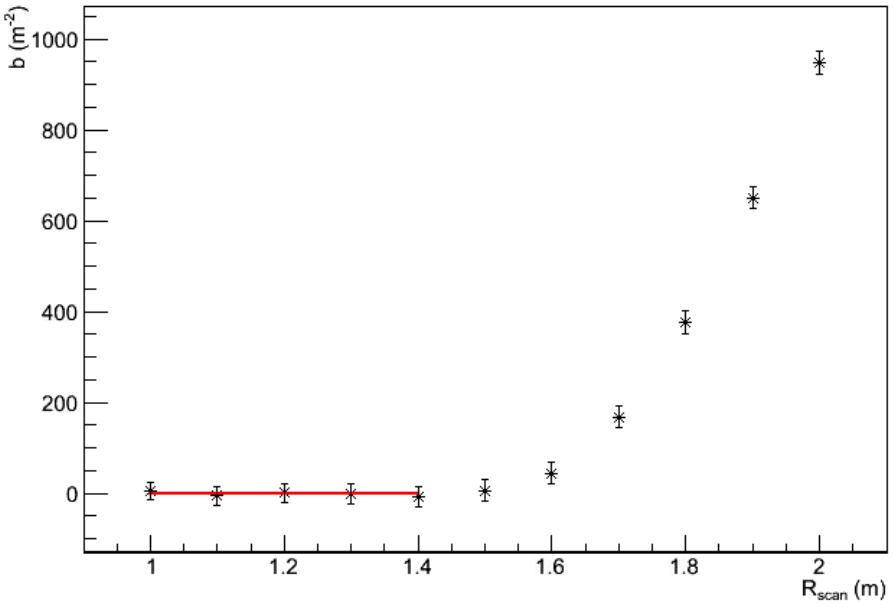

(b)

Figure 4.11: Fitted parameters a and b from Fig. 4.10. The fitting range was $R_{sphere} = R_{scan}$ – 0.5 m to $R_{sphere} = R_{scan}$. The red lines are the constant fits applied to evaluate a and b.

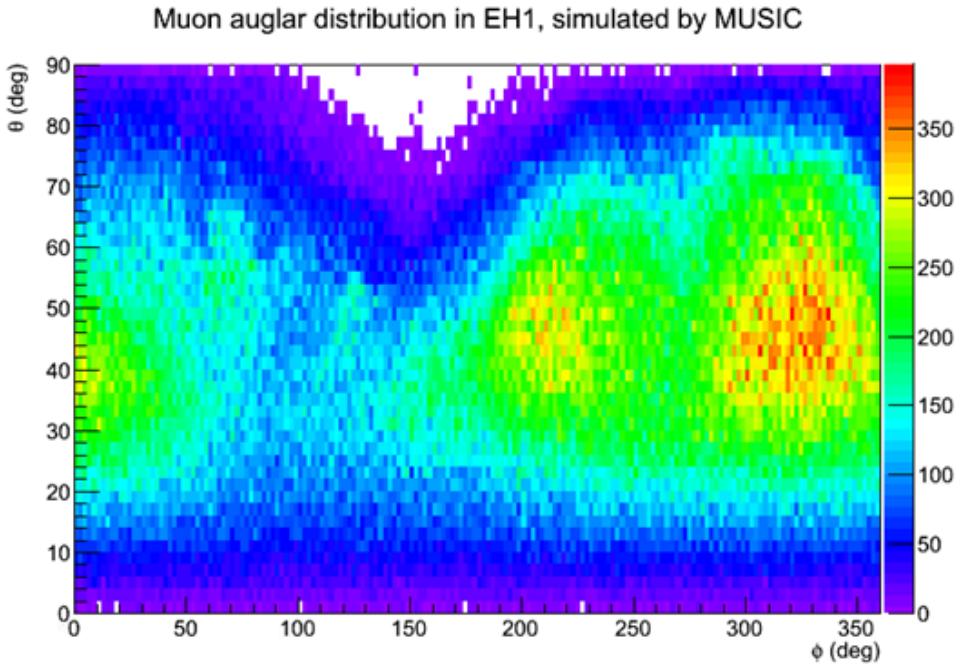

Figure 4.12: MUSIC simulation of muon angular distribution in EH1 [32, 10].

4.13 showed the plot of total track length per N_{prompt} against the scaling volume. Both shapes of the volumes showed linear properties, and the slopes were in good agreement with each other. The normalized total track length density was determined to be 0.0546 ± 0.0005 m^{-2}.

The neutron yield was calculated by:

$$\begin{aligned}
&\text{neutron yield} \\
&= \frac{\text{neutron detection density/efficiencies}}{\text{normalized total track length density} \times \text{number of prompts} \times \text{GdLS density}} \\
&= \frac{a/(\epsilon_{time}\epsilon_{en}\epsilon_{Gd})}{c \times \text{number of prompts} \times \text{GdLS density}},
\end{aligned} \tag{4.8}$$

where ϵ_{time}, ϵ_{en} and ϵ_{Gd} are defined in Table 4.2. Hence, the neutron yield for AD1

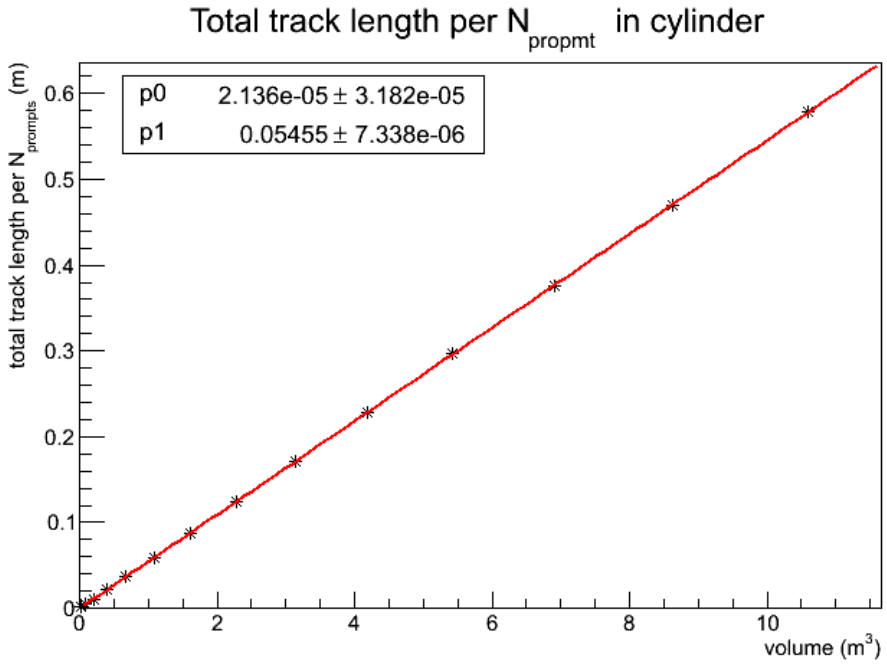

(a)

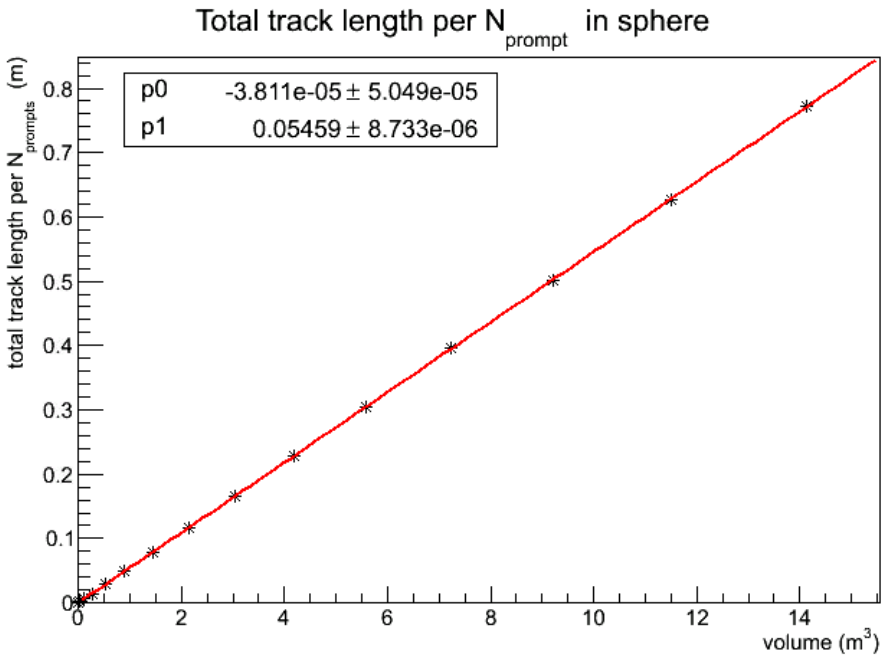

(b)

Figure 4.13: Total track length per N_{prompt} against the volumes under the muon flux in EH1, simulated by MUSIC. Red lines are the linear fittings of the MUSIC simulated data, indicated by the stars. The slopes ($p1$) for (a) cylindrical and (b) spherical fiducial volumes agree with each other.

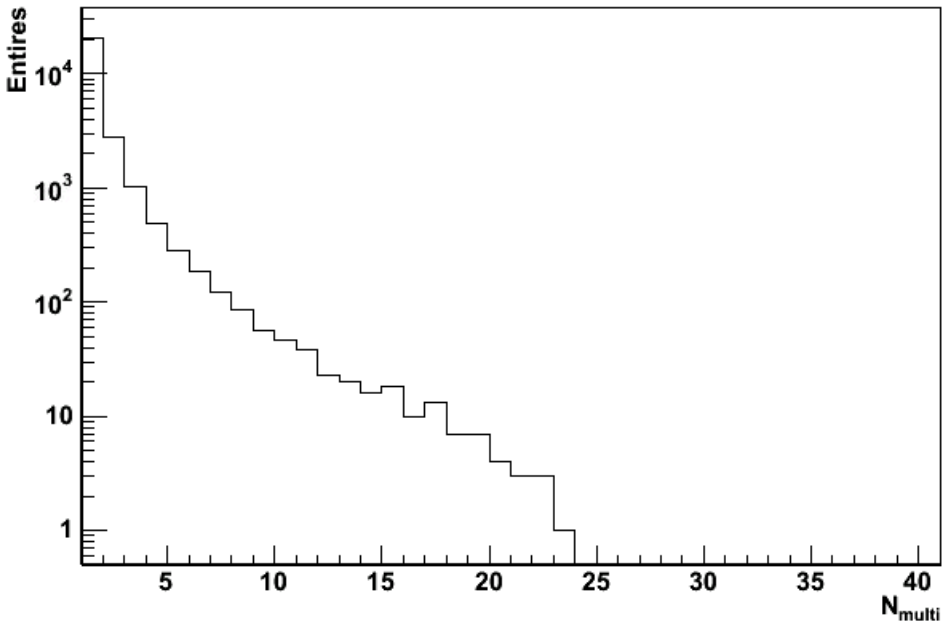

Figure 4.14: Distribution of nGd capture multiplicities (N_{multi}) for each prompt within the time and energy window, for AD1 in EH1.

in EH1 was:

$$N_\mu = [0.94 \pm 0.04] \times 10^{-4}(n/(\mu\text{gcm}^{-2})). \tag{4.9}$$

The distribution of nGd capture multiplicities for each prompt within the time and energy window was shown in Fig. 4.14. The ratio of single nGd to total nGd captures per prompt was $20406/38359 = 0.53 \pm 0.01$.

The analysis was applied to other five ADs. Table 4.3 summarized the results. Fig. 4.15 plotted the neutron yields, fitted nGd capture time constants and the ratios of single nGd to total nGd captures per prompt for all six ADs.

The nGd capture time constants for six ADs were quite consistent with each other. This was because the neutrons were thermalized before being captured. Therefore the capture time constants were not dependent on the muon energy. The ratio of single to total nGd captures in EH3 was smaller than those in EH1

Table 4.3: Summary of six AD measured results.

	AD1	AD2	AD3	AD4	AD5	AD6
Number of prompts	5119900 ± 2300	5120100 ± 2300	3615400 ± 1900	1756100 ± 1300	1766200 ± 1300	1758700 ± 1300
$a(\mathrm{m}^{-3})$	1553 ± 30	1555 ± 23	1030 ± 18	942 ± 18	918 ± 16	883 ± 16
$b(\mathrm{m}^{-2})$	-2 ± 9	-7 ± 6	0 ± 5	-8 ± 4	-9 ± 4	-10 ± 4
$c(10^{-2}\mathrm{m}^{-2})$	5.46 ± 0.05	5.46 ± 0.05	5.46 ± 0.05	5.45 ± 0.05	5.45 ± 0.05	5.45 ± 0.05
Neutron yield $(10^{-4}\frac{n}{\mu\mathrm{gcm}^{-2}})$	0.94 ± 0.04	0.94 ± 0.04	0.88 ± 0.04	1.66 ± 0.08	1.61 ± 0.07	1.55 ± 0.07
$\frac{\text{Singles}}{\text{Total}}$	0.53 ± 0.01	0.53 ± 0.01	0.53 ± 0.01	0.41 ± 0.01	0.43 ± 0.01	0.43 ± 0.01
$\tau_{cap}(\mu s)$	29.8 ± 0.3	29.6 ± 0.3	29.9 ± 0.4	30.0 ± 0.5	29.7 ± 0.4	29.8 ± 0.5

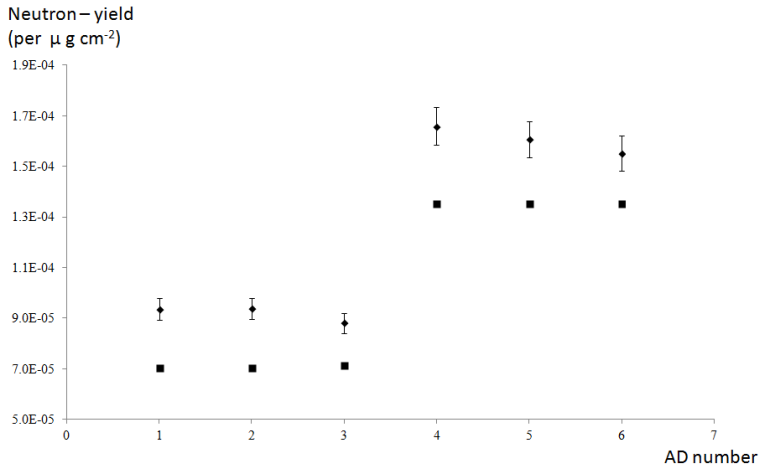

(a)

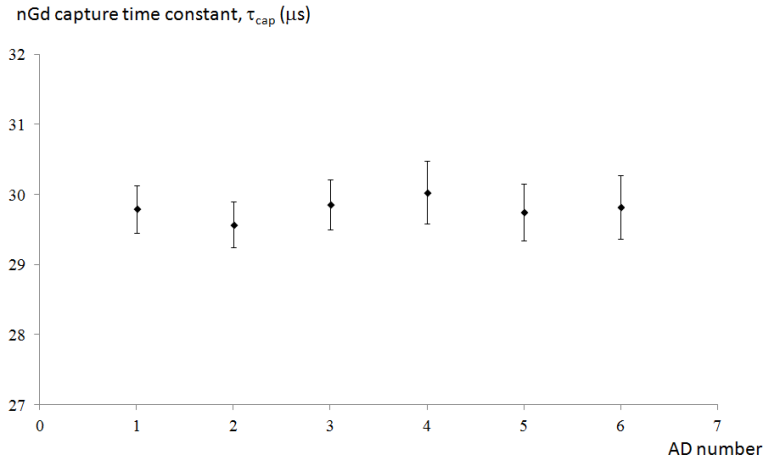

(b)

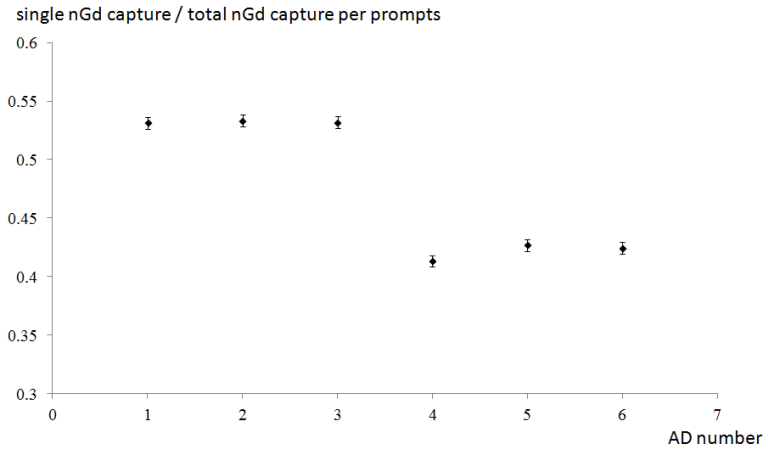

(c)

Figure 4.15: (a) The neutron yields of data (square) and Wang's parameterization (circle), (b) fitted nGd capture time constants and (c) ratios of single nGd to total nGd captures for each prompt of six ADs.

and EH2. This was because the muons penetrating into EH3 have higher energy on average and generate more neutrons.

In Fig. 4.15(a), the neutron yields for EH1 and EH2 were similar. They were smaller than those in EH3. The neutron yields for EH1, EH2 and EH3 were 0.94 $\pm$ 0.03, 0.88 $\pm$ 0.04 and 1.61 $\pm$ 0.05 ($10^{-4}n/(\mu\text{gcm}^{-2})$) respectively. The corresponding neutron yields calculated by Wang's parameterization using Eq. 3.15 were 0.70 (EH1), 0.71 (EH2) and 1.35 (EH3) ($10^{-4}n/(\mu\text{gcm}^{-2})$). The stability of the neutron yield among ADs in the same EH showed the merit of the analysis method. Moreover, the method of spilling effect correction was data driven only, instead of using MC simulation. Events happened near the boundary of the GdLS region were not considered, and hence for those cut efficiency corrections from simulations. The large uncertainties of the parameters b was due to the grid-like distribution of the reconstruction vertices. This violated the isotopic assumption of the analysis slightly. Besides, the parameters b of EH3 were slightly negative beyond the uncertainty. This was due to the outward bias of the vertex reconstruction in EH3, which was slightly larger than those in other EHs. One would get better results if the reconstruction would be improved in the future.

Chapter 5

Summary and conclusion

CRs on the surface were studied. Properties of surface CR muon variations, included zenith angle dependence, East-West effect and atmospheric effect, were measured by a home-built detector CMT. For the measurement of the Zenith angle dependence, the vertical axis of the telescope was tilted to point at different zenith angles for count rate measurement. The modified Gaisser formula was compared with the result. The fitted chi-squared per degree of freedom is 14.5/7. For the East-West count asymmetry measurement, the telescope was rotated four times in taking data so as to eliminate possible differences in the combo efficiencies. The East-West count asymmetries for the 1-offset and 2-offset combos were about 8% and 14% respectively, in good agreement with a GEANT4 simulation. For the measurement of the CR count rate time series, the telescope was set to point vertically upward, and data was taken from 20^{th} Jan to 4^{th} June of 2012. The time series of the data was analyzed in different time ranges, daily, monthly and seasonally. There was a day-night count asymmetry, with more night counts than day counts. The variation was about 2% from the mean. The surface temperature and pressure were compared with the series. A highly negative correlation of the surface temperature and the muon count time series was found, averaging -0.76.

A model was developed for the observation, in which the muon production, stopping and decay in an atmosphere in hydrostatic equilibrium are described by two coupled differential equations. The model showed the relationship of the changes in the muon counts with the surface air density, while the surface pressure was regarded as a correction for the muon counts due to the total air mass change. The coefficient of the correction was fitted to the data. We concluded that after the correction the surface temperature effect on CMT was -0.6 (%/°C), while the barometric effect -0.5 (%/hpa) on CMT.

CRs in underground and the muon induced neutrons were studied in the Aberdeen Tunnel Experiment. The angular response of the tracker and energy scale of the neutron detector were obtained from the calibrations. Event reconstructions were developed for the tracker and the neutron detector. The muon angular flux distribution was compared with the MUSIC simulation with the mountain profile as the input. They showed good agreement, except for $\theta \approx 60°$. Further study is required for the deviation there. The time series was stable over the whole time period. Binning the entire time series into the 24-hour series, we observed a small day-night count asymmetry was observed. The night counts were higher than the day counts with variations of about 1% from the mean. For the muon induced neutron measurement, event selections based on minimization of the total uncertainty ratio for delayed signals and backgrounds were applied. Data of the accumulated run time of about 175 days gave the number of neutrons to be 343 and 36 backgrounds, with 166852 prompts. After efficiency correction and division of parameters, the neutron yield was determined to be $[0.91\pm0.06(\text{stat.})\pm0.05(\text{sys.})]$ $(10^{-4}n/(\mu\text{gcm}^{-2}))$. Using the track information from MUSIC simulation, the mean muon energy was 93 GeV. The corresponding average neutron yield calculated by Wang's parameterization was 1.18 $(10^{-4}n/(\mu\text{gcm}^{-2}))$.

The muon induced neutrons was also studied in the Daya Bay Reactor Neu-

trino Experiment using the anti-neutrino detectors located in three underground experimental halls. The mean muon energies for EH1, EH2 and EH3 were 57, 58 and 137 GeV respectively. For the muon induced neutron measurement, the muon multiplicity cut was applied for the prompt selection criteria. A scaling analysis was developed for the neutron yield calculation. It corrects for the spill-in/out of the neutron vertices due to either reconstruction or physical diffusion, based on simple geometric assumptions. Moreover, the analysis was data driven, instead of relying on complicated MC simulations. Neutron detection density and normalization total track length density were obtained. The total track length was normalized by the number of muons, from the MUSIC simulation, passing the criteria equivalent to the prompt muon selection criteria for the experimental data. The division of neutron detection density by the normalized total track length density and other parameters and efficiencies gave the neutron yield. Data of six ADs were analyzed, and the results showed a good stability of the capture times over six ADs. The neutron yields and the ratios of single to total nGd captures also showed good stability among the ADs in the same EH. The averaged neutron yields for EH1, EH2 and EH3 were 0.94 $\pm$ 0.03, 0.88 $\pm$ 0.04 and 1.61 $\pm$ 0.05 ($10^{-4}n/(\mu\text{gcm}^{-2})$) respectively. The corresponding average neutron yields calculated by Wang's parameterization were 0.70, 0.71 and 1.35 ($10^{-4}n/(\mu\text{gcm}^{-2})$) respectively.

Fig. 5.1 compared the neutron yields of the Aberdeen Tunnel Experiment and the Daya Bay Experiment with other experimental results. They showed good agreement with a trend. The neutron yield comparison of the experimental results with the ones obtained by Wang 's parametrization using mean muon energy, as shown in Fig. 1.10, is not appropriate, since the muon energies are not single-valued in the realistic cases. It is better calculating the average neutron yield as given by Eq. 3.15.

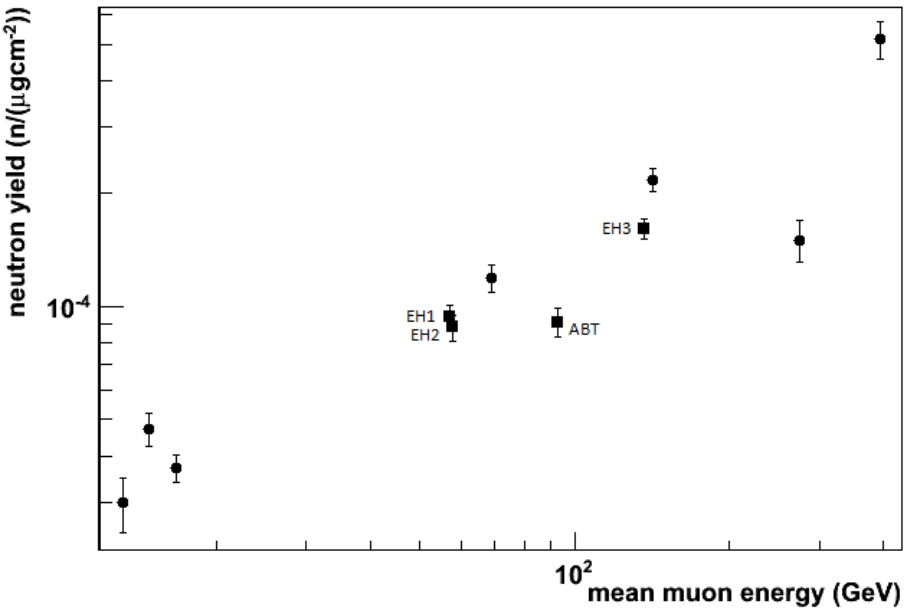

Figure 5.1: Comparison of the neutron yields (squares) in the Aberdeen Tunnel (ABT) and Daya Bay (EH1, EH2 and EH3) Experiments with other experimental results (circles).

Bibliography

[1] R. Kronig et al. *Collected Sci, Papers*, vol. 2, p. 1313, 1964.

[2] John N. Bahcall *Rev. Mod. Phys.*, vol. 50, p. 881, 1978.

[3] V. Gribov and B. Pontecorvo *Phys. Lett. B*, vol. 28, p. 493, 1969.

[4] R.G.H. Robertson *Prog. Part. Nucl. Phys.*, vol. 57, p. 90, 2006.

[5] C.W. Kim and A. Pevsner, *Neutrinos in physics and astrophysics.* Harwood Academic Publishers, 1993.

[6] Z. Maki, M. Nakagawa and S. Sakata *Prog. Theor. Phys.*, vol. 28, p. 870, 1962.

[7] T. Schwetz, M. Tortola, J.W.F. Valle *New J. Phys.*, vol. 10, 2008. 113011.

[8] B. Aharmim et al. (SNO Collaboration) *Phys. Rev. C*, vol. 81, 2010. 055504.

[9] P. Adamson et al. (MINOS Collaboration) *Phys. Rev. Lett.*, vol. 106, 2011. 181801.

[10] F. P. An et al. (Daya Bay Collraboration) *Chinese Phys. C*, vol. 37, 2013. 011001.

[11] F. P. An et al. (Daya Bay Collraboration) *Nucl. Instrum. Meth.*, vol. 685, p. 78, 2012.

[12] Daya Bay Collaboration, "Daya Bay Proposal – A Precision Measurement of the Neutrino Mixing Angle Theta13 Using Reactor Antineutrinos at Daya Bay," tech. rep., Daya Bay Collaboration, 2006.

[13] Viktor Pec, "GtLiHeGen - Helium and Lithium generator," tech. rep., Daya Bay Collaboration, 2009. http://dayabay.ihep.ac.cn/cgi-bin/DocDB/ShowDocument?docid=3566.

[14] J. Ling and X. Qian, "Li9/He8 and Fast Neutron Update for P12E Dataset," tech. rep., Daya Bay Collaboration, 2013. http://dayabay.ihep.ac.cn/cgi-bin/DocDB/ShowDocument?docid=8950.

[15] Henrik Svensmark and Eigil Friis-Chridtensen *Journal of Atmosphere and Solar-Terrestrial Phys.*, vol. 59, p. 1225, 1997.

[16] Nigel Marsh and Henrik Svensmark (Danish Space Research Institute, Copenhagen, Denmark) *Journal of Geophysical Research - Atmosphere*, 2001.

[17] Ole Humlum, "Cosmic ray intensity and sunspot activity." http://www.climate4you.com/Sun.htm#Cosmic ray intensity and sunspot activity.

[18] A. R. Bell *Monthly Notices of the Royal Astronomical Society*, vol. 182, p. 147, 1978.

[19] J. Cronin, T.K. Gaisser and S.P. Swordy *Sci. Amer.*, vol. 276, p. 44, 1997.

[20] H.V. Cane *Space Sci. Rev.*, vol. 93, p. 55, 2000.

[21] NASA. http://helios.gsfc.nasa.gov/gloss_op.html.

[22] J. Poirier and T. Catanach, "Atmospheric effects on muon flux at project grand," *Proc. of the 32nd International Cosmic Ray Conference, BEIJING 2011.*

[23] P. N. Diep and P. T. T. Nhung *Commun. in Phys.*, vol. 14, p. 57, 2004.

[24] V. Yanke et al., "Temperature effect of general component seen by cosmic rary detectors," *Proc. of the 32nd International Cosmic Ray Conference, BEIJING 2011.*

[25] Marc L. Duldig *Space Sci. Rev.*, vol. 93, p. 207, 2000.

[26] L.I Dorman, *Variations of Galactic Cosmic Rays.* Moscow University Publishing House, 1975.

[27] A.N. Dmitrieva, R.P. Kokoulin, A.A. Petrukhin and D.A. Timashkov *Astroparticle Phys.*, vol. 34, p. 401, 2011.

[28] Bagrat Mailyan and Ashot Chilingarian *Adv. in Space Research*, vol. 45, p. 1380, 2010.

[29] W. C. Barber *Physical Rev.*, vol. 75, p. 4, 1949.

[30] T. K. Gaisser and T.Stanev *Phys. Lett. B*, vol. 592, p. 1, 2004.

[31] M. Guan et al., "Muon simulation at the Daya Bay site," tech. rep., Daya Bay Collaboration, 2006. http://dayabay.ihep.ac.cn/cgi-bin/DocDB/ShowDocument?docid=318.

[32] P. Antonioli et al. *Astroparticle Phys.*, vol. 7, p. 357, 1997.

[33] V.A. Kudryavtsev *Computer Phys. Commun.*, vol. 180, p. 339, 2009.

[34] I.A. Belolaptikov et al. *Astroparticle Phys.*, vol. 7, p. 263, 1997.

[35] E. Andres, et al. *Astroparticle Phys.*, vol. 13, p. 1, 2001.

[36] M. Crouch *Proc. of the 20th International Cosmic Ray Conference*, vol. 6, p. 165, 1987.

[37] Y. F. Wang et al. *Phys. Rev. D*, vol. 64. 013012.

[38] R. Hertenberger, M. Chen and B.L. Dougherty *Phys. Rev. C*, vol. 52, p. 3449, 1995.

[39] L. B. Bezrukov et al. *Sov. J. Nucl. Phys.*, vol. 17, p. 51, 1973.

[40] F. Boehm et al. *Phys. Rev. D*, vol. 62, 2000. 092005.

[41] R.I. Enikeev et al. *Sov. J. Nucl. Phys.*, vol. 46, p. 883, 1987.

[42] M. Aglietta et al. *Proc. of the 26th International Cosmic Ray Conference*, vol. 2, p. 44, 1999.

[43] M. Aglietta et al. *Il Nuovo Cimento C*, vol. 12, p. 467, 1989.

[44] J. J. Bevelacqua, *Health Physics in the 21st Century.* Wiley Online Library, 2008.

[45] Y. L. Chan, "Study of Cosmic Ray Variation in Hong Kong," Master's thesis, The Chinese University of Hong Kong, 2012.

[46] Institute of High Energy Physics, "Yang ba jing cosmic rays variations." http://ybjnm.ihep.ac.cn/nm/.

[47] T. K. Gaisser, *Cosmic Rays and Particle Physics.* Cambridge University Press, 1990.

[48] T. Kwok, *Cosmic-ray muon in the Aberdeen Tunnel laboratory in Hong Kong.* PhD thesis, The University of Hong Kong, 2011.

[49] A. Luk, "Cosmic muon-induced neutron background study in underground laboratories," Master's thesis, The Chinese University of Hong Kong, 2008.

[50] P. Lau, "Geometry of ABT Tracker," tech. rep., Aberdeen Tunnel Collaboration, 2011. http://theta13.phy.cuhk.edu.hk/elog/Aberdeen-Database/38.

[51] J. Ngai, "The Reflectance of MIRO-SILVER," tech. rep., Aberdeen Tunnel Collaboration, 2007. http://theta13.phy.cuhk.edu.hk/elog/Aberdeen-Hardware/367.

[52] J. Ngai, *Measurment of cosmic-ray muon induced neutrons in the Aberdeen Tunnel underground laboratory in Hong Kong.* PhD thesis, The University of Hong Kong, 2012.

[53] Japan Atomic Energy Agency, "Nuclear data center." http://wwwndc.jaea.go.jp/NuC/index.html.

[54] Y.C. Lin, "modified esum schematic," tech. rep., Aberdeen Tunnel Collaboration, 2012. http://theta13.phy.cuhk.edu.hk/elog/Aberdeen-Hardware/680.

[55] P. Lau, "Scintillator Efficiency Results," tech. rep., Aberdeen Tunnel Collaboration, 2010. http://theta13.phy.cuhk.edu.hk/elog/Aberdeen-Hardware/650.

[56] T. Kwok, "Energy scale calibrations," tech. rep., Aberdeen Tunnel Collaboration, 2013. http://theta13.phy.cuhk.edu.hk/elog/Aberdeen-calibration/.

[57] S. C. Blyth et al. *Nucl. Instrum. Meth.*, vol. 723, p. 67, 2013.

[58] Z. Liu et al. *Appl. Radiat. Isot.*, vol. 65, p. 1318, 2007.

[59] Y. L. Chan, "Simulating AmBe at ND south wall," tech. rep., Aberdeen Tunnel Collaboration, 2011. http://theta13.phy.cuhk.edu.hk/elog/Aberdeen-Software/406.

[60] H. M. Tsang, "Simulations and software developments for cosmic-ray and particle physics experiments in underground laboratories," Master's thesis, The University of Hong Kong, 2007.

[61] W. Zhong, "Angular Response of PMT model," tech. rep., Daya Bay Collaboration, 2006. http://dayabay.ihep.ac.cn/cgi-bin/DocDB/ShowDocument?docid=429.

[62] Y. L. Chan, "ND Efficiency of mu induced n from NuWa," tech. rep., Aberdeen Tunnel Collaboration, 2013. http://theta13.phy.cuhk.edu.hk/elog/Aberdeen-Software/515.

[63] C. Kexi, "Muon-induced neutron efficiency due to DAQ," tech. rep., Aberdeen Tunnel Collaboration, 2013. http://theta13.phy.cuhk.edu.hk/elog/Aberdeen-Software/513.

[64] F. P. An et al. (Daya Bay Collraboration) *Phys. Rev. Lett.*, vol. 108, 2012. 171803.

[65] R. Hackenburg et al., "The MuonVeto System of the Daya Bay Reactor Antineutrino Experiment," tech. rep., Daya Bay Collaboration, 2012.

[66] T. Skwarnicki. PhD thesis, 1986. DESY F31-86-02, Appendix E.

[67] Y. Nakajima, "Vertex reconstruction using charge templates for AdSimple reconstruction package," tech. rep., Daya Bay Collaboration, 2012. http://dayabay.ihep.ac.cn/cgi-bin/DocDB/ShowDocument?docid=7536.

[68] W. Q. Jiang et al. *Chinese Phys. C*, vol. 36, p. 235, 2012.

[69] K. M. Heeger and F. Wu, "AD dimensions in one figure," tech. rep., Daya Bay Collaboration, 2009. http://dayabay.ihep.ac.cn/cgi-bin/DocDB/ShowDocument?docid=4101.